Characterisation of the Turbulent Atmosphere for Free-Space Optical Communications

LILY FERN BEESLEY

Characterisation of the Turbulent Atmosphere for Free-Space Optical Communications

Lily F. Beesley

A thesis presented for the degree of

Doctor of Philosophy

Centre for Advanced Instrumentation

The University of Durham

United Kingdom

March 2024

Characterisation of the Turbulent Atmosphere for Free-Space Optical Communications

Lily F. Beesley

Abstract

Atmospheric optical degradation is a key inhibitor to the performance of a Free-Space Optical Communications (FSOC) link. The turbulent mixing of air creates a non-uniform refractive index within the atmosphere. Light propagating through this turbulent medium is subject to various propagation effects, including phase distortions, intensity fluctuations, beam wander, and speckling, all of which contribute to signal degradation at the receiver. The extent of this degradation is determined by the strength of the atmospheric turbulence encountered that the light interacts with. While the characterisation of such turbulent environments has been extensively studied within the field of astronomical instrumentation—typically in remote, high-altitude locations—these sites are not always suitable for communication links. Therefore, it is necessary to characterise turbulence in less optimal environments—this primary focus of this thesis.

This research investigates optical turbulence in diverse environments, including urban landscapes and varying zenith angles. The first part of the thesis examines the impact of changing zenith angles on the turbulence parameters σ_I^2 and r_0, crucial for ground-to-satellite communication links between transiting LEO satellites or the maintenance of a link between GEO-satellites and ground stations at high latitude. It was found that the scintillation index remains consistent with weak and strong fluctuation theories until zenith angles exceed approximately 80°, where weak fluctuations increase asymptotically and strong fluctuations saturate, deviating significantly from observed values that reduce to near 0.3. Similarly, the Fried parameter aligns well with the theory up to a zenith angle of approximately 70°. When approaching larger zenith angles, both Kasten and Young's theories and

secant scaling overestimate the Fried parameter, tending to 0.9 cm, whereas true measurements tend towards 2.5 cm, indicating weaker turbulence than predicted.

The second part of the thesis presents the first measurements of atmospheric optical turbulence in an urban environment, specifically over London's financial district, where the Fried parameter, Rytov variance, and scintillation index were found to have mean values of 4.5 cm, 0.2, and 0.08, respectively. Vertical turbulence distributions were developed based on these measurements, which were then used to simulate realistic urban FSOC conditions. The study demonstrated that adding tip/tilt-only correction and full adaptive optics (AO) improved coupling by 8.86 dB and 11.6 dB, respectively, compared to the uncorrected case. For communication links established at zenith angles of 60° or higher, full AO was recommended due to the significant aberrations at these angles, with an improvement of 4.2 dB observed between tip/tilt-only and full AO systems.

Finally, a study was conducted at the Universitat Politècnica de Catalunya in Barcelona, collecting 40 hours of continuous optical turbulence data in an urban setting. The findings revealed significant daily fluctuations in turbulence, with mean values for Fried parameter, Rytov variance, isoplanatic angle, and coherence time of 6.2 cm, 0.36, 1.1 arcsec, and 3.6 ms, respectively. The study observed a decrease in the turbulence strength, reflected in each turbulence parameter, during the transition through sunset. The performance of a satellite-to-ground optical link is simulated investigating the impact of increasing beam waist in the uplink and increased receiver size on the downlink. Each of these scenarios investigate different adaptive optics configurations to compensate for the turbulence. It was found that in the strongest observed turbulence conditions, full AO offered at most a 7 dB improvement compared to no compensation on the downlink. Additionally, for uplink precompensation, full LGS-AO offers at most a 14 dB reduction in signal losses.

Supervisors: James Osborn and Gordon D. Love

Acknowledgements

I would like to thank my supervisors James Osborn and Gordon D. Love for their academic guidance and occasional emotional support over the past 3 and a half years. James, I am thankful for your generosity in funding my travel; it has not only enriched my research but is also the reason this thesis can include nice pictures. Gordon, I am grateful for your insights into the field, and your guidance in refining my comma usage.

I also extend my thanks to Ollie, whose patience and willingness to entertain my questions, rants, and sarcasm have been invaluable. Ryan, for his dedication to engineering an instrument that is the backbone of this thesis. And to Katy, for keeping me sane while sifting through numerous errors in code during our campaigns.

Thank you Claire Whitehill for going through countless receipts from various trips and for organising each of them.

To the dwellers of OCW11, both past and present (Chris, Polly, Jeremi, Craig, Phineas, Kathryn, Puttiwat). I thank you for your interesting and stimulating conversation, as well as the many hours of necessary distractions.

I'd like to thank my family, especially my Mum for her 'relentless' enthusiasm; I couldn't have done this without you. Mum, Maia, and Saph, I dedicate this thesis to you - you are the most determined and brilliant women I know.

Finally, thank you Bernie for being patient while I wrote this thesis; we can go on all of the walks now!

Contents

Declaration

The work in this thesis is based on research carried out at the Centre for Advanced Instrumentation, Department of Physics, University of Durham, England. No part of this thesis has been submitted elsewhere for any other degree or qualification, and it is the sole work of the author unless referenced to the contrary in the text.

Some of the work presented in this thesis has been published in journals and conference proceedings - the relevant publications are listed below.

Publications

L. Westerby-Griffin, J. Osborn, O. J. D. Farley, R. Griffiths, and G. D. Love. Atmospheric optical turbulence analysis in London's financial district. In H. Hemmati and B. S. Robinson, editors, *Free-Space Laser Communications XXXV*, volume 12413, page 55. SPIE, 3 2023a. ISBN 9781510659315. doi: 10.1117/12.2648907. URL https://doi.org/10.1117/12.2648907

L. Westerby-Griffin, J. Osborn, O. J. D. Farley, R. Griffiths, and G. D. Love. Atmospheric optical turbulence measurements at varying elevation angles. In H. Hemmati and B. S. Robinson, editors, *Free-Space Laser Communications XXXV*, volume 12413, page 56. International Society for Optics and Photonics, SPIE, 3 2023b. ISBN 9781510659315. doi: 10.1117/12.2649231. URL https://doi.org/10.1117/12.2649231

L. F. Beesley, J. Osborn, R. Wilson, O. J. D. Farley, R. Griffiths, and G. D. Love. Exploring atmospheric optical turbulence: observations across zenith angles. *Applied Optics*, 63(16):E48, 2024. ISSN 1559-128X. doi: 10.1364/ao.519063

List of Figures

List of Tables

Nomenclature

AO Adaptive Optics

DM Deformable Mirror

FSOC Free-Space Optical Communications

FAST Fourier Domain Adaptive Optics Simulation Tool

KY Kasten and Young

LEO Low Earth Orbit

LGS Laser Guide Star

GEO Geostationary Orbit

HV Hufnagel-Valley

NGS Natural Guide Star

OGS Optical Ground Station

SHIMM Shack-Hartmann Image Motion Monitor

SHWFS Shack-Hartmann Wavefront Sensor

PAA Point-Ahead Angle

PSF Point Spread Function

QKD Quantum Key Distribution

RF Radio Frequency

WFS Wavefront Sensor

CHAPTER 1

Introduction

Turbulence has captivated the curiosity of both artists and scientists throughout history. From Leonardo da Vinci's attempts to describe the chaotic motion of water vortices in a running tap to Vincent van Gogh's depiction of the swirls of the air in our atmosphere in both *Starry Night* and *Road with Cypress and Star* (see figure 1.1), turbulence remains an enduring subject of fascination. In our daily lives, turbulence influences the clouds we see, the weather we experience, and how light passes through our atmosphere.

Recently, scientists have been studying the nature of optical propagation through atmospheric optical turbulence. Turbulence creates localised variations in air density, akin to behaving as tiny lenses, distorting the light as it passes through them. This phenomenon, long known to astronomers, manifests itself in the twinkling of stars and the apparent shift in their positions. Our comprehension of optical turbulence has been pivotal in the evolution of ground-based optical telescopes, supplementing our understanding of the universe. Moreover, researching optical turbulence has gained renewed significance in the subject of Free-Space Optical Communications (FSOC).

Current communications systems face saturation due to an ever-increasing demand for global connectivity. A surge in the number of devices requiring internet connectivity, coupled with the advancement of technology used by each device means that there

Figure 1.1: Vincent van Gogh, Road with Cypress and Star (1890).

are ever-increasing data demands per user. By using optical frequencies for communication instead of radio frequencies, access to the high data rates and low latency provided by fibre optic communications is achieved, along with the freedom to propagate through the atmosphere. This allows for communication with satellites using optical wavelengths, as well as the establishment of terrestrial links without the constraints of fibre installation.

The benefits of integrating FSOC into global communication systems cannot be overstated. Low latency ensures swift responsiveness in data transmission, crucial for applications such as real-time communication, financial transactions, and remote control operations. In the context of FSOC, this lower latency is achieved not due to faster propagation speeds, but rather because of the higher bandwidth and reduced congestion compared to Radio Frequency (RF) systems (Uysal, 2016). Additionally, high

data rates facilitate the seamless transfer of large volumes of data, which is essential for bandwidth-intensive tasks like high-definition video streaming, cloud computing, and big data analytics (Pan et al., 2002). The benefits from these advancements are broad-reaching and have the capacity to improve many aspects of society and industry, which will be discussed in detail in Section 2.1.2. By enabling efficient and rapid communication, these advancements contribute to enhanced productivity, innovation, and connectivity on a global scale (Zafar and Khalid, 2021; Malik and Singh, 2015).

However, the propagation of laser beams through the atmosphere is significantly impeded by optical turbulence. This atmospheric phenomenon induces phase distortions onto the propagating beam, leading to effects such as beam wander and intensity distortion. Ultimately, these distortions can hinder the transmission of photons between the transmitter and receiver, resulting in potential data loss.

The focus of this thesis is to characterise optical turbulence conditions that optical communication links will have to propagate through. This involves areas of optical turbulence theory previously unexplored by astronomical instrumentation, such as large zenith angles and within urbanised environments.

In chapter 4, work characterising the effects of increasing zenith angle on the propagation of light is presented. Satellite-to-ground optical communications systems must operate at all zenith angles, a scenario not commonly encountered in astronomy. The dependence of optical turbulence parameters on zenith angles is analysed by conducting concurrent measurements using two instruments: one positioned near zenith and the other tracking a target through all zenith angles. The measurements are found to agree very well with the theory up until very large zenith angles.

Chapter 5 introduces the first optical turbulence measurements conducted in an urban environment, where free-space optical communications will inevitably operate, yet remains inadequately characterised. The results of an initial study conducted in London are presented. With these results, the potential performance of an optical commu-

nication link within the city is predicted, as well as a novel approach to deriving an atmospheric model that matches the observed conditions.

A final study, presented in chapter 6, involves 40 hours of continuous turbulence measurements within the city of Barcelona. This study is part of the commissioning of a permanent instrument at the Universitat Politècnica de Catalunya (UPC), a 24-hour turbulence monitor designed to aid in characterising atmospheric turbulence in Barcelona. Various diurnal effects, turbulence weather dependencies, and potential design parameters of an optical ground station are investigated.

This research aims to better understand the turbulent conditions under which FSOC links must operate. By doing so, it lays the groundwork for the future of this communication technology, paving the way for its adoption and ensuring its reliability in real-world conditions.

CHAPTER 2

Free-Space Optical Communications

This chapter provides an overview of the historical background of FSOC and its relevance to today's communication systems. The components of an FSOC system are explored, highlighting its potential advantages and the challenges associated with FSOC communication. The discussion concludes with the form of laser propagation in the atmosphere and considerations for the satellites used for relaying information.

2.1 Overview of FSOC

2.1.1 History of optical communications

Modern forms of optical communications trace back to the mid-19th century. Claude Chappe established a network of optical telegraphs employing semaphore signals which spanned several hundred kilometres, covering most major French cities as well as reaching Amsterdam and Vienna (Dilhac, 2001). Messages could be encoded onto the arms of the device, shown in figure 2.1, and it was 50 times faster at transmitting messages compared to a postal carrier. Despite its initial success, operational complexities led to its failure, and it was soon replaced with electrical telegraphs.

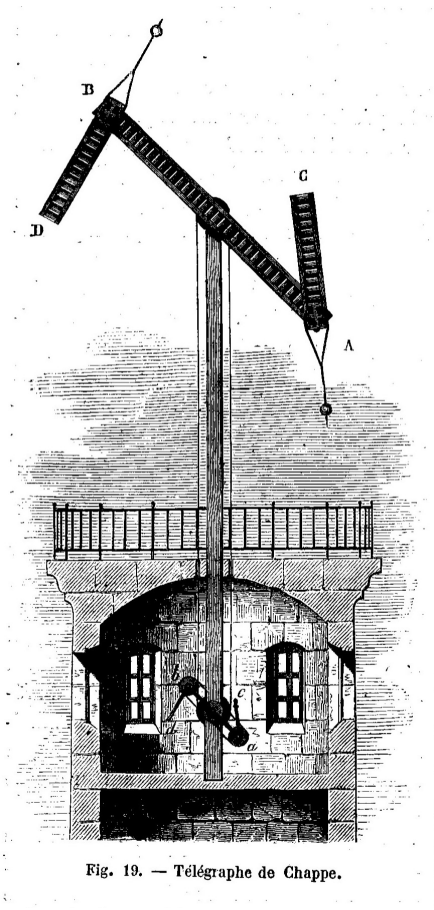

Figure 2.1: The Chappe telegraph developed in the late 18th Century. Each arm could rotate by 45° to create a semaphore that could be read by neighbouring towers by telescope (figure from Dilhac (2001)).

Over the next century, RF technologies found swift adoption by the military during World War I to enable communication between ships and aircraft. Soon afterwards, the technology transitioned to non-military use. In 1921, the Detroit Police Department made an early adoption of radio communications, utilising the 2 MHz band to facilitate communication between patrol cars and their central command (Sanders et al., 2003). Messages could be encoded into the signal by modulating the amplitude of this particular frequency. This new technology proved so successful that it was soon used across the United States until eventually, the 2 MHz band became overcrowded. With investments into developing wireless communications, different channels within the radio spectrum became accessible for broadcasting. Again, these frequencies were quickly

used up and radio interference was a significant problem. This led to the first-ever licensing of the radio spectrum whereby broadcasting authorities controlled who could transmit in a particular frequency and in what area.

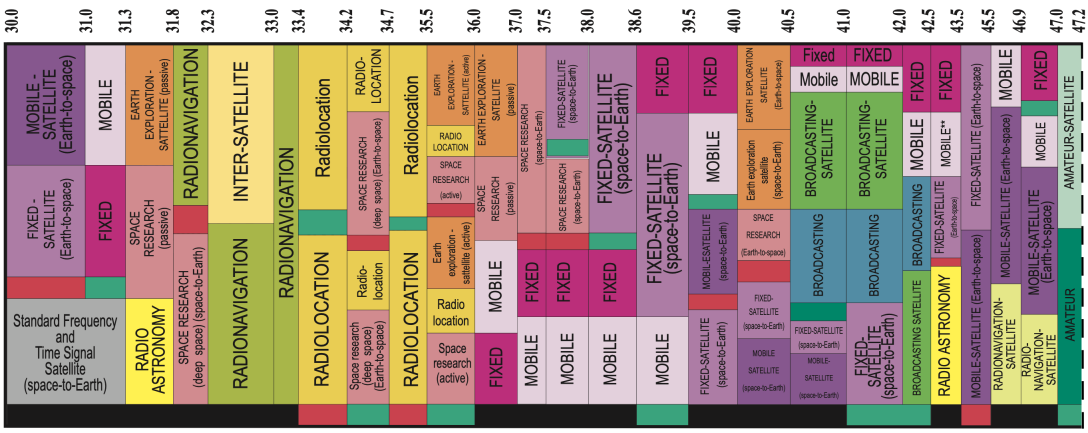

Figure 2.2: United States frequency allocation from the National Telecommunications and Information Administration, 2016. This is cropped to show the band from 30 GHz to 47.2 GHz.

Despite today's telecommunications being significantly more advanced than the simple amplitude modulation of the 1920s, the same problem still arises. With a finite electromagnetic spectrum there can only be a finite number of connections and as technology evolves so too does the need for high-speed, cost-effective and secure internet access. This critical point is referred to as the Spectrum Crunch whereby spectral demand outweighs supply. This is displayed in Figure 2.2, illustrating the spectrum allocation within the United States communication network. The intricate patchwork of RF allocations emphasises the necessity for careful management to regulate each communication band.

Wired forms of communication have outgrown copper-based internet and evolved into fibre optic communications, enabling data speeds in the order of terabytes per second. While this communication system offers exceptional performance, establishing such connections can be both costly and invasive. The installation often involves the complex

process of laying submarine cables across the ocean floor. Additionally, the vulnerability of these cables to accidental cuts poses a significant risk, potentially resulting in a complete loss of internet connectivity for a specific area.

FSOC now has the potential to combine the advantages of both RF and fibre optics, explicitly offering the high data speeds of optical fibres and the inherent wireless nature of RF communications.

2.1.2 Future applications

FSOC features high data rates, low power demands, portability, cost-effectiveness, and inherent security (Uysal, 2016; Carbonneau and Wisely, 1998; Britz et al., 2001). The implementation of FSOC is explored, showing how it will not only improve but also become an integral part of future communication systems.

Optical feeder links

Free-space optical feeder links offer a suitable alternative to the current RF feeder links for future generations of satellites. Feeder links refer to the link between a satellite and a ground station and form the backbone for communications. The current world's highest capacity telecommunications satellite, ViaSat-2, is capable of supporting a data transfer rate of up to 260 Gbps using RF communications (ViaSat, 2017). However, the increasing demand for high data rates will require more high-throughput satellites to operate at Tbps ranges to ensure all users can access speeds of at least 30 Mbps (Barrios et al., 2021). Despite optical communications being an emerging technology, ground-based demonstrations have shown that optical links are capable of supporting Tbps data rates, indicating their viability for future satellite communication systems(Fuchs et al., 2019).

Space missions

It appears that the next stage of human exploration lies beyond Earth. Space navigation

and communication for such sophisticated space missions require vast amounts of data transfers, a demand that cannot be solely supported by RF communications. NASA has projects that specifically focus on the development of optical communications for high-data rates and deep space communications for future space exploration (Schieler et al., 2022; Hart et al., 2018). Specifically, the goal to maximise data rate to support human exploration of Mars even at maximum distances from Earth.

Similarly, as space-based astronomical telescopes are becoming more advanced the data rate that will be required to support the transmission of large quantities of science-data from telescope to Earth will reach a point where only FSOC will be able to support it (Johns et al., 2008).

Quantum Key Distribution (QKD)

One crucial application of FSOC is QKD. With the increasing power and accessibility of computers, classical cryptography faces growing insecurity. Quantum cryptography, based on the principles of quantum mechanics, ensures theoretically unconditional security. QKD, a well-developed form of quantum cryptography, facilitates intermittent key exchange, primarily implemented over long distances through satellite-to-ground optical channels (Zapatero et al., 2023; Wang et al., 2019). This intermittent key exchange is particularly advantageous as it reduces the reliance on consistently clear weather conditions. QKD is an attractive alternative form of key exchange for applications that require highly secure communications, such as those in the financial and governmental sectors.

Disaster relief

In certain disaster scenarios, such as natural catastrophes, there may be a complete loss of communications (Topcu et al., 2011). FSOC technologies can be quickly deployed via unmanned aerial vehicle (UAV) to provide network coverage when high bandwidth

Developer	Mission name	Data rate (Gbps)	Wavelength (nm)	Modulation	Ref.
AC	NFIRE	5.7	1064	BPSK	Fields et al. (2011)
DLR	OSIRISv2	1	1550	OOK	Fuchs et al. (2019)
DLR	OSIRISv1	0.2	1550	OOK	Fuchs and Schmidt (2019)
AC	OCSD-B&C	0.2	1064	OOK	Rose et al. (2019)
JAXA	SOLISS	0.1	1550	OOK	Yamazoe et al. (2022)
DLR	OSIRIS4Cubesat	0.1	1550	OOK	Schmidt et al. (2022)
JPL	TBIRD	200	1550	QPSK	Schieler et al. (2022)

Table 2.1: Overview of current state-of-the-art FSOC demonstrations. AC denotes Aerospace Corporation, DLR.

is necessary (Kaushal and Kaddoum, 2017). For accurate monitoring of disaster zones, the ground must be imaged by high-resolution instruments either from satellite or aeroplane. FSOC enables the fast and efficient transfer of large volumes of data, facilitating real-time observations of disaster zones. This cannot be accomplished by solely using RF communications (Pan et al., 2002).

2.2 Current state-of-the-art FSOC systems

Despite much of the initial research and development into free-space optical communications occurring in the 1970s, full development of FSOC systems has only recently been possible due to advancements in the enabling technology.

Table 2.1 presents the current state-of-the-art demonstrations for free-space optical communication between satellites and ground stations. There are numerous additional demonstrations involving communication between aircraft and ground stations, which are not included in this table for clarity (Walsh et al., 2022).

Reviewing these current demonstrations allows identification of the most used wavelengths, the highest attainable data rates, and the most successful modulation schemes. This information justifies the system choices used in our simulations and helps to validate

our approach in section 2.3.

2.2.1 Current state-of-the-art modulation schemes

Table 2.1 shows the modulation schemes that have been used for signal modulation. On-Off Keying (OOK) is one of the simplest modulation schemes, where the intensity of the light is modulated such that the presence of light represents a '1' and the absence of light represents a '0'. OOK is advantageous due to its simplicity and minimal hardware requirements, where a photodetector can be used to observe the change in intensity of the optical beam (Wang et al., 2017). However, it is less efficient in terms of bandwidth and power and is more susceptible to noise.

Phase modulation is also used in Binary Phase Shift Keying (BPSK) and Quadrature Phase Shift Keying (QPSK) are also used. In BPSK, the phase of the carrier signal is shifted between two values, typically 0° and 180°, to represent binary '0' and '1'. This method allows for robust data transmission with good noise immunity, but only one bit of data is transmitted per symbol (Proakis, 2001). QPSK further enhances the efficiency by using four different phase shifts (0°, 90°, 180°, and 270°) to represent two bits per symbol. This higher efficiency makes QPSK more bandwidth-efficient, allowing for higher data rates compared to BPSK and OOK, as seen in Table 2.1 with TBIRD. The detection of a phase-modulated beam is more complex as it requires coherent detection to demodulate the phase information of the received signal (Ziemer and Tranter, 2001).

2.3 Characteristics of FSOC

The foundation of any form of free-space communication is to superimpose information onto the propagating electromagnetic wave. As this technology is built upon that used in fibre-optic communications, the signal modulation used can be incredibly complex.

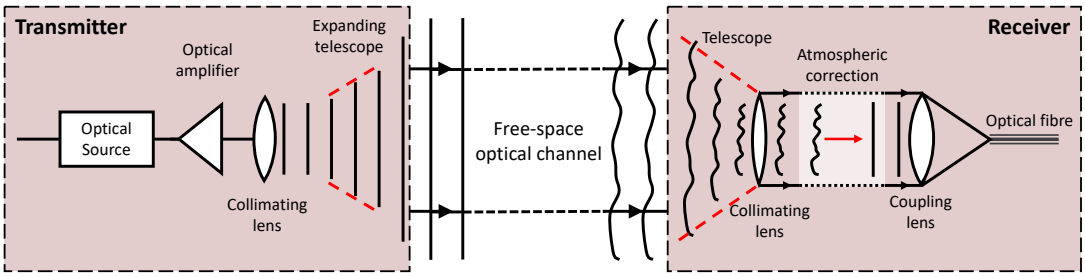

Figure 2.3: Diagram showing the typical components of an FSOC system. Consisting of a transmitter, free-space optical channel and a receiver.

For the sake of simplicity, this work operates on the knowledge that a successful FSOC link will maximise the mean received intensity and minimise the variance in the received intensity.

These metrics are useful for comparing simulations across different turbulence environments and optical systems. The mean received intensity provides a first-order approximation of system performance, allowing for the comparison between systems by observing that one has a larger mean received intensity than another, indicating that more photons reach the receiver. However, the mean received intensity alone does not account for scintillation variations caused by turbulence (see section 3.2.1). Therefore, both metrics must be considered together to evaluate system performance.

Other metrics, such as the probability of fade or bit error rate (BER), can also demonstrate the performance of an FSOC system, however this work focuses on mean received intensity and variance due to their direct relevance to overall signal quality and stability.

2.3.1 Overview of an FSOC system

Figure 2.3 shows a diagram of a FSOC link. Each link consists of a transmitter and receiver separated by a free-space channel. The transmitter uses an optical source, typically a laser beam, which undergoes amplification and collimation to ensure a plane wave during propagation. This beam is expanded using a telescope before transmission through the atmosphere, where a smaller aperture experiences higher beam divergence,

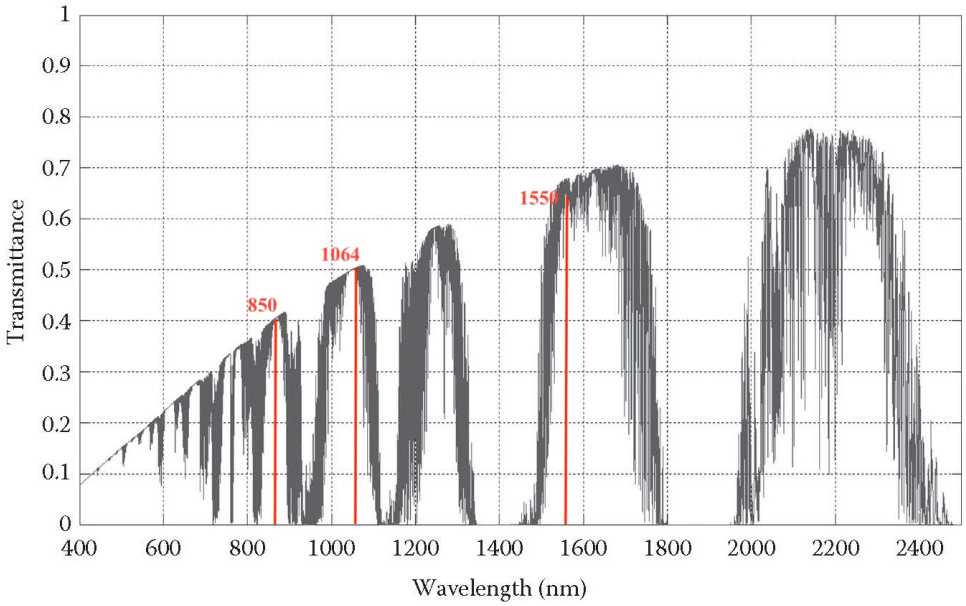

Figure 2.4: Atmospheric transmission as a function of wavelength for a visibility of 5 km in an urban environment. Adapted from Alkholidi and Altowij (2014).

as detailed further in section 3.2.3. The beam's divergence can be optimised to increase the likelihood of successful reception at the receiver.

Upon reaching the receiver, a telescope collects the light, directing it to a collimating lens. At this stage, the light can undergo processes to correct for atmospheric effects, such as adaptive optics. Subsequently, the corrected light can be demodulated using a photodetector or coupled into an optical fiber for either coherent detection or integration into an existing network. The type of demodulation used is specific to the system as discussed in section 2.2.1. However, demonstrating a high-bandwidth phase modulation technique such as QPSK requires the use of an optical fibre.

Note that this diagram may vary significantly based on the communication type used; however, for the purposes of this document, the provided diagram suffices.

2.3.2 Operational wavelengths

Figure 2.4 shows the transmittance of optical light as a function of wavelength through our atmosphere. There are clear windows over which certain wavelengths have maximum improved transmittance. The spectral regions around 850 nm, 1064 nm, and 1550 nm correspond to operational wavelengths used by optical fibres within telecommunications, these are due to them being readily available lasers. This preference is due to the widespread availability and well-developed nature of lasers operating at these frequencies. These are the three most appropriate spectral windows to use for FSOC due to their compatibility with existing communication systems and can be built using off-the-shelf components.

This document will focus specifically on communications at a wavelength of 1550 nm. This wavelength allows for the safe use of higher power levels in laser transmission due to its higher Maximum Permissible Exposure (MPE) limits, as established by the International Commission on Non-Ionizing Radiation Protection (ICNIRP) (Ziegelberger, 2013). Consequently, this reduces the risk of harmful effects on human tissues, particularly the eyes. Additionally, the 1550 nm wavelength demonstrates greater resilience to optical turbulence, a topic which is further explained in chapter 3.

2.3.3 Challenges in FSOC

Here, the main contributors to signal degradation for FSOC are discussed. The signal losses can be divided into those caused by geometric losses based on beam shaping and those losses caused by atmospheric attenuation in the propagating channel (Bloom et al., 2003; Zafar and Khalid, 2021; Miller, 1997). This thesis focuses on the latter.

Absorption and scattering

Gases, aerosols, and particulates are abundant within our atmosphere and affect the propagation of optical light. Scattering, the alteration of light direction, and absorption,

Weather	Atmospheric loss (dB/km)
Urban haze	0.5
Typical rainfall	3
Heavy rainfall	6
Snow	10
Typical fog	10
Heavy to severe fog	30 – 120

Table 2.2: A table of atmospheric losses at 1550 nm for various weather conditions. Adapted from Miller (1997).

the extinction of the light, both contribute to signal attenuation. Fog poses the most significant risk to signal attenuation, while rain, haze, and snow can also contribute to the attenuation process. Signal losses are expressed as atmospheric loss in decibels per kilometre (dB/km). The decibel (dB) is a logarithmic unit used to measure the intensity of a signal. Signal loss in dB is calculated using the formula:

$$\text{Loss (dB)} = 10 \log_{10} \left(\frac{P_{\text{R}}}{P_{\text{T}}} \right) \tag{2.1}$$

where P_{R} is the power received and P_{T} is the power transmitter. The atmospheric losses corresponding to different weather conditions are presented in table 2.2.

Atmospheric optical turbulence

Atmospheric optical turbulence is caused by random fluctuations in the refractive index of air, which result in the aberration of the optical phase as light passes through. As the light propagates, these variations cause distortions in the light's phase causing a local focusing and defocusing effect leading to variations in amplitude. This is commonly referred to as scintillation and is discussed further in section 3.2.1. This leads to a reduction in the received signal as well as an uncertainty in the received signal. This cause of signal loss is explored throughout this thesis.

2.4 Optical links through our atmosphere

Our main focus within this project is to study how an optical link is affected by atmospheric optical turbulence on FSOC. The extent to which the atmosphere can cause signal degradation is dependent on the type of link used to communicate.

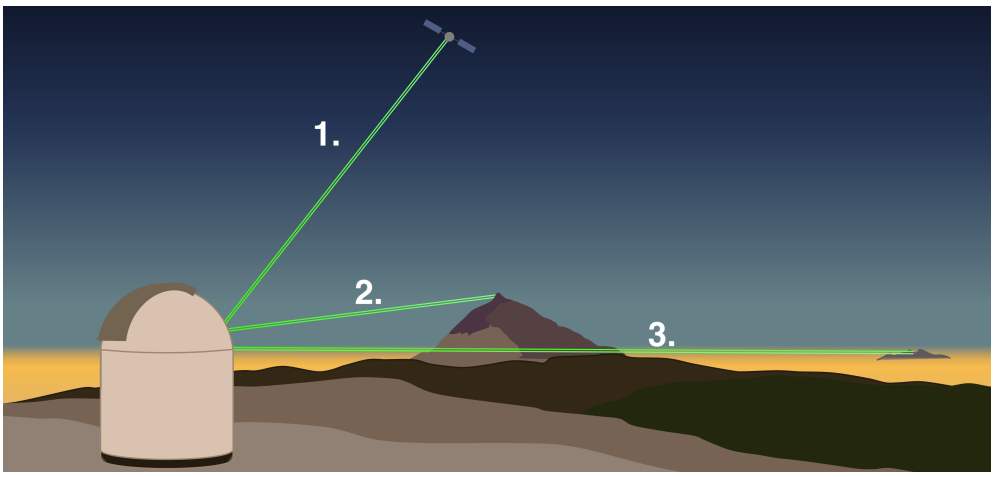

Figure 2.5: Schematic for the long-range FSOC link scenarios discussed in this section. Links, shown in green, include uplink/downlink, slant-path, and horizontal, labelled as 1., 2., and 3., respectively. The white dome represents an Optical Ground Station (OGS).

2.4.1 Long-range FSOC link configurations

A standard FSOC link requires a transmitter, a free-space optical propagating channel, and a receiver. The receiver can either directly detect the laser signal using a photodetector or can couple the light into an optical fibre. Depending on the application, each link will require different implementation strategies (Uysal, 2016). Each type requires unique system capabilities, such as link range and transmitter size, and will have to operate under vastly different atmospheric optical turbulence distributions. A schematic for these link types is displayed in figure 2.5.

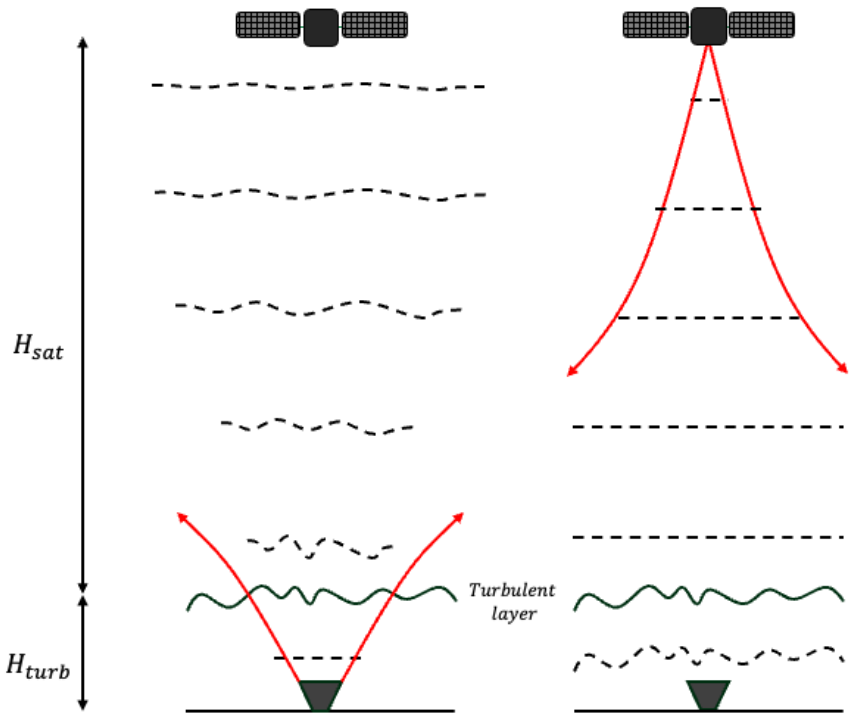

Figure 2.6: Diagram illustrating uplink (left) and downlink (right). H_{sat} denotes the distance from the turbulent layer to the satellite and H_{turb} denotes the distance from the ground to the turbulent layer.

Uplink/Downlink to satellite

Such FSO links will communicate from ground-to-satellite (uplink) and from satellite-to-ground (downlink). Figure 2.6 illustrates the effect of atmospheric turbulence on the communication link. As atmospheric turbulence is concentrated towards the ground end of the propagating channel, the mechanism for signal degradation is significantly different (Andrews and Phillips, 2005).

In uplink channels, the greater distance between the atmospheric optical turbulence and the receiver (on the order of hundreds to thousands of kilometres) allows small turbulence-induced phase aberrations on the propagating beam to evolve into beam wander and scintillation. This phenomenon is explained further in section 3.2.1. Conversely, in downlink channels, these same turbulence-induced phase aberrations propag-

ate over a shorter distance (on the order of tens of kilometres). Consequently, while beam wander and scintillation are reduced compared to uplink, the phase aberrations are more pronounced, resulting in increased angle-of-arrival fluctuations.

The transmitter/receiver for this configuration on the ground is referred to as an OGS. Ground-to-satellite links represent one of the more promising forms of long-range form FSOC due to its minimal interaction with our atmosphere compared to terrestrial links.

Horizontal Link

Here the light will be modulated to carry information from transmitter to receiver which are both positioned on the ground. Unlike vertical propagation, the optical turbulence along a horizontal propagation path is a continuous medium between transmitter and receiver, referred to as deep turbulence. These links can exist at both low- and high-altitude, the latter operating in weaker atmospheric turbulence. Such links can exist on the scale of m's to tens of km's.

Slant-Path

Slant-path propagation is between ground and high altitude, e.g. a mountain top or aeroplane, as shown in figure 2.5. Similarly to ground-to-satellite links, the beam will only propagate through the strongest turbulence at ground level. The difference is that the beam will only continue to propagate for a few km's. The vertical turbulence distribution being weaker than that for horizontal links, combined with the smaller propagation distance compared to ground-to-satellite links, makes this an attractive form of FSOC. Slant-paths are also being used to profile the turbulence for applications to uplink/downlink communications (Montmerle-Bonnefois et al., 2019).

2.4.2 Communication Channels to Different Orbits

Consideration of the atmospheric optical channel is also important when evaluating types of communication satellites.

Low Earth Orbit (LEO)

Satellites in LEO orbit at ∼400-1,000 km, this proximity to Earth's surface makes them desirable for communications (Cochetti, 2014). These orbits can include polar (about the Earth's poles), equatorial (above the equator) and inclined (at an angle to the equator). Limitations of these satellites are that they are not always in the observer's field of view, so have to be deployed as constellations which can increase risks of collision in LEO orbit. They also have to have complex tracking mounts and have to compensate for atmospheric effects both very quickly due to the fast orbital velocities and complex turbulence effects due to low-elevation communications.

Geostationary Orbit (GEO)

GEO satellites are positioned in orbit at an altitude where their orbital period matches the Earth's rotation, allowing them to remain fixed relative to a specific point on the Earth's surface. This fixed position makes the link between ground and satellite relatively easy to establish. However, given their orbit at approximately ∼35,000 km, 35 times farther away than LEO satellites, the latency is significantly higher. This increased latency can impact real-time communications, such as video calls. Additionally, their geostationary position above the equator results in limited coverage for areas at high latitudes.

CHAPTER 3

Optical propagation through atmospheric optical turbulence

3.1 Atmospheric optical turbulence

In fluid mechanics, the nature of fluid motion can be broadly classified into two categories: laminar flow and turbulent flow, each exhibiting distinct characteristics. Laminar flow is characterised by a smooth, organised movement of fluid in parallel layers, with minimal mixing between adjacent layers. On the other hand, turbulent flow is marked by chaotic and irregular fluid motion, leading to significant mixing and the formation of eddies and vortices. The distinction between laminar and turbulent flow depends on the fluid's Reynolds number denoted as Re where $Re = vL/\nu$, where v and L represent the flow's characteristic velocity and length scale, and ν is the fluid's kinematic viscosity (Wyngaard, 2010). Figure 3.1 shows the transition of a water jet from laminar to turbulent flow. The interaction with ambient fluid, called shear strain, causes the initially predictable flow to mix and break down in structure to form turbulent vortices.

The Earth's atmosphere undergoes turbulent mixing resulting from convective and radiative processes, as well as mixing induced by wind shears between layers of varying densities and pressures. This turbulent mixing generates spatial inhomogeneities in

Figure 3.1: Laser sheet illumination of a dyed water jet. Demonstration of transition from laminar flow into turbulent flow. From Reynolds et al. (2003).

the air's temperature (Good et al., 1988), which are directly proportional to refractive index inhomogeneities.

$$D_n(\boldsymbol{\rho}) = \langle |n(\boldsymbol{r}) - n(\boldsymbol{r} + \boldsymbol{\rho})|^2 \rangle = C_n^2 \rho^{2/3}. \tag{3.1}$$

Here, $\rho = |\boldsymbol{\rho}|$ and $\langle\rangle$ denotes the ensemble average. The value C_n^2 is known as the refractive index structure parameter and is used as a measurement to characterise the strength of turbulence. It is measured in units of $\mathrm{m}^{-2/3}$.

The inherently random nature of turbulence makes it impossible to predict its behaviour analytically. In other words, foreseeing how a turbulent fluid will evolve is unfeasible since its development is highly sensitive to its initial state. Therefore, turbulent behaviours are analysed statistically, an approach most notably developed by Roddier (1981).

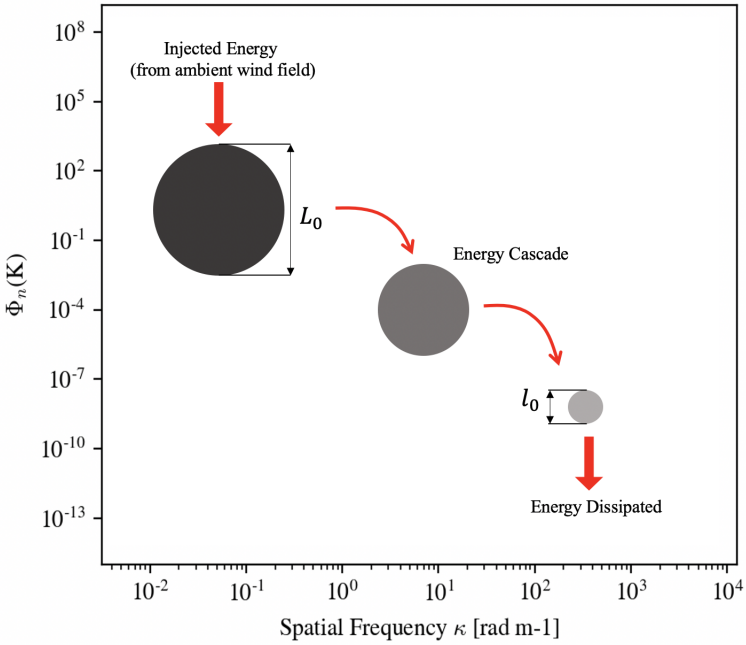

Figure 3.2: Qualitative description of energy transfer between eddies in turbulent flow.

Kolmogorov's model adopts an energy cascade theory, where energy is injected into the system via wind shear or convection at large scales (see figure 3.2). This process induces a region of air with a uniform refractive index, referred to as an eddy. Inertial forces cause these eddies to divide into smaller and smaller ones until the energy is eventually dissipated as heat. The characteristic scales of this process are the inner scale l_0 and outer scale L_0, describing the smallest and largest size of eddies, respectively, within the inertial subrange. Eddies within this subrange are assumed to be statistically homogeneous and isotropic, where the power spectrum for the refractive index is written as (Tatarskii, 1971)

$$\Phi_n^K(f) = 0.033(2\pi)^{-2/3} C_n^2 f^{-11/3}, \tag{3.2}$$

where f is the spatial frequency with units of m^{-1}.

In this context, homogeneous refers to the statistical properties of the turbulence being uniform throughout the medium, indicating that the properties do not change with location (Pope, 2000). Isotropic describes the statistical properties being the same in all directions, implying that the turbulence has no preferred direction.

Kolmogorov's power spectrum is only valid when within the inertial subrange, i.e. it assumes an infinite outer scale and zero inner scale. A modification to this equation was introduced by Von Karmán to include more realistic length scales. These are expressed as:

$$\Phi_n^{VK}(f) = 0.033(2\pi)^{-2/3} C_n^2 \left(f^2 + \frac{1}{L_0^2}\right)^{-11/6} \exp\left(-\left(\frac{2\pi l_0}{5.91} f\right)^2\right), \tag{3.3}$$

which is valid for all values of f. This equation is particularly relevant when considering turbulence at near-ground level, where L_0 cannot exceed the height above the ground. Both models are presented in figure 3.3.

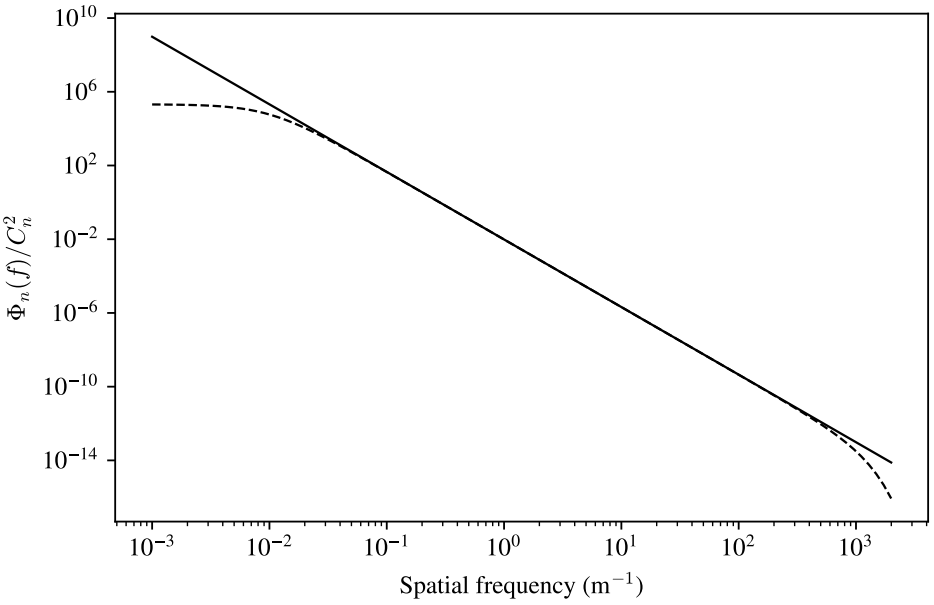

Figure 3.3: Power spectral densities of the variation in refractive index. Normalised with the C_n^2 value of 1. The solid line represents the Kolmogorov theory while the dotted depicts the Von Kármán theory with an $L_0 = 100$ m and $l_0 = 0.001$ m.

3.1.1 Dependence of C_n^2 with altitude

Our atmosphere is considered stratified whereby distinct layers exhibit unique temperature, pressure, and composition characteristics. Since 97% of our atmosphere is

compressed within the first 30 km, our focus will be on the first two layers, namely the troposphere and stratosphere, which roughly extend from 0 to 20 km and 20 to 50 km, respectively (Holton and Hakim, 2012).

As this document explores atmospheric optical turbulence in different environments, it's important to understand how the measured optical turbulence can arise from meteorological effects, site location and surface topology.

Boundary layer

The boundary layer experiences turbulent mixing driven by diurnal heating and cooling processes. During the day, solar heating induces vigorous vertical convective mixing as the ground warms the cooler surrounding air (Tokovinin, 2010; Roadcap and Tracy, 2009). At night, the ground loses heat to the now-warmed surrounding air. This layer is unstable, and its C_n^2 value can vary by several orders of magnitude throughout the day, ranging 10^{-13} $m^{-2/3}$ to 10^{-15} $m^{-2/3}$. At some point during dawn and dusk, a state of thermal equilibrium is reached between the ground and air, resulting in temporary stability with lower turbulence. As the temporal turbulence dynamics are dependent on solar heating, the latitude and season have a strong effect on the behaviour of the boundary layer (Ryznar and Bartlo, 1986). Similarly, the height of the boundary layer is specific to the location and can be as high as several kilometres.

Free atmosphere

Above the boundary layer exists the free atmosphere, where turbulent effects are not influenced by ground heating (Wallace and Hobbs, 2006). The free atmosphere encompasses the troposphere, and stratosphere, divided by the tropopause which is the boundary between them. Measurements of the C_n^2 profiles within the free atmosphere find that there exist regions of a distinct value C_n^2 which form a layer, or laminae, hundreds of metres thick. Observations determine that they coincide with areas of strong temperature gradients such as inversion layers and increases in humidity although the

complex dynamics that form these layers are still not well understood. Similarly, predicting the temporal development of turbulence within the free atmosphere is complex due to the influence of large-scale meteorological factors, such as jet streams and the Coriolis effect (Tatarski, 1961).

Hufnagel-Valley model

Numerous experiments have measured C_n^2 as a function of altitude e.g. Wesely and Alcaraz (1973); Wilson (2002); Azouit and Vernin (2005); Coulman et al. (1995); Avila et al. (1997); Bi et al. (2020); Cheinet and Siebesma (2007); Abahamid et al. (2004). These measurements have allowed for the development of empirical models of vertical C_n^2 profiles. One of the more notable models is the Hufnagel-Valley (HV) model. This model encapsulates atmospheric stratification by accepting meteorological parameters as inputs. It is given by (Farrell, 2019),

$$C_n^2(h) = 0.00594\left(\frac{w}{27}\right)^2\left(10^{-5}h\right)^{10}\exp\left(-\frac{h}{1000}\right)+ 2.7\times10^{-16}\exp\left(-\frac{h}{1500}\right)+A\exp\left(-\frac{h}{100}\right), \quad (3.4)$$

where h is the altitude in m, w is the Hufnagel-Valley wind speed parameter, and A is known as the structure constant, equal to the surface layer turbulence strength. Typically, it is considered that a structure constant for weak and strong boundary layer turbulence is 1.7×10^{-14} m$^{-2/3}$ and 1.7×10^{-13} m$^{-2/3}$, respectively. Additionally, w is recognised to lie between 10 ms^{-1} and 30 ms^{-1} for weak and strong upper atmospheric wind speeds, respectively. Figure 3.4 displays the vertical C_n^2 distribution corresponding to the HV-model for strong and weak boundary layer turbulence.

The HV-model can provide a good first approximation for the estimated vertical distribution of optical turbulence. However, a single distribution of optical turbulence cannot satisfactorily define any strong or weak turbulent regime. For a better understanding of a particular turbulent channel, one must measure the turbulence parameters directly.

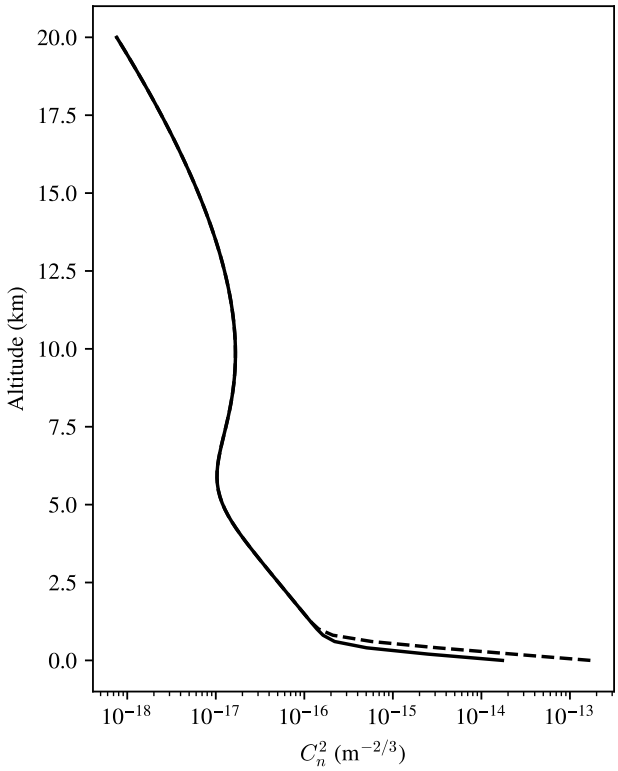

Figure 3.4: Hufnagel-Valley profiles for night (solid) and day (dashed) conditions, defined by a structure constant value of 1.7×10^{-14} $m^{-2/3}$ and 1.7×10^{-13} $m^{-2/3}$, respectively.

3.1.2 Integrated C_n^2

When simulating the propagation of light through the atmosphere, optical turbulence is commonly modelled using discrete, infinitesimally thin layers. A layer can be derived from any C_n^2 distribution by integrating C_n^2 between altitudes h_0 and h_1, a value calculated as:

$$C_n^2 dh = \int_{h_0}^{h_1} C_n^2(h) dh. \tag{3.5}$$

Here, $C_n^2 dh$ represents the integrated value of C_n^2. Similar approaches can be used for modelling the horizontal distribution of turbulence, where integration is performed over horizontal distances instead of altitudes.

3.1.2.1 Airmass dependence on zenith

For modelling and establishing bidirectional communication links, it is essential to understand how optical propagation through atmospheric turbulence varies with the zenith angle. The zenith angle is the angle between the target and the vertical directly above the observer (zenith). For communication links between LEO, MEO and any non-geostationary satellite, the OGS and satellite will need to maintain links over all zenith angles. Similarly, any geostationary satellite at non-zero latitudes must communicate at varying zenith angles. This discussion begins with the consideration of zenith angle for modelling the atmosphere.

The optical airmass is defined as the integrated air density over the propagating path of light. The relative air mass, denoted as M, is used here. It scales the absolute air mass by dividing it by the air mass within the vertical column directly above the observer, in order to only consider the difference in the propagation path. Typically, the airmass is at its lowest value when observing at the zenith. The maximum airmass is observed when looking at a target along the horizon. Assuming a plane parallel atmospheric model and neglecting the curvature of the Earth and refraction, the relative air mass is then the secant of the zenith angle, ζ:

$$M(\zeta) = \sec(\zeta). \tag{3.6}$$

However, a consequence of the $\sec(\zeta)$ dependence leads to the atmospheric optical turbulence tending to be infinitely deep as the line-of-site reaches the horizon (Young, 1994). More developed models exist that take into account the geometry of the Earth and refraction of the light as it passes through a non-homogeneous atmosphere, most notably the Kasten and Young (KY) (Kasten, 1965; Kasten and Young, 1989) empirical description of optical air mass which is written as

$$M_{KY}(\zeta) = \left[\cos\zeta + a \cdot (90 - \zeta + b)^{-c}\right]^{-1}, \tag{3.7}$$

where constants used in this formula are a = 0.50572, b = 6.07995° and c = 1.6364. These coefficients are empirically derived in Kasten and Young (1989).

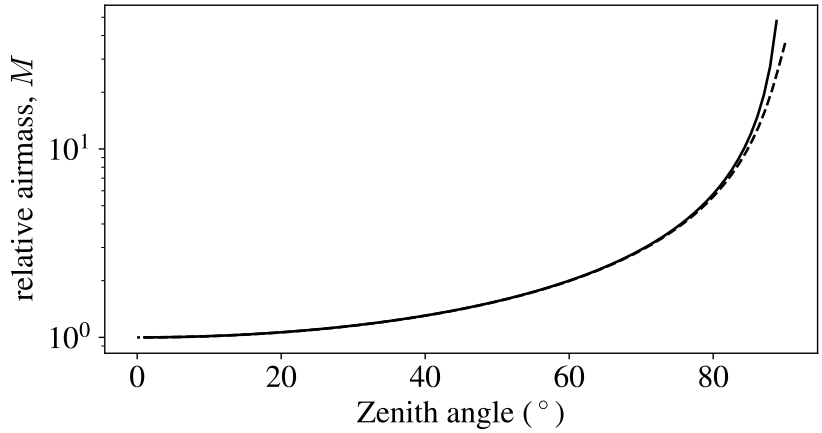

Figure 3.5: Relative air mass, M, as a function of zenith angle. Lines are made using equations 3.6 and 3.7, solid and dashed lines, respectively. The two equations agree well up until ∼83° where the secant theory tends to infinity and the KY theory tends to a maximum of 36.5.

Note that the two above equations only deviate at zenith values >80°, as seen in figure 3.5. However, it shall be used as needed throughout this document to avoid the flat Earth assumption.

3.2 Turbulence and laser propagation

Random fluctuations in the refractive index of air give rise to phase perturbations in the wavefront of optical and infrared electromagnetic waves. As the light continues to propagate, these phase perturbations evolve into intensity fluctuations, or *scintillation*. The combined impact of wavefront perturbations and intensity fluctuations can result in significant signal losses for optical communication links.

To better understand the effects of an extended turbulent medium on the propagation of a laser beam, the following two schematics are considered.

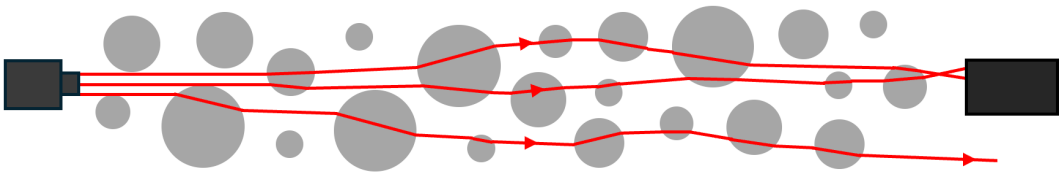

Figure 3.6: Schematic of a laser beam propagating from transmitter to receiver through a turbulent field. The red lines represent individual rays within the laser beam, while the grey circles symbolise turbulent cells, analogous to lenses in optical turbulence.

Figure 3.6 illustrates the propagation of a laser beam through a turbulent field. This schematic uses the analogy of turbulent cells behaving similarly to lenses along the propagation path, as seen in Andrews et al. (2001). As the laser travels through these turbulent cells, the direction of the rays deviates from the intended path. These changes in the ray direction cause portions of the laser beam to not be received, leading to a reduction in the received intensity.

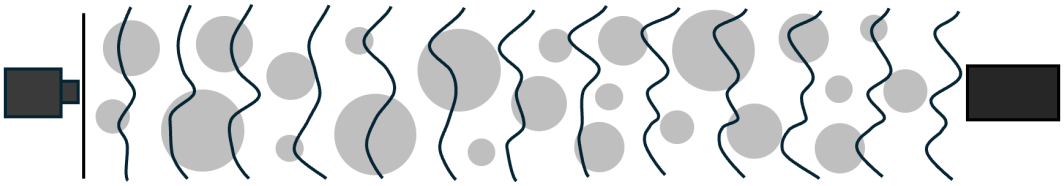

Figure 3.7: Schematic of a wavefront propagating from transmitter to receiver through a turbulent field. The black lines represent the wavefront, while the grey circles symbolise turbulent cells, analogous to lenses in optical turbulence.

Figure 3.7 illustrates the propagation of a wavefront through the same turbulent field. As the initially flat wavefront travels through these turbulent cells, the perturbations in the wavefront increase. These phase distortions affect the beam direction and how the light is received at the receiver. Distorted wavefronts are the mechanism that leads to a reduction in the number of photons reaching the receiver and also a reduction in the measured signal particularly for coherent detection systems (Belmonte et al., 2007). The consequences of these wavefront perturbations on signal reception are described further in section 3.2.1 and 3.2.3.

The study of the nature of laser beam propagation through turbulence has been a topic of significant interest for various fields, including astronomy, laser ranging, directed energy, and free-space optical communications (Roddier, 1999; Titterton, 2015; Spencer, 2020; Belmonte, 2000). This sustained interest has generated a substantial body of research, with one of the most seminal contributions in the field being Andrews and Phillips (2005).

In this section, the characterisation of atmospheric turbulence is explained and its implications on the optical propagation of a laser examined.

3.2.1 Atmospheric turbulence parameters

Here several parameters that are used in this document to describe both phase and intensity aberrations in the propagating light are discussed.

Scintillation

Light propagating through turbulent media will exhibit temporal and spatial variances in intensity, a phenomenon referred to as atmospheric scintillation. The metric used to parameterise scintillation is the scintillation index, denoted by σ_I^2 and is calculated by

$$\sigma_I^2 = \frac{\langle I^2 \rangle}{\langle I \rangle^2} - 1, \tag{3.8}$$

where I denotes the intensity of the optical wave.

Analytical expressions for the intensity fluctuations have been developed. For weak fluctuation regimes, where σ_I^2 is less than 0.3, the scintillation index is described by the Rytov variance, σ_R^2. For an unbound, plane wave, σ_R^2 can be derived directly from the measured turbulence strengths and their relative distances from the receiver (Bass, 1995):

$$\sigma_R^2 = 2.25 k^{7/6} H^{5/6} \sec^{11/6}(\zeta) \int_0^H C_n^2(h) H^{5/6} dh. \tag{3.9}$$

where H is the altitude of the maximum considered turbulent layer, typically considered to be 20 km, and k is the wavenumber of the optical wave, defined as $k = \frac{2\pi}{\lambda}$. Here the observer is assumed to be 0 m above ground.

For a path of length z and constant C_n^2, the σ_R^2 reduces to

$$\sigma_R^2 = 1.23 C_n^2 k^{7/6} z^{11/6}. \tag{3.10}$$

It is useful to use the Rytov variance as a metric for understanding when the optical wave is no longer exhibiting weak fluctuations. For a plane wave, weak fluctuations are typically associated with $\sigma_R^2 < 0.3$. Moderate fluctuations are associated with $0.3 < \sigma_R^2 < 1$ and strong characterisations by $\sigma_I^2 > 1$. These thresholds are based on both empirical observations and theoretical analysis which compare the derived Rytov variance with the scintillation index of a path (Andrews and Phillips, 2005; Andrews, 2019). Both moderate and strong fluctuations will be discussed in later sections.

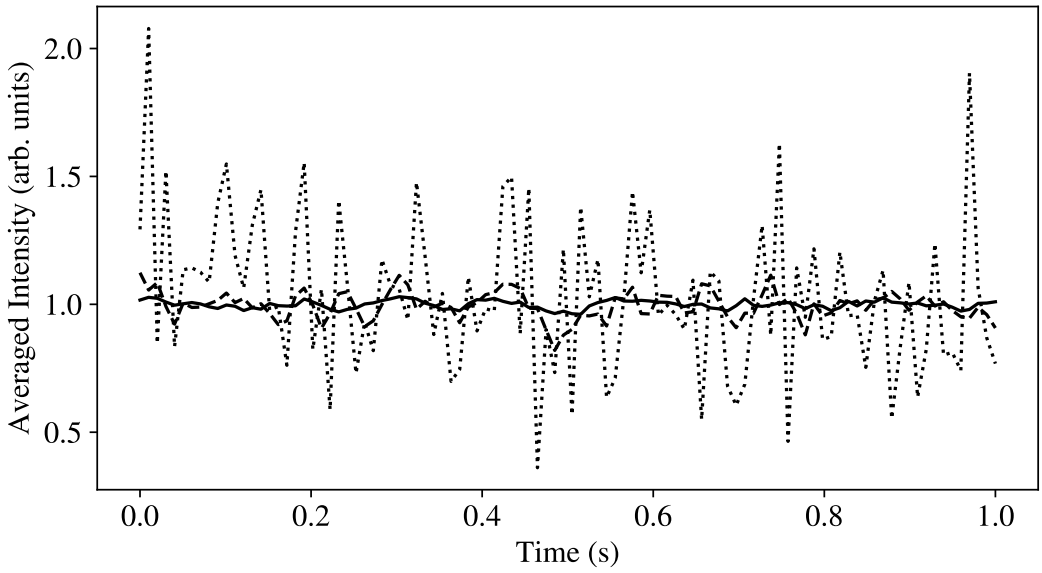

Figure 3.8: Temporal variation in the averaged intensity across the apertures of different sizes. Solid, dashed and dotted lines correspond to 50 cm, 20 cm and 5cm apertures, respectively.

The scintillation index can also be measured directly from the intensity fluctuations which can be input into equation 3.8. If the aperture of the receiver is smaller than the

width of spatial coherence of the intensity fluctuations, i.e. the intensity is the same across the aperture, then the receiver can be considered to be point-like. Here, the measured σ_I^2 equates to σ_R^2 if in the weak fluctuation regime. However, if the aperture is larger than the coherence width then the receiver will measure reduced intensity variance. Figure 3.8 demonstrates this averaging effect whereby the temporal stability in mean intensity across an aperture is highly dependent on aperture size. There is therefore an increase in the temporal variance and thus the scintillation index is much larger for smaller apertures. This phenomenon is an effective way to mitigate this form of signal degradation. Further details can be found in section 3.2.2.2, specifically in equation 3.27.

Fried parameter

The Fried parameter, r_0, can be used to measure the turbulence-induced phase aberrations of the light. It can be derived from the integrated atmospheric turbulence strength C_n^2 over the propagating path, written as (Tyson, 1991):

$$r_0 = \left[0.423k^2 \int_0^H C_n^2(h)\, dh\right]^{-3/5}. \tag{3.11}$$

It is also referred to as the coherence length and can be approximated as the aperture diameter over which there is 1 rad^2 of variance in the phase for Kolmogorov turbulence. This parameter is wavelength-dependent, and the values stated in this document are scaled to 500 nm unless otherwise noted. At astronomical observatories with very good seeing, r_0 can be as large as 20 cm in good conditions and around 5 cm in poorer conditions (Miller, 1997). As it is inversely proportional to the integrated C_n^2, it can be used to define the strength of turbulence.

The impact of r_0 on the optical system is dependent upon the diameter of the system's aperture, D. Following this, the ratio D/r_0 is used to estimate the effect of turbulence on the optical system. A heuristic interpretation of this ratio indicates that values of 0.1, 1, and 10 correspond to weak, moderate, and strong turbulent effects, respectively. Figure 3.9 shows simulated PSFs which represent each of the three regimes. The PSF

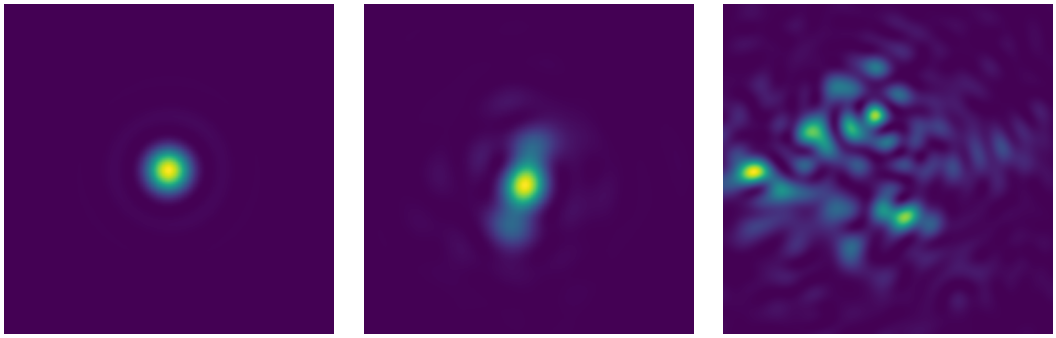

Figure 3.9: Simulated PSFs for three distinct turbulent regimes. All simulations use the same r_0 value of 10 cm, with varying aperture sizes. From left to right, the D/r_0 ratios are 0.1, 1, and 10, representing weak, moderate, and strong turbulent effects, respectively.

describes the response of an optical system to a point source or point object and is used to characterise the optical aberrations and performance of an optical system (Goodman, 1969). For a D/r_0 value of 0.1, the PSF nears the diffraction limit as the wavefront distortions are minimal enough over the small aperture to allow the system to perform close to the theoretical diffraction limit. As the D/r_0 value increases, the impact of atmospheric turbulence becomes more significant. For a D/r_0 value of 1, the wavefront distortions cause slight wander and aberrations in the PSF. As D/r_0 increases to 10, the PSF exhibits splitting, referred to as speckling, and significant wandering.

Isoplanatic angle

The isoplanatic angle, denoted by θ_0, is the angle over which the atmospheric turbulence is effectively constant. It can be approximated by Sechaud et al. (1999):

$$\theta_0 = \frac{r_0}{h}, \tag{3.12}$$

where h describes the altitude of the turbulent layer.

θ_0 is an important descriptor for the angle over which phase compensation can be successfully performed.

Coherence time

The coherence time, τ_0, describes the temporal stability of a turbulent layer. As the

development of turbulent eddies is much slower than the wind velocity of the layer, τ_0 can be described as:

$$\tau_0 = \frac{r_0}{v}, \tag{3.13}$$

where v is the wind velocity of the turbulent layer.

Similar to θ_0, τ_0 describes how your phase correction system will need to operate. For stationary targets in ideal conditions, τ_0 can be on the order of 10 ms. However, when the target is a non-geostationary satellite, the relative motion between the turbulent layer and the target is much faster, leading to a smaller coherence time. For example, correcting the phase for a Low Earth Orbit (LEO) satellite requires faster correction systems. A LEO satellite orbiting at an altitude of 500 km, such as TBIRD (see table 2.1), traverses the sky at an angular velocity of approximately 4°/s (Piazzolla et al., 2023). Figure 3.10 shows the effective wind speed (or layer velocity) and the effective coherence time for each turbulent layer tracking at 4°/s. It can be seen that the higher layers can have τ_0 values as short as 0.05 ms.

3.2.1.1 Zenith dependence of atmospheric turbulence parameters

The zenith corrections expressed in the following equations are derived through geometric scaling of the vertical height above the observer, h, to the increased propagation distance resulting from the increased zenith angle, z. The adjustment is performed using

$$\begin{aligned} z &= \sec(\zeta)h, \\ dz(\zeta) &= \sec(\zeta)dh. \end{aligned} \tag{3.14}$$

At high zenith angles, this correction introduces ambiguities stemming from assumptions of a flat Earth and a homogeneous atmosphere. To correct for this, $\sec(\zeta)$ scaling can be replaced with the more appropriate $M_{KY}(\zeta)$ (from section 3.1.2.1) in the following theory.

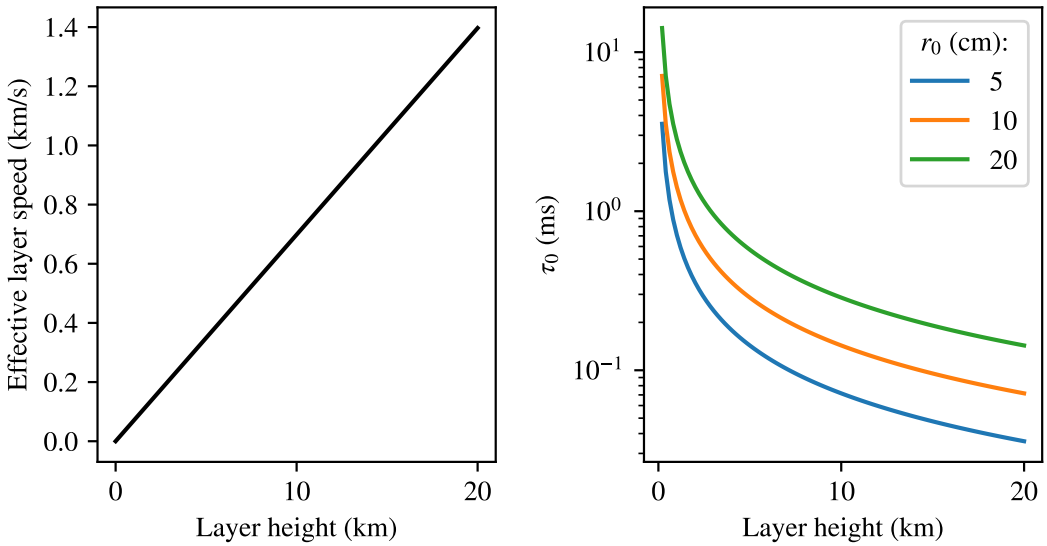

Figure 3.10: Effective turbulent layer velocity and coherence time for turbulent layers at varying altitudes when tracking a LEO satellite orbiting at 4°/s. (Left) Effective layer speed as a function of layer height. (Right) Coherence time as a function of layer height for three different r_0 values, derived using equation 3.13. This assumes the layer is stationary.

Scintillation

There are numerous analytical approaches to modelling scintillation generated from atmospheric optical turbulence.

For weak fluctuations, equation 3.9 can be modified to include the more complete air mass correction shown in equation 3.7, written as:

$$\sigma_R^2 = 2.25k^{7/6}M_{KY}(\zeta)^{11/6}\int_0^H C_n^2(h)h^{5/6}\,dh. \tag{3.15}$$

This demonstration aims to establish the relationship between σ_R^2 at zenith angle, ζ, denoted as $\sigma_R^2(\zeta)$, and σ_R^2 at the zenith, denoted as $\sigma_R^2(0)$. This is achieved by scaling them using the following expression:

$$\sigma_R^2(\zeta) = M_{KY}(\zeta)^{11/6}\sigma_R^2(0). \tag{3.16}$$

The use of equation 3.15 is only appropriate for weak fluctuations when σ_R^2 is less than 0.3. When entering stronger fluctuations, an alternative theory has been suggested by Andrews et al. (1999b):

$$\sigma_I^2 = \exp\left[\frac{0.49\sigma_R^2}{(1+1.11\sigma_R^{12/5})^{7/6}} + \frac{0.51\sigma_R^2}{(1+0.69\sigma_R^{12/5})^{5/6}}\right] - 1. \tag{3.17}$$

Equation 3.16 is used in combination with 3.17 to model strong fluctuations.

Fried Parameter

The generally accepted derivation of the Fried parameter at a specific zenith angle, ζ, is given by (Roddier, 1981):

$$r_0(\zeta) = \sec^{-3/5}(\zeta) r_0(0), \tag{3.18}$$

where $r_0(0)$ is the vertical Fried parameter measured at zenith and $r_0(\zeta)$ is the Fried parameter scaled to angle ζ.

Again, as shown above, this relationship can be improved by including the Kasten and Young's air mass correction:

$$r_0(\zeta) = M_{KY}(\zeta)^{-3/5} r_0(0). \tag{3.19}$$

3.2.2 Modelling laser propagation

There are many techniques used to model laser beam propagation through optical turbulence each with varying flexibility and convenience. This document utilises three main ways to model optical turbulence covering numerical models.

3.2.2.1 Laser propagation using phase screens

This numerical approach to optical propagation is best described in Schmidt (2010). This method has a significant advantage over the analytical approach as it is not confined to weak fluctuation regimes and there are many degrees of freedom to simulating

the optical system. Real, measured phase screens can be used to accurately represent the system's performance for a specific atmospheric state. Additionally, numerical simulations facilitate the application of the Monte Carlo method, enabling the identification of statistical information for the system. However, because of the runtime associated with this method, it may take several hours to achieve satisfactory statistical convergence. The simulation techniques used in this document are presented here.

The electromagnetic field of the propagating beam is described mathematically by its complex amplitude, Ψ (Born and Wolf, 2019):

$$\Psi(x, y, z) = A_0 \exp(-i\phi) \tag{3.20}$$

where A_0 and ϕ are the amplitude and phase of the beam respectively.

The description of the amplitude field of a propagating beam depends on the specific scenario of propagation. When observing light from stars, it's understood that by the time it encounters atmospheric turbulence—typically defined as occurring below altitudes of approximately 20 km—the amplitude and phase of the light can be modelled as an infinite plane wave. Similarly, when considering the propagation of laser beams from satellites to the ground, practical constraints such as mass and space limitations often result in small launch sizes for the downlink beam. Therefore, after traversing several hundred kilometres, the spread of the beam leads to the local approximation of a planar wave at the top of the atmosphere (Tatarski, 1961).

For the launch from a ground-based transmitter, the laser shall be modelled as a gaussian beam, where the irradiance profile, $I(r)$, is defined by (**?**):

$$I(r) = I_0 e^{-2r^2/w_0^2}, \tag{3.21}$$

where I_0 is the intensity at the centre of the beam, r is the radial position and w_0 is the beam waist, defined as the distance between the peak and the point at which the intensity drops to $1/e^2$ of its maximum value. The effect of this shape on the propagation of the beam will be discussed below. Other beam profiles such as Bessel beams or

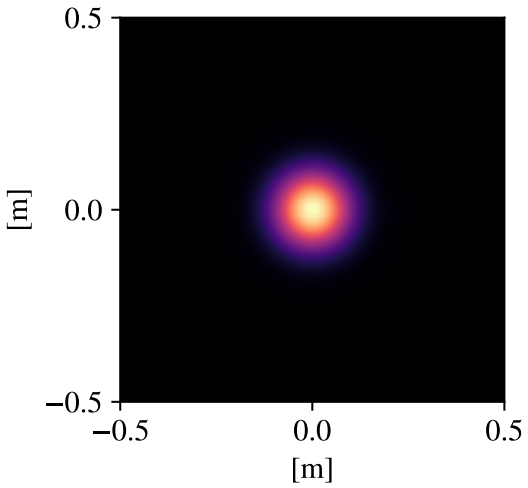

Figure 3.11: An example of the initial intensity of a propagating Gaussian beam used in simulations. Here, the Gaussian beam has a beam waist of 10 cm. The maximum value of the amplitude is set to 1.0.

Laguerre-Gaussian beams can also be used. Examples of the Gaussian intensity profiles that are used in simulation are shown in figure 3.11.

The beam can be propagated over a distance of Δz using the Fresnel propagation method (Goodman, 1969):

$$\begin{aligned}\Psi(x, y, z + \Delta z) &= \Psi(x, y, z) \otimes \left[\frac{e^{ik\Delta z}}{i\lambda\Delta z} e^{i\frac{k}{2\Delta z}(x^2+y^2)} \right] \\ &= \Psi(x, y, z) \otimes \mathcal{F}_{\Delta z}(x, y)\end{aligned} \tag{3.22}$$

where $\otimes$ is the convolution product and $\mathcal{F}_{\Delta z}$ represents the Fresnel integral.

In this work, the Fresnel propagation algorithm is used to simulate beam propagation over large distances, such as between the top of the atmosphere and the satellite. For shorter distances, the angular-spectrum method is employed. These two methods are most accurate across their respective distance ranges (Southwell, 1981; Schmidt, 2010). These propagation algorithms are performed using the Python package AOTools (Townson et al., 2019).

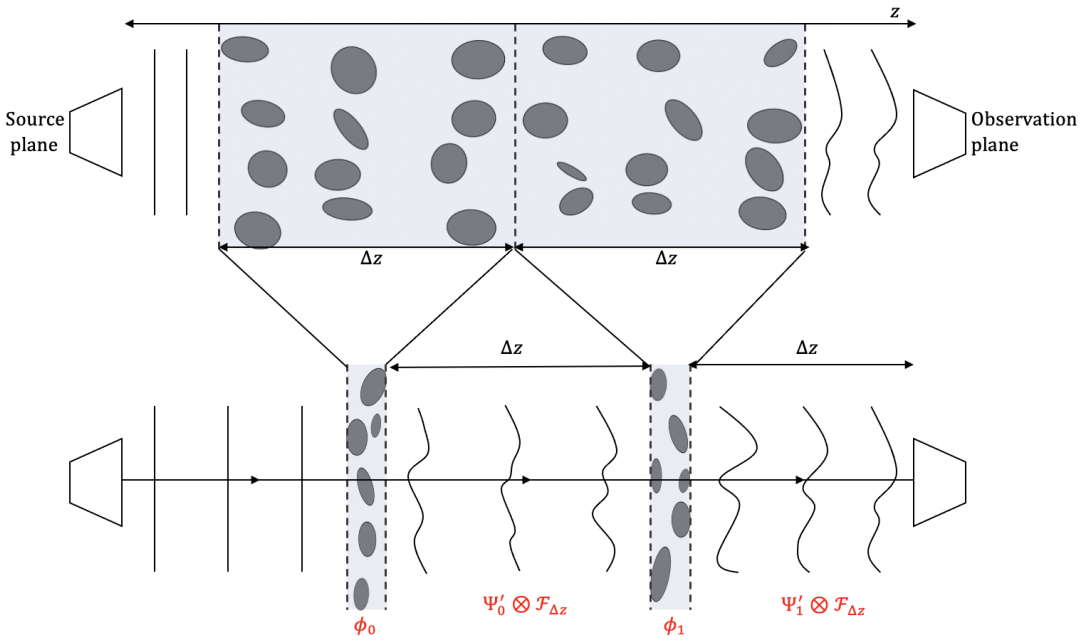

Figure 3.12: Schematic showing the process of phase screen propagation between a transmitter and receiver. The turbulence is presented as both an extended medium (top) and as several phase screens (bottom). Lines perpendicular to the propagation path represent the wavefront of the laser. The relative mathematical symbols for each portion of propagation have been written in red.

The phase screen method of propagation divides the atmospheric turbulence into several turbulent sections (Andrews and Phillips, 2005). Each section is then represented as a series of thin, statistically independent, turbulent layers called phase screens. Phase screens are assumed to be thin enough so that propagation within the layer can be considered negligible. Figure 3.12 illustrates this process. Propagation between layers is assumed to be through a vacuum, shown as the following (Goodman, 1969):

$$
\begin{aligned}
\Psi_0(x,y,z) &= A_0 \cdot e^{(-i\phi_0)} \\
\Psi_0'(x,y,z) &= \Psi_0(x,y,z) \cdot e^{-i\phi_1(x,y,x)} \\
\Psi_1(x,y,z+\Delta z) &= \Psi_0'(x,y,z) \otimes \mathcal{F}_{\Delta z}(x,y) \\
\Psi_1'(x,y,z+\Delta z) &= \Psi_1(x,y,z+\Delta z) \cdot e^{-i\phi_2(x,y,z+\Delta z)} \\
\Psi_2(x,y,z+2\Delta z) &= \Psi_1'(x,y,z+\Delta z) \otimes \mathcal{F}_{\Delta z}(x,y) \\
&\dots \\
\Psi_n(x,y,z+n\Delta z) &= \Psi_{n-1}'(x,y,z+(n-1)\Delta z) \otimes \mathcal{F}_{\Delta z}(x,y)
\end{aligned}
$$

where n describes the number of phase screens between the source and observation plane.

The full turbulent distribution can be modeled using only N equivalent layers, referred to as the Equivalent Layers Method (Fusco et al., 1999). In this method, the true C_n^2 distribution is divided into N turbulent slabs, with each slab being represented by a single turbulent layer. When these layers are placed at the correct heights, they preserve the observed turbulent conditions. Each layers's equivalent integrated turbulence strength, corresponding to $C_n^2 dh$, is calculated by:

$$C_n^2 dh = \int_{h_{\min}}^{h_{\max}} C_n^2(h)\, dh, \tag{3.23}$$

where $h_{\min}$ and $h_{\max}$ are the minimum and maximum heights of the layer, respectively.

For each turbulent slab, an equivalent layer is placed at an equivalent height h_{eq}, defined as the weighted mean height of the turbulent slab:

$$h_{\text{eq}} = \frac{\int_{h_{\min}}^{h_{\max}} C_n^2(h)\, h\, dh}{\int_{h_{\min}}^{h_{\max}} C_n^2(h)\, dh}. \tag{3.24}$$

with an associated r_0:

$$r_0 \sim \left(\int_{h_{\min}}^{h_{\max}} C_n^2(h)\, dh \right)^{-3/5} \tag{3.25}$$

The model can be used to derive the r_0 values for phase screens that can be placed at heights h_{eq} which will successfully replicate the turbulent conditions using a full turbulent distribution. In doing so, the computational demands for simulating a single atmospheric instance are reduced.

The temporal evolution of turbulence can be conceptualised through Taylor's frozen flow hypothesis, which suggests that turbulence evolves at a slower rate than the horizontal translation caused by wind velocity. To simulate this, each phase screen can be shifted horizontally, emulating a specific wind speed. By doing so the temporal turbulence statistics can be studied.

The phase screen generation are simulated in this report via AOtools (Townson et al., 2019). The phase screens are based on the Von Karmán power spectrum which allows for the inclusion of outer and inner length scales.

3.2.2.2 Analytical descriptions

Over half a century of academic research has been dedicated to building analytical models of atmospheric turbulence and how light propagates through it (Tatarski, 1961; Fried, 1967; Young, 1970a,b). While this document primarily utilises a phase screen Monte Carlo approach to model optical systems, analytical descriptions of turbulence can offer valuable insights for quick system characterisation. Given the extensive body of literature, the focus will be on analytical models specific to the scope of this document: specifically, scintillation in varying aperture sizes and under strong fluctuation conditions. For more comprehensive analytical derivations, readers are referred to Andrews and Phillips (2005).

Statistical understanding of intensity fluctuations generated by turbulence can be successfully modelled by the Rytov variance, described in equations 3.9 and 3.10. Both of these equations suggest that the scintillation tends to infinitely under strong perturbations. However, both observations and simulations have shown that after some

propagation distance, scintillation reaches a maximum and then begins to decrease, this is referred to as saturation. Literature states that the cause of this phenomenon is due to the lateral spreading of high-order intensity fluctuations with optical propagation (Young, 1970a). It is also said to be caused by multiple scattering events occurring along an extended medium leading to an averaging effect (Andrews et al., 1999a). Both explanations are plausible, suggesting that saturation may result from a combination of these factors.

Physically, weak fluctuations occur when the propagating wave has a longer wavelength or when the integrated atmospheric turbulence strength is weaker such as at smaller zenith angles or travelling over short propagating paths. Where stronger fluctuations are reached, an alternative theory has been suggested by Andrews et al. (1999b):

$$\sigma_I^2 = \exp\left[\frac{0.49\sigma_R^2}{\left(1+1.11\sigma_R^{12/5}\right)^{7/6}} + \frac{0.51\sigma_R^2}{\left(1+0.69\sigma_R^{12/5}\right)^{5/6}}\right] - 1. \tag{3.26}$$

Figure 3.13 shows a comparison between the weak and strong fluctuation theories. These distributions are made using the Hufnagel-Valley turbulence distribution with the ground layer C_n^2 equal to 1.7×10^{-14} m$^{-2/3}$ (Andrews et al., 2009). The wavelength is 500 nm. For this particular set of optical parameters, there is an initial agreement between the two theories up until 40°. The extent of this divergence between the two theories depends on the propagating wavelength and the specific conditions of the optical turbulence. The weak theory exhibits exponential growth as the zenith angle increases. In reality, however, scintillation reaches a point of saturation as observed in the strong fluctuation model.

The other scintillation model that is useful to this document is the expected aperture averaged scintillation index. Again, this model is found in Andrews and Phillips (2005) and is written as:

$$\begin{aligned}\sigma_I^2(D_G) = {} & 8.7k^{7/6}H^{5/6}\sec^{11/6}(\zeta) \\ & \times \mathrm{Re}\int_0^H C_n^2(h)\left[\left(\frac{kD_G^2}{16h}+i\frac{h}{H}\right)^{5/6} - \left(\frac{kD_G^2}{16h}\right)^{5/6}\right]dh,\end{aligned} \tag{3.27}$$

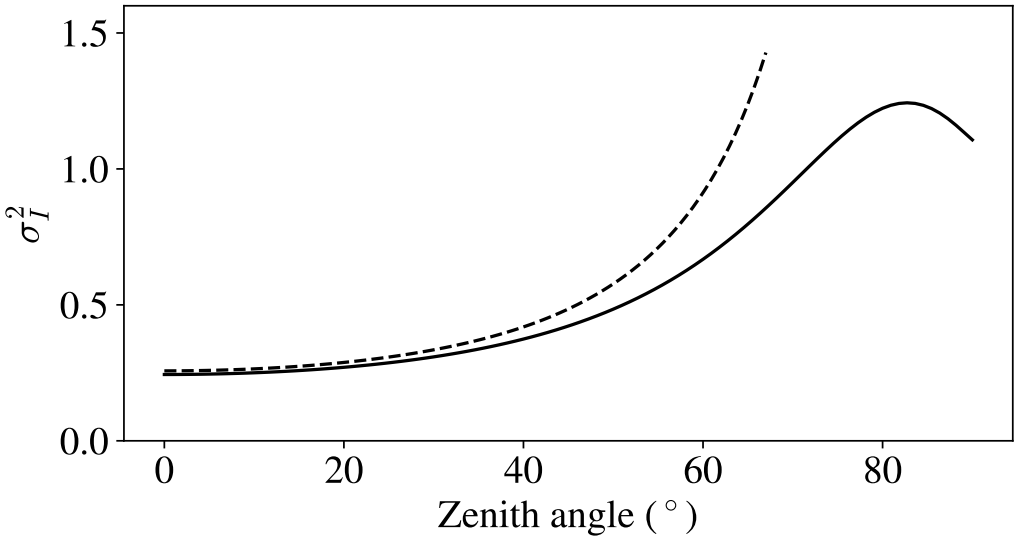

Figure 3.13: The downlink scintillation index as a function of zenith angle. The dashed line uses the weak-fluctuation theory from equation 3.15 and the solid line uses the strong-fluctuation theory from equation 3.26. The Hufnagel-Valley turbulence distribution is used here, with the ground layer C_n^2 equal to 1.7×10^{-14} $\mathrm{m}^{-2/3}$ with a wavelength of 500 nm (Andrews et al., 2009).

where D_G is the diameter of the aperture and it is assumed that the observer is at 0 m.

3.2.3 Turbulent effects on optical propagation

Previous sections explored how turbulence can cause phase and intensity fluctuations in a propagating beam. This section will discuss the specific effects of optical turbulence on a communication channel and strategies for optimising optical systems to mitigate these effects. All results presented here are simulated using the method described in section 3.2.2.

Beam divergence

Even in the absence of optical turbulence, optical propagation leads to signal loss due to beam divergence based purely on diffraction. The beam divergence is inversely

proportional to the size of the beam waist at the transmitter, which is expressed as (Svelto, 1998):

$$w(z) = \frac{\lambda z}{\pi w_0} \tag{3.28}$$

where $w(z)$ is the beam waist at propagation distance z and w_0 is the initial beam waist.

This is seen in figure 3.14, where three different Gaussian beam launch sizes are propagated over 2,000 km. The smallest of the three exhibits a much larger beam divergence. Note the differences in axis scales.

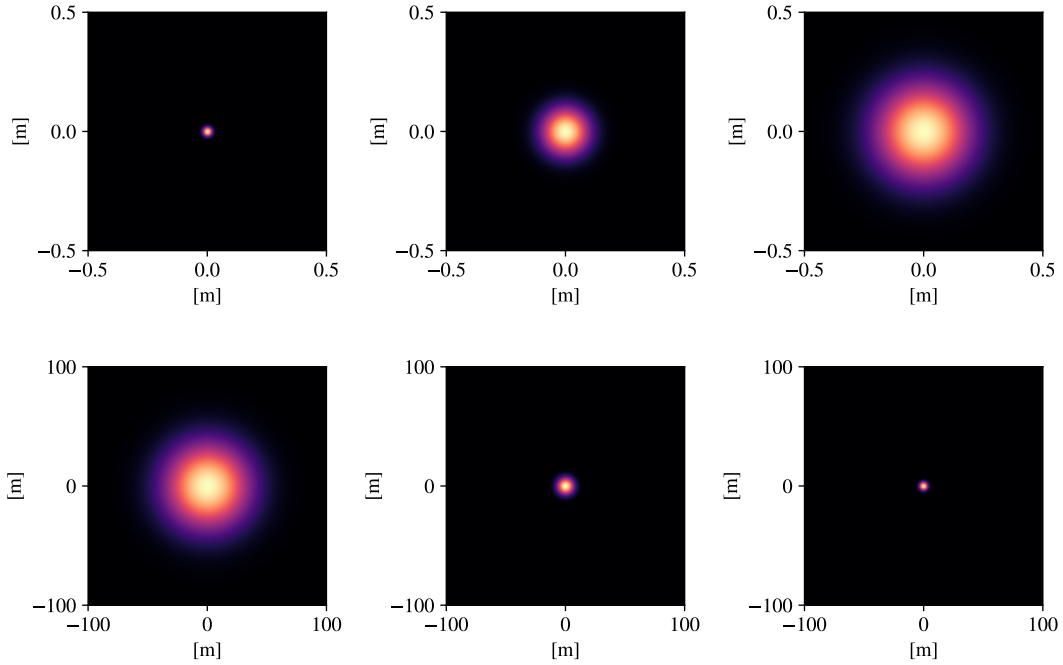

Figure 3.14: Propagation of Gaussian beams through vacuum with varying w_0. Normalised z-scale, where each maximum amplitude is 1. (Top) Beams before propagation, from left to right w_0 of 2 cm, 10 cm and 20 cm. (Bottom) Same beams but propagated to LEO altitude of 2,000 km.

This effect can be advantageous in instances where the receiver's position is not accurately known, such as in certain cases of ground-to-satellite optical communications. The beam divergence increases the probability of successful reception. Additionally, a

smaller beam size can minimise interaction with ground-layer optical turbulence. However, in cases where high data rates are required, limiting divergence may be desirable to ensure a larger flux reaches the receiver. Nevertheless, such systems may become more sensitive to turbulent effects.

Beam wander

Beam wander refers to the displacement of the centroid of the beam in the radial axis from its initial position as it propagates through turbulence. The primary mechanism that causes beam wander is low-order fluctuations in the phase. Wavefront aberrations can be quantitatively analysed using Zernike polynomials. These polynomials form an orthogonal set on the unit disk and are used to describe optical aberrations (Born and Wolf, 2019). Figure 3.15 illustrates the first 15 Zernike polynomials. The first-order terms, known as tip (Z_1^1) and tilt (Z_1^{-1}), introduce horizontal and vertical gradients, respectively, to the wavefront. As the wavefront propagates, these gradients induce displacements in the centroid of the beam, causing beam wander.

Figure 3.16 depicts instantaneous beam wander at the satellite generated by ground-layer turbulence which evolves temporally. The simulated wind speed of the ground layer is 5 ms^{-1} which can be seen to create a large displacement of the centroid even over short time scales.

Additionally, figure 3.17 shows the spot size of a beam over a long exposure for varying ground layer strengths. Here, the variation in the long exposure spot size is due to the increased beam wander with stronger optical turbulence.

This form of signal degradation predominantly affects the uplink due to the large propagation distance, requiring correction to prevent a reduction in signal strength or complete signal loss.

Angle of arrival

The angle of arrival is the mean angle at which the phase of the light is as it reaches

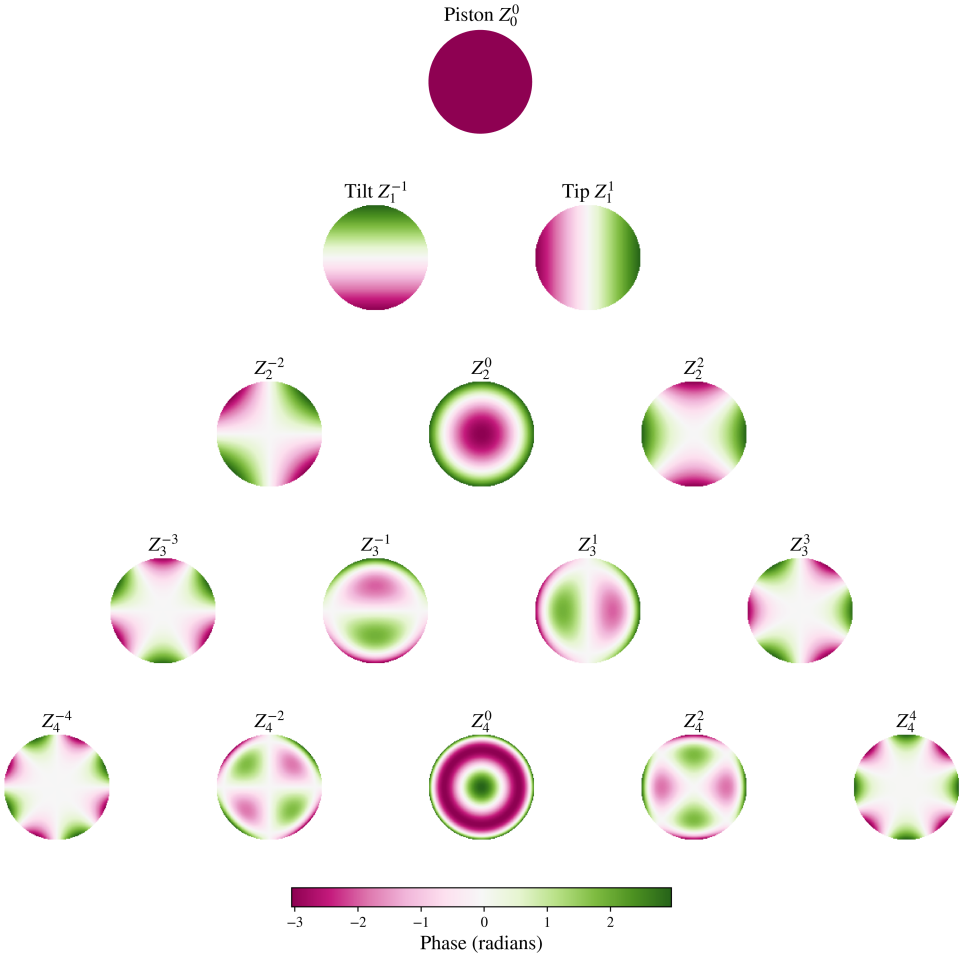

Figure 3.15: The first 15 Zernike polynomials. Ordered vertically by the degree of aberration and horizontally by azimuthal frequency.

the receiver. As this light is focused, variations in phase in the pupil plane can cause the focal point to shift around the centre. Figure 3.18 illustrates this effect over three turbulent regimes, showing both short and long-exposure images. For smaller r_0, it can be seen that the angle of arrival causes the focal point to deviate from the centre of the image.

In the context of FSOC, this form of signal degradation has a particular prevalence in downlinks and any ground-to-ground terrestrial links as these channels are where the phase will exhibit the strongest perturbations. For uplink, the initial phase perturbations at the ground become flatter with the expansion of the beam and it can be

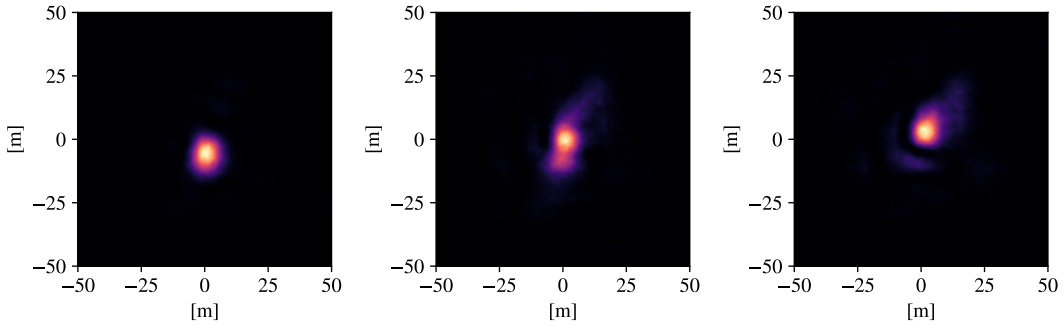

Figure 3.16: Short exposure of the intensity profile of a collimated Gaussian beam with an initial w_0 of 10 cm propagating to a LEO-satellite at 2,000 km. A single layer of turbulence is applied at the ground with an r_0 of 10 cm. Normalised z-scale, where each maximum amplitude is 1. From left to right, the temporal evolution of the beam wander at 0 ms, 20 ms, and 40 ms is shown. The turbulent layer has been simulated to have a wind speed of 5 ms^{-1}.

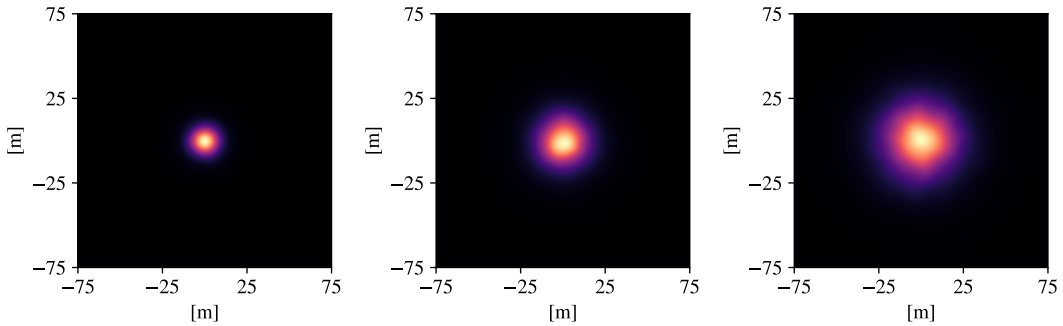

Figure 3.17: Long exposure intensity profiles of a collimated Gaussian beam with an initial w_0 of 10 cm propagating to a LEO-satellite at 2,000 km. Normalised z-scale, where each maximum amplitude is 1. From left to right, the ground layer turbulence strength is generated with r_0 of 20 cm, 10 cm and 7 cm, respectively.

assumed in cases that the phase is flat at the receiver. In cases where coupling light into an optical fibre is required, the angle of arrival may prevent proper focusing of light leading to signal losses.

3.2.4 Strong perturbations

So far, some of the most common consequences of optical turbulence on the propagating beam have been observed. These effects occur under weak turbulence conditions

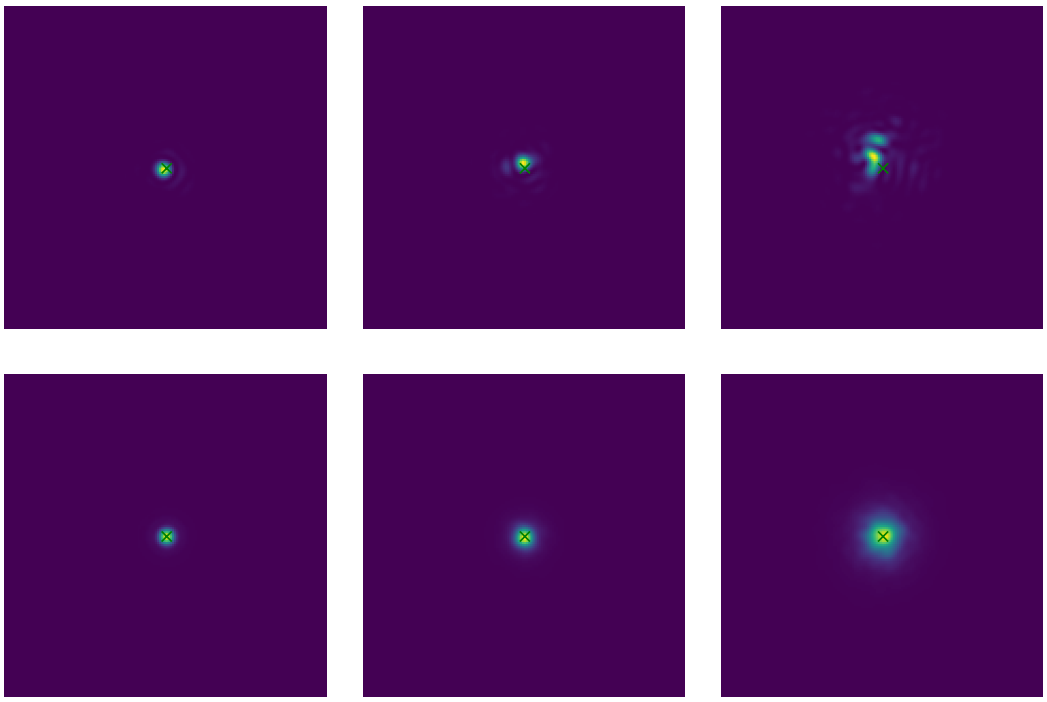

Figure 3.18: Impact of the angle of arrival on the centroid in the focal plane of an optical system. From left to right, the r_0 is 20 cm, 10 cm, and 5 cm, corresponding to a D/r_0 ratio of 1, 2, and 4. (Top) Instantaneous position of the focused light. (Bottom) Long exposure images of the focused light. The green cross represents the centre of the image.

and are well understood both in their modelling and how to correct them. However, as stronger perturbations occur with longer propagation distances and increased refractive index fluctuations along the path, the behaviour of the light becomes more complex to model. As seen in section 3.2.2.2, the analytical models for entering the strong perturbation regime are non-trivial. However, it is still possible to model these perturbations numerically.

Figure 3.19 illustrates the intensity fluctuations, or speckle patterns, across a 2.5 m screen under varying σ_R^2, corresponding to weak, moderate, and strong perturbations. In all patterns, granulations of varying sizes are observed, with larger granules (or spatial frequencies) in the intensity corresponding to increased σ_R^2. For strong perturbations, filament-like shapes appear with increasing anisoplanatism in the intensity

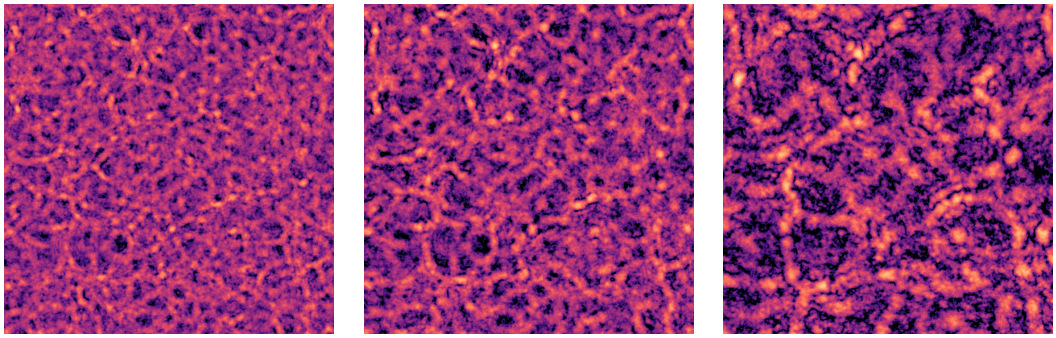

Figure 3.19: Scintillation patterns for perturbations of varying strengths, axis of 2.5 m used. From left to right, σ_R^2 of 0.3, 1 and 6. Specific σ_R^2 were generated using the same turbulence strength but propagated at different distances. The same phase screen was used to generate all 3 patterns. Simulated with a λ of 1550 nm and plotted on a logarithmic scale.

profile.

3.3 Mitigating optical turbulence using adaptive optics

AO uses mechanical means to correct for turbulence in real time. As illustrated in figure 3.20, a basic AO system typically consists of three main components: a wavefront sensor, a deformable mirror, and a control system (Roddier, 1999). The wavefront measures the distortions caused by atmospheric turbulence, while the control system alters the shape of the deformable mirror to correct for these distortions, effectively 'flattening' the wavefront (Tyson, 1991). The deformable mirror is deformed to match the shape of half the input light's wavefront. Any aberration which remains after the light interacts with the deformable mirror is referred to as the residual phase. For a closed-loop adaptive optics system, this residual phase is then measured using a wavefront sensor. Using these residual wavefront measurements, the control system then iteratively reshapes the deformable mirror to continue correcting the phase.

The removal of wavefront aberrations leads to an improved angular resolution in imaging systems, which is crucial for applications such as astronomy and microscopy

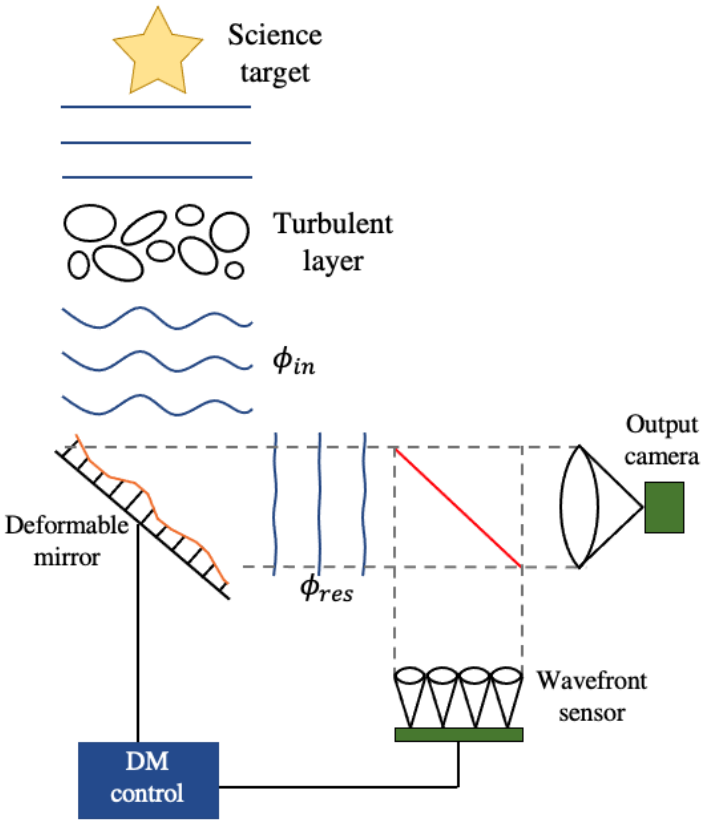

Figure 3.20: Schematic of a closed-loop adaptive optics system.

(Booth, 2007). In the context of FSOC, this phase correction allows more light to be precisely focused into an optical fibre, thereby increasing coupling efficiency and significantly reducing signal losses caused by atmospheric turbulence.

The extent of phase correction performed by adaptive optics is dependent on the specific needs of the system. Tip/tilt only AO is designed to remove low-order aberrations in the phase, correcting for the mean gradient (or tilt) in the wavefront. Full AO systems work to remove both high- and low-order phase perturbations. Full AO systems are much more computationally expensive than tip/tilt AO, and the increase in system performance is not always proportional. Therefore, the choice AO system should be optimised on a case-by-case basis.

To measure the shape of the wavefront there must be a sufficiently bright source to

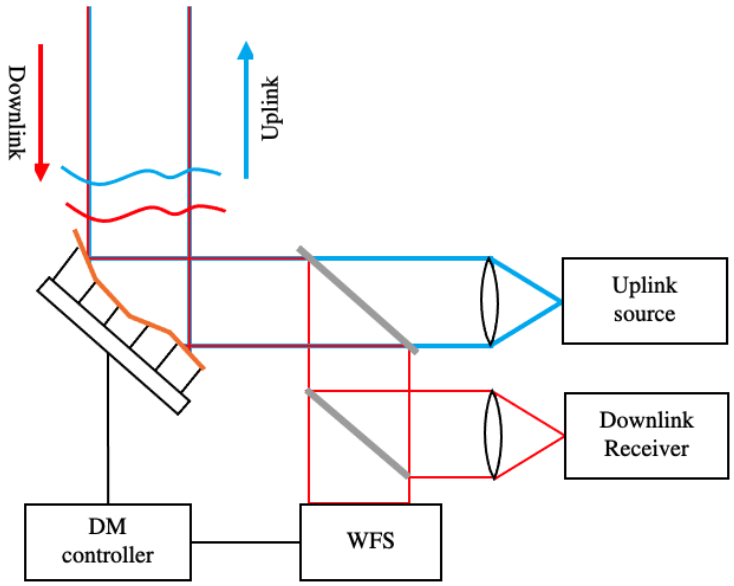

Figure 3.21: Schematic of the precompensated uplink using the Deformable Mirror (DM) from the downlink.

illuminate the wavefront sensor over short exposure times. In certain instances in astronomy, the target itself may provide sufficient brightness for wavefront measurements. If not, wavefront sensing relies on guide stars, which can be either a Natural Guide Star (NGS) or a Laser Guide Star (LGS). For downlink FSOC, the communication beam itself may be a bright enough source to measure the wavefront.

To mitigate the effect of optical turbulence on the propagation of an uplink beam, adaptive optics can be used to predistort the wavefront at the launch (D. L. Fried, 1971). This form of turbulence mitigation is called precompensation and takes advantage of the reciprocity of some atmospheric channels whereby the atmospheric channel is the same on the downlink beam as it is for the uplink beam. The added distortions to the wavefront will cancel the aberrations of the wavefront as it propagates, effectively achieving an unaberrated wavefront at the top of the atmosphere. Precompensation prevents scintillation in the propagating beam, a capability which is not possible with a simple AO system at the receiver.

In some AO configurations, the wavefront can be precompensated by using the same deformable mirror that is used for correcting the downlink wavefront aberrations, as shown in figure 3.21. This form of mitigation is limited by the Point-Ahead Angle (PAA) between the downlink beam and the uplink beam, whereby the atmospheric channels can no longer be considered reciprocal (see figure 3.22). As a satellite moves, it traverses an angle between laser transmission and reception, known as the point ahead angle. This movement can either be to match the rotation of the Earth as with GEO or can be due to its orbital motion as in LEO. The PAA for GEO satellites is around 4" and for LEO around 10". If the point ahead angle is much larger than the isoplanatic angle, this leads to anisoplanatism, and there will be reduced knowledge of the characteristics of the uplink's propagating channel which worsens the effectiveness of phase precompensation on the uplink.

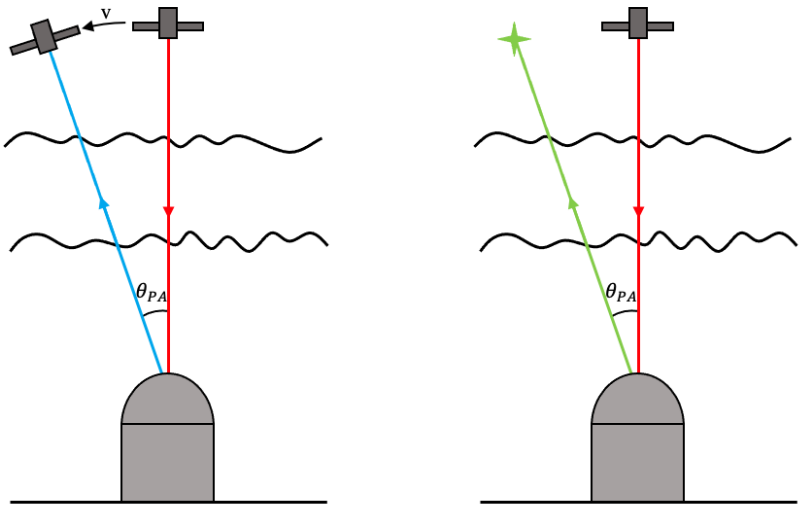

Figure 3.22: (Left) Point-ahead angle between the downlink beam and the uplink beam. (right) Laser guide star being used at the point-ahead angle for

The PAA effect can be mitigated by using a LGS that will be pointed at the PAA, probing the atmospheric channel that will be used by the uplink beam, shown in figure 3.22. A separate AO system can measure the wavefront of the LGS and predistort the uplink beam. As LGS's are unable to measure the tip/tilt and defocus of the wavefront

the from the downlink beam can be used in place.

As adaptive optics systems have been developed to be used at astronomical sites, conventional systems are only designed to operate under weak turbulence conditions. However, as adaptive optics is one of the most promising ways to correct the perturbations within the wavefront, the operational performance in strong turbulence regimes must be discussed.

Alternative methods for mitigating the effects of atmospheric turbulence include various innovative approaches. One effective technique is the use of multi-aperture transmitting systems, which can help average out the effects of turbulence over multiple paths, thereby improving the overall signal quality (Jiang et al., 2020). Another approach involves digital signal processing techniques, such as retransmitting the same data if a fade is detected, which ensures data integrity despite turbulent conditions (Schieler et al., 2022). Additionally, different modulation techniques that are inherently more resistant to turbulence have been explored. For example, orbital angular momentum (OAM)-based modulation has shown promise in maintaining signal integrity under turbulent conditions, enabling robust communication over long distances. This technique has been demonstrated to support high data rates and large numbers of channels, making it a viable solution for mitigating turbulence effects (Li and Wang, 2017; Qu and Djordjevic, 2016).

Wavefront sensing under strong scintillation

A common wavefront sensor used in adaptive optics is the SHWFS (Tyson, 1991). It consists of an array of small lenses, called lenslets, arranged in a grid pattern. Each lenslet within the array focuses the light onto a camera sensor, referred to as a spot. The displacement of the spots across the camera is proportional to the gradient of the wavefront at the receiver. A spot pattern of an evenly illuminated Shack-Hartmann sensor is shown in figure 3.23.

In more challenging turbulent scenarios, such as propagation over long distances, the

laser beam can experience strong scintillation, as seen in Primmerman et al. (1995) and Marchi and Scheifling (2012). Scintillation induces intensity variance across the SHWFS, which can cause the spots to be either too bright or too dark, as shown in figure 3.24. Due to the finite dynamic range of the wavefront sensor camera, this variance can lead to pixel saturation when the spots are too bright, or cause the spots to fall below the detector's background noise level when they are too dim, rendering the signal undetectable. Without accurate spot position data, wavefront reconstructions become unreliable.

The change in spot brightness depends on the size of the lenslets in the SHWFS. Larger lenslets collect light over a larger area, which can increase the brightness of the spots, making saturation more likely. Conversely, smaller lenslets result in dimmer spots, which reduces the likelihood of saturation but increases the risk of the spots being undetectable if the intensity falls below the noise threshold.

The diagram in figure 3.25 demonstrates how the centroiding of a spot worsens under strong scintillation conditions. It compares the normal operation of the centroiding algorithm with scenarios where saturation and lack of light adversely affect the accuracy. Under normal conditions, the centroiding algorithm accurately detects the spot's position. However, in the presence of strong scintillation, saturation can lead to inaccurate position measurements, while insufficient light can prevent the spot from being detected altogether.

Without the centroid information for these subapertures, the feedback loop used in the AO system will be faulty, thus preventing accurate measurements of the wavefront. Methods have been suggested to compensate for these fades in signal, such as the use of a pyramid wavefront sensor, which can operate over a larger dynamic range and is thus less sensitive to scintillation (Ragazzoni, 1996; Biasi et al., 2023). The use of a spatial light modulator instead of a SHWFS has also been suggested in Lechner et al. (2020), whereby the lenslet sizes can adapt, becoming larger or smaller depending on

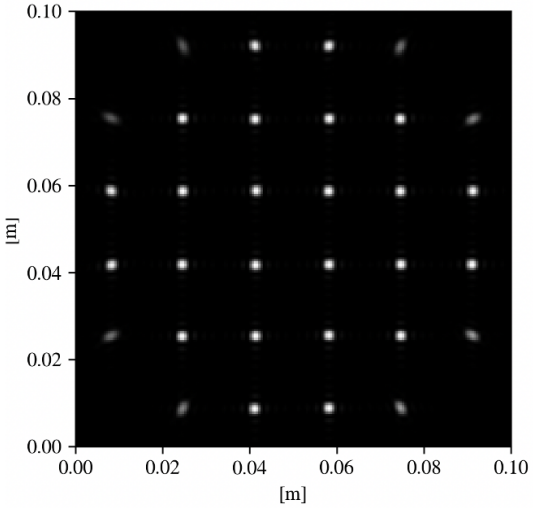

Figure 3.23: SHWFS spot pattern for an aperture under even illumination.

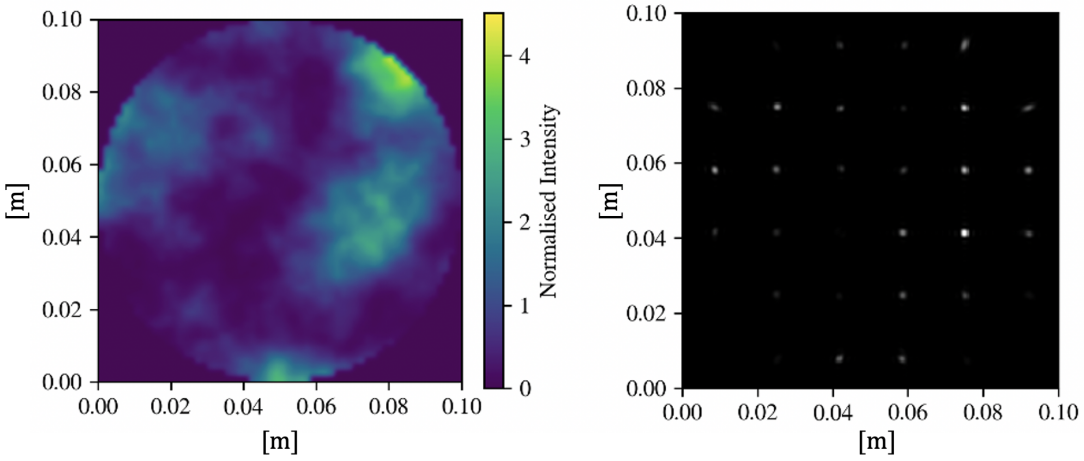

Figure 3.24: (Left) Normalised intensity pattern for a 15 km propagation of moderate turbulence. (Right) The corresponding spot pattern for the received intensity. Note the variation in the brightness of the spots across the aperture.

the received signal.

Branch points

When an electromagnetic wave undergoes strong perturbations instances of zero amplitude occur. A dislocation forms in the phase referred to as a branch point or cut occurs, as seen in figure 3.26. If such a dislocation occurs, the shape of a conventional deformable mirror will not be able to correct for this leading to signal losses.

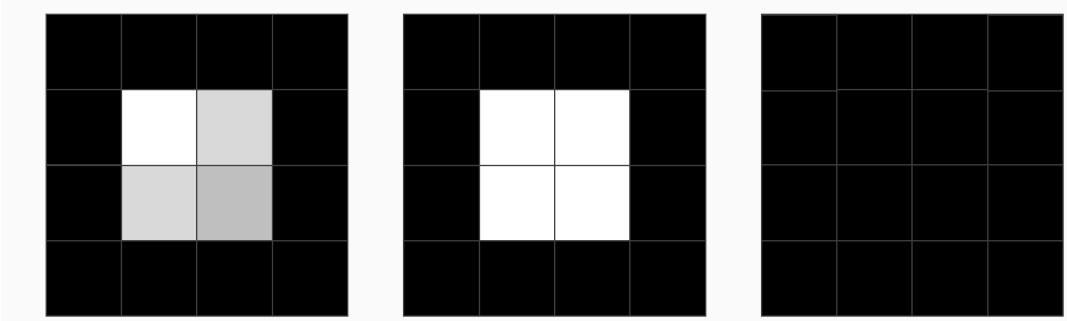

Figure 3.25: Diagram showing the effect of scintillation on the centroiding of a spot for a 2 by 2-pixel array. (Right) Normal operation of the centroiding algorithm where the spot is accurately detected. (Centre) Saturated spot causing loss of positional accuracy. (Left) Absence of a spot due to insufficient light in the lenslet.

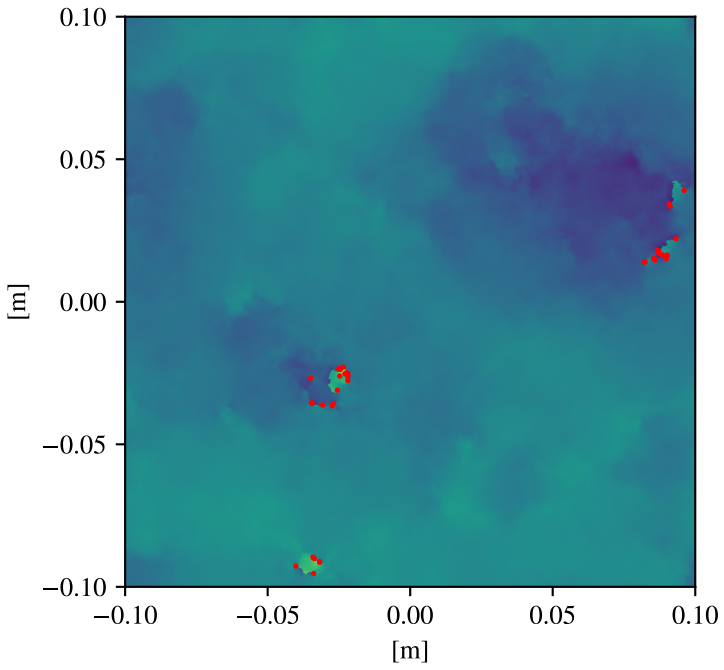

Figure 3.26: Branch points forming on the EM field of a 5 cm r_0 phase screen that has been propagated 1 km. The positions of the branch points are shown in red. Here the phase has been unwrapped to make the discontinuities clearer.

3.3.1 Adaptive optics simulation

The adaptive optics simulations performed in this thesis use Fourier Domain Adaptive Optics Simulation Tool (FAST). FAST employs analytical methods to derive the power spectral density (PSD) of residual phase errors from AO systems (Farley et al., 2022). This involves calculating the contributions of various AO error terms such as fitting, anisoplanatism, servo-lag, aliasing, and noise. These calculations are performed in the Fourier domain, enabling the determination of long-exposure PSFs with high computational efficiency.

The tool then uses numerical techniques to generate random phase screens based on the analytically derived PSDs. This is done via inverse Fast Fourier Transform (FFT) methods, allowing for the creation of realistic turbulence simulations. Monte Carlo methods are employed to model the statistical behaviour of light propagation through these screens.

FAST uses several AO parameters to evaluate and enhance system performance, including specific AO mode, WFS type and pitch, DM pitch, loop rate, and wavefront sensor (WFS) noise. In this thesis, the parameters are chosen to realistically represent the AO system's capabilities:

- **WFS type:** The Shack-Hartmann wavefront sensor is widely utilised and well-developed in adaptive optics.
- **WFS pitch:** Using an 8x8 subaperture Shack-Hartmann wavefront sensor has be used in FSOC AO systems, as demonstrated by FEEDELIO (Montmerle-Bonnefois et al., 2019). With this configuration, the WFS pitch is determined by dividing the receiver diameter by 8. For example, for a 40 cm receiver, the WFS pitch is 5 cm.
- **WFS noise:** As described in Farley et al. (2022), the WFS noise is assumed to be negligible compared to the laser signal.

- **DM pitch:** The DM pitch is set to match the WFS pitch. This alignment ensures that the actuators on the DM correspond directly to the subapertures of the WFS. Matching the pitches simplifies the control algorithms, increasing the efficiency of the AO system.

- **Loop rate:** The loop rate of an AO is typically on the kHz scale. For a closed-loop AO system, achieving a flat wavefront requires a strong correlation between the incoming wavefront and the shape of the deformable mirror (DM). Given that the coherence time, typically around 10 ms, dictates how long this correlation remains effective, the AO loop must operate at a significantly higher rate, approximately 1 kHz, to maintain optimal correction performance.

This semi-analytical approach allows FAST to model both uplink and downlink scenarios effectively, providing significant speed advantages over full MC-WO simulations while ensuring accurate characterisation of AO system performance under varying turbulence conditions. However, as FAST assumes small perturbations to the wavefront, it is limited to the weak turbulence regime.

3.4 Measuring atmospheric turbulence

3.4.1 Shack-Hartmann Image Motion Monitor (SHIMM)

This document uses a Shack-Hartmann Image Motion Monitor (SHIMM) to measure atmospheric optical turbulence parameters. The SHIMM is comprised of a telescope coupled with a SHWFS. A CMOS camera is used to image the focal plane of the SHWFS as the telescope tracks a bright star. By tracking a bright star, short exposure times can be used to capture the turbulent atmosphere at a faster rate than the turbulence can evolve. The detail of the original instrument is in Perera et al. (2023).

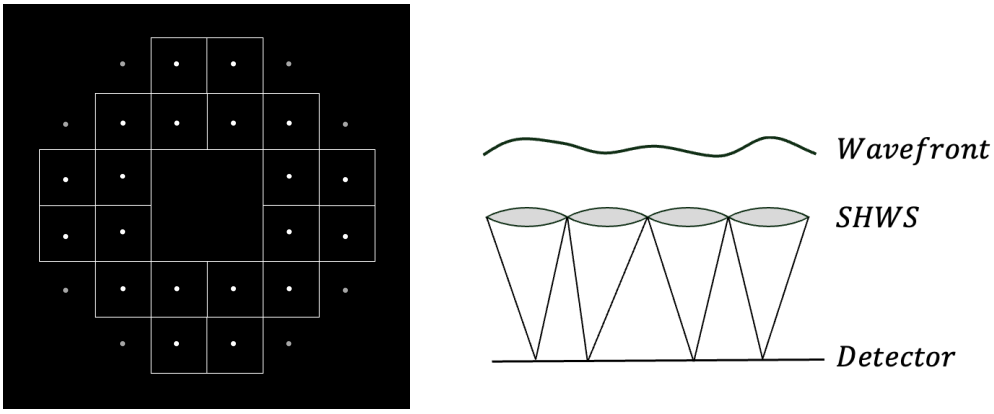

Figure 3.27: Illustration of the Shack-Hartmann Wavefront Sensor. (Left) Spot pattern formed on the detected from the illuminated sub-apertures. The spots in the white grid are fully illuminated and are used in the calculation of the turbulent parameters. (Right) Schematic showing the displacement of the spots from each lenslet due to the slope in the incoming wavefront.

Figure 3.27 shows the spot pattern formed on the detector when the SHWFS is illuminated. The telescope aperture and secondary mirror cause either no or partial illumination on other sub-apertures as a result these spots are not used to derive the turbulence measurements. The centre of the spot which is used in the image processing is referred to as the centroid which is found using the centre of mass. Each spot is displaced from the centre of the sub-aperture, where the displacement is equal to the gradient of the wavefront at the sub-aperture. The autocovariance between the x- and y-displacement of each of the centroids within the WFS is calculated to generate an auto-covariance map.

The auto-covariance is weighted with the scintillation strength for varying layers with the highest layers contributing the most turbulence and the ground layer contributing none. This allows for the extraction of an estimated 4-layer $C_n^2 dh$ profile which can be used to calculate r_0, σ_R^2, σ_I^2, θ_0, τ_0. The calculation of the centroids removes mean motion across the sub-apertures, only including differential motion. By doing so, this removes spot motion due to wind shake and vibrations.

The particular device used in the document, whose details can be found here Griffiths

et al. (2023), provide advancement to other atmospheric monitors due to its ability to operate continuously over the day and night by using an infrared camera to remove sky background below 900 nm. The specific details of each optical set-up vary between experiments and will be detailed in later chapters.

3.4.2 Site characterisation

Turbulence monitors are fundamental to the process of site characterisation where the suitability of a location for a potential Optical Ground Station (OGS) can be assessed. The turbulence characteristics of an area depend on various geographical and environmental factors that can be challenging to model accurately. Taking real measurements of these characteristics is crucial for designing an effective optical system and estimating its performance. Site characterisation is important not only in individual OGS design but also to optimise communication system uptime and manage costs associated with establishing a network of optical ground stations (Giggenbach et al., 2015; Osborn and Sarazin, 2018). It is also important to consider typical meteorological effects, such as cloud cover, as part of this analysis (Olmedo and Jiménez, 2023).

CHAPTER 4

Effects of changing zenith angles on optical propagation through turbulence

4.1 Introduction

Generally, turbulence strength decreases with altitude with the strongest turbulence typically occurring in the ground layer (Avila et al., 1997; Tokovinin, 2004; Butterley et al., 2020). As the angle from zenith increases, the length of the propagation path of light through the atmosphere increases. This elongation of the path means that the light passes through a larger volume of turbulent air, leading to greater interaction with turbulence. Consequently, the overall strength of turbulence increases with the zenith angle (Roddier, 1981).

The relationship between the zenith angle and atmospheric parameters is well-accepted in the field of atmospheric turbulence, particularly in the context of adaptive optics. While it historically holds its relevance in astronomy, this relationship has now gained significant importance in the design and performance estimation of ground-to-satellite optical links (Phillips et al., 2000; Chen et al., 2018a; Stotts and Andrews, 2022). This is particularly relevant for optical communications with LEO satellites, as well as for ground stations at high latitudes communicating with GEO satellites (Fischer et al.,

2018; Schieler et al., 2022; Chen et al., 2018b), which must operate at large zenith angles. Understanding the zenith dependency of optical light propagation through atmospheric turbulence also has relevance in satellite laser ranging, as well as solar observations (Vasylyev et al., 2019; Marino, 2012).

Optical turbulence measurements were taken in September 2022 at the Roque de Los Muchachos Observatory in La Palma, Canary Islands, Spain. The measured Fried parameter (r_0) and scintillation index (σ_I^2) are presented here, metrics of turbulence strength and intensity variance, respectively, measured concurrently with two identical instruments, one pointing near zenith and the other tracking a single star to slew through various zenith angles. By comparing measurements any changes observed can be attributed to the increasing zenith angles instead of changes in the local environment caused by variations in air temperature and wind speed.

The primary objective is to validate the leading theories of r_0 and σ_I^2 variance with zenith angle which are presented in section 3.2.1.1. The variation of r_0 with the secant of the zenith angle is one of the fundamental "laws" of adaptive optics, yet this has not been experimentally tested directly.

Some initial studies have been conducted, particularly in relation to scintillation. In Chivers and Davies (1962), increased intensity fluctuations with increasing zenith angle were observed, but the study presented only 11 data points. Young (1970a) notes that at large zenith angles, saturation in scintillation is observed, though again, the evidence is based on a limited number of data points. Parry et al. (1979) attempted to determine the zenith angle at which scintillation saturation occurs, however, no change is observed between the zenith range of 0° and 80 °, indicating a problem with the experiment or the analysis tools used. All these studies used a single instrument, whereas this work differentiates itself by using a secondary instrument to eliminate temporal uncertainties in the measurements. Additionally, none of these experiments measured the Fried parameter. This work serves as a demonstration to validate existing models, and the

experiment would need to be repeated for a comprehensive statistical understanding.

4.2 Experimental details

The primary aim of this experiment is to make comparisons between turbulence measurements taken at zenith and varying zenith angles. The experiment was conducted from the roof of the Isaac Newton Telescope at the Observatorio de Los Muchachos in La Palma. Measurements were taken using a Shack-Hartmann Image Motion Monitor (SHIMM), which uses a Shack-Hartmann wavefront sensor to measure the slopes of the wavefront at the telescope pupil plane. This set-up used a Cassegrain telescope with a 23.5 cm diameter aperture. The SHIMM uses a ZWO ASI462MC CMOS camera, which has a responsivity between 400 nm and 1000 nm, with a central wavelength of 695 nm. The camera's read noise ranges from 0.47 to 2.46 e^-, which is suitably low for observing bright targets but should be considered if scintillation reduces the received intensity within a subaperture to near zero. Integrated turbulence parameters like the Fried parameter can be derived from the wavefront sensor slopes. The temporal scintillation index was determined by observing the fluctuations in the brightness of a single Shack-Hartmann spot during the measurement. The background light is derived from measuring the mean intensity in an annulus around each sub-aperture spot and this is subtracted from each measurement. 3600 images of the Shack-Hartmann focal plane were taken at a rate of 120 Hz with a 2 ms exposure time for each measurement, with each measurement taking 30 seconds. The short exposure time is necessary to prevent smearing of the focal spots within the sub-apertures during the exposure (Wilson et al., 2009). The SHIMM compensates for vibrations by measuring the differential motion of spot patterns in the Shack-Hartmann focal plane. Further information on the instrument's validation can be found in Griffiths et al. (2023).

Two SHIMMs were used in the experiment positioned approximately 2 meters apart, seen in figure 4.1. The primary SHIMM, referred to as SHIMM1, measured the integ-

Figure 4.1: Two SHIMM set-up on the roof of the Isaac Newton Telescope, La Palma.

rated turbulence parameters for targets with an zenith angles smaller than 20 degrees. Within this range, equations 3.15 and 3.19 were confidently employed to perform air mass correction up to zenith. The secondary SHIMM, referred to as SHIMM2, tracked stars from various zenith angles between 0° and 90°. By comparing the measurements taken by SHIMM1 and SHIMM2, the validity of equations 3.26 and 3.18 at all zenith angles could be tested.

4.3 Results

Initially, both the r_0 and σ_I^2 measured using SHIMM1 and SHIMM2 are presented. Here, all SHIMM1 values are scaled to zenith, while SHIMM2 values are left unscaled. The scaled SHIMM1 data to SHIMM2's zenith angle is then presented, which uses the theory discussed in section 3.2.1.1. SHIMM1 observed target stars lay between 10° and 25° zenith angles, within this region there should be no deviation from the Kasten and Young theory, $M_{KY}(\zeta)$. All measurements have been scaled to a wavelength of 500 nm to standardise results.

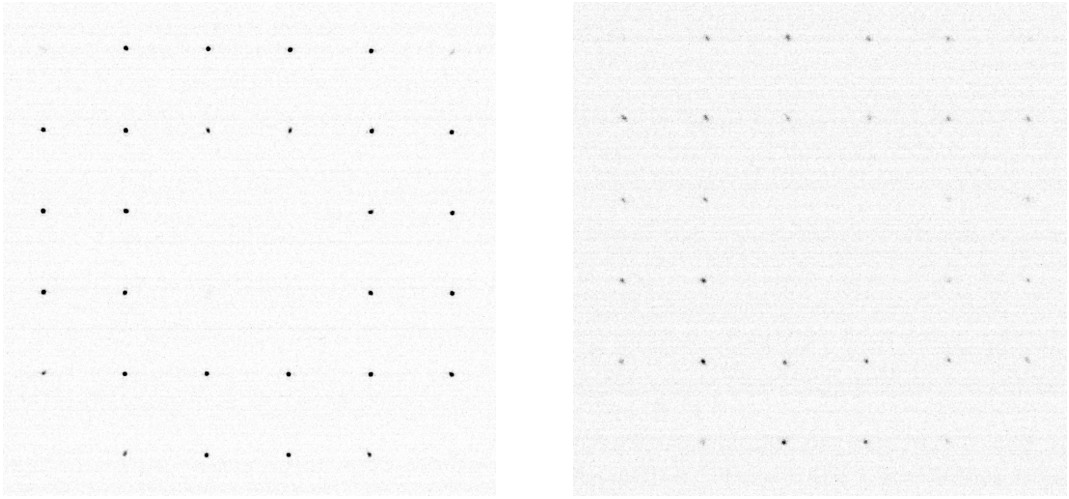

(a) 6° (b) 89°

Figure 4.2: Shack-Hartmann spot pattern for two measurements at zenith angles of 6° and 89°. The data was taken over a 2 ms exposure and these measurements were taken simultaneously at 03:09 AM. Both images have been plotted on the same greyscale range.

For clarity, the Fried parameter is scaled to zenith by:

$$r_0(\zeta) = r_0(0) M_{KY}(\zeta)^{-3/5}, \tag{4.1}$$

where $r_0(0)$ is the Fried parameter measured by SHIMM1 scaled to zenith and $r_0(\zeta)$ is scaled to the zenith angle of SHIMM2.

Additionally, σ_I^2 is be scaled to zenith by:

$$\sigma_I^2(\zeta) = \sigma_I^2(0) M_{KY}(\zeta)^{11/6}, \tag{4.2}$$

where $\sigma_I^2(0)$ is the scintillation index measured by SHIMM1 scaled to zenith and $\sigma_I^2(\zeta)$ is scaled to the zenith angle of SHIMM2. This is then inputted into equation 3.17 to derive the σ_I^2 in the strong perturbation regime.

Figure 4.2 shows the images taken by both SHIMMs concurrently at 3° and 85° zenith. With increasing zenith angle there is an increased spatial variance in the spot brightness across the Shack-Hartmann focal plane. There is also an overall mean reduction in the

received intensity across the aperture. More temporal variations in the spot brightness are observed as the zenith angle increases. All these effects are as expected.

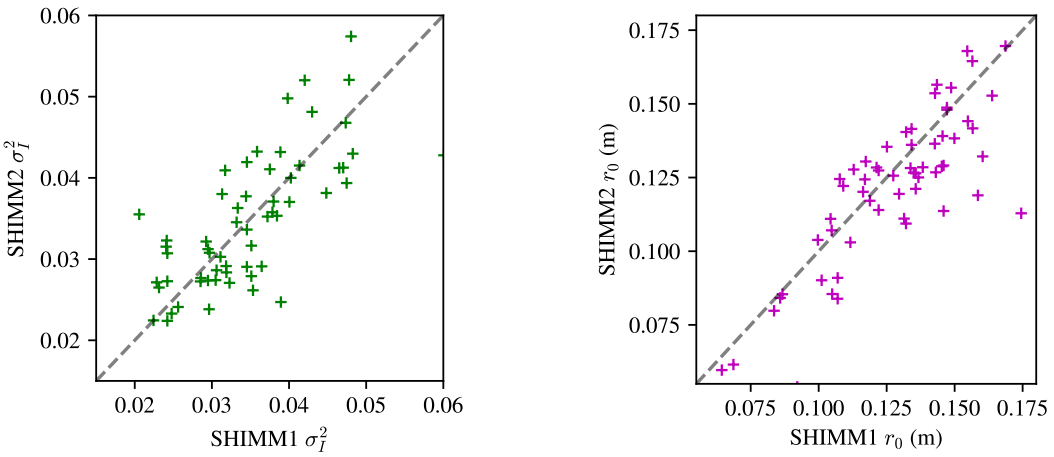

Figure 4.3: SHIMM1 and SHIMM2 measurements are plotted against each other when the instruments are pointing at the same target. (Right) Measured scintillation index. (Left) Measured Fried parameter.

For the first hour of the run, the two instruments were pointed at the same target to compare the measurements between the two systems. Figure 4.3 shows the comparisons between the measured turbulence parameters from two SHIMMs. The correlation between the two sets of data for scintillation and the Fried parameter is 0.78 and 0.75, respectively, indicating an agreement between the measurements from the two systems.

Below, a more in-depth analysis is presented of the correlation between the two SHIMM measurements. During the 10-day campaign, adverse weather conditions, including high winds and intermittent clouds, posed challenges to data collection on several nights, resulting in only 2 nights of usable data. In the following sections, the night with the most favourable observation conditions will be discussed first, followed by the second-best night. Figure 4.4 shows the cloud conditions before sunset.

Figure 4.4: View of the Isaac Newton Telescope showing various types of stratus and cumulus clouds spanning different altitude levels. Fog can be seen rising from the caldera from the right side of the image. Large zenith angle measurements cannot be taken in these conditions.

4.3.1 Analysis of nights with ideal weather conditions

The most complete set of data was taken on September 20th, 2022. Here SHIMM2 was able to track Vega from near zenith down to near 90 degrees zenith angle. The measured zenith angles as a function of time are shown in figure 4.5. The local weather data is presented in figure 4.6. This was the calmest night of observations where the wind speed only fluctuated between 0 and 4 ms^{-1}.

4.3.1.1 Scintillation index

Figure 4.7 shows the measured σ_I^2 by SHIMM1 and SHIMM2 throughout the night of the 21st. The local σ_I^2 mean, which is measured from zenith, is 0.03 which varied between 0.02 and 0.08. The σ_I^2 measured by SHIMM2 reaches saturation at 02:50 AM which occurs at 80° zenith which is similar to the zenith angle predicted by theory (Roddier, 1981).

Figure 4.8 shows the measured σ_I^2 of SHIMM2 compared with SHIMM1 which measures the optical turbulence at zenith and is scaled to SHIMM2's corresponding zenith angle

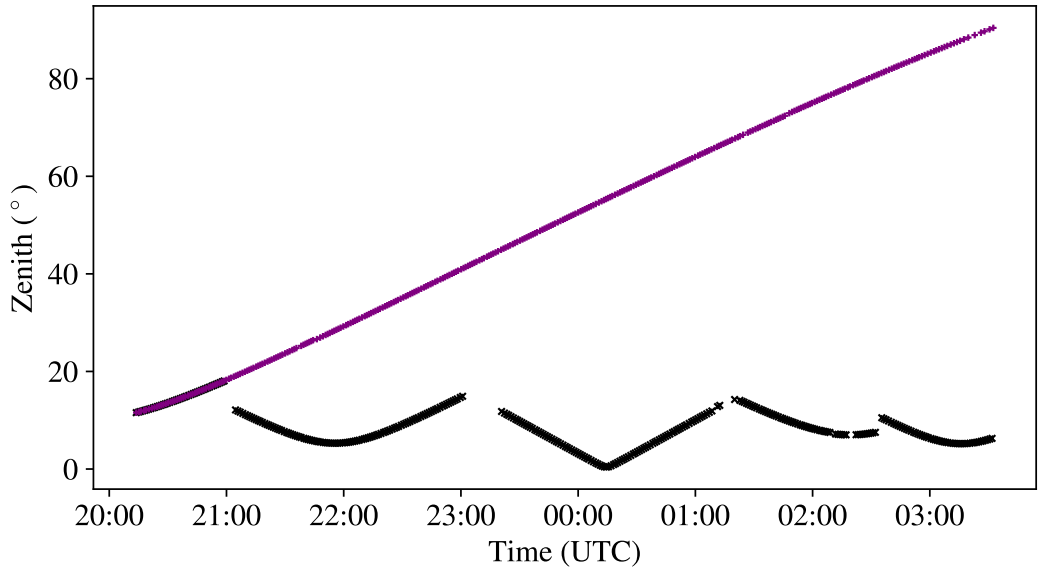

Figure 4.5: Measurements corresponding zenith angles by SHIMM1 (black) and SHIMM2 (purple). SHIMM1 pointed at targets between 0° and 20° zenith whilst SHIMM2 pointed at Vega which was tracked until it set.

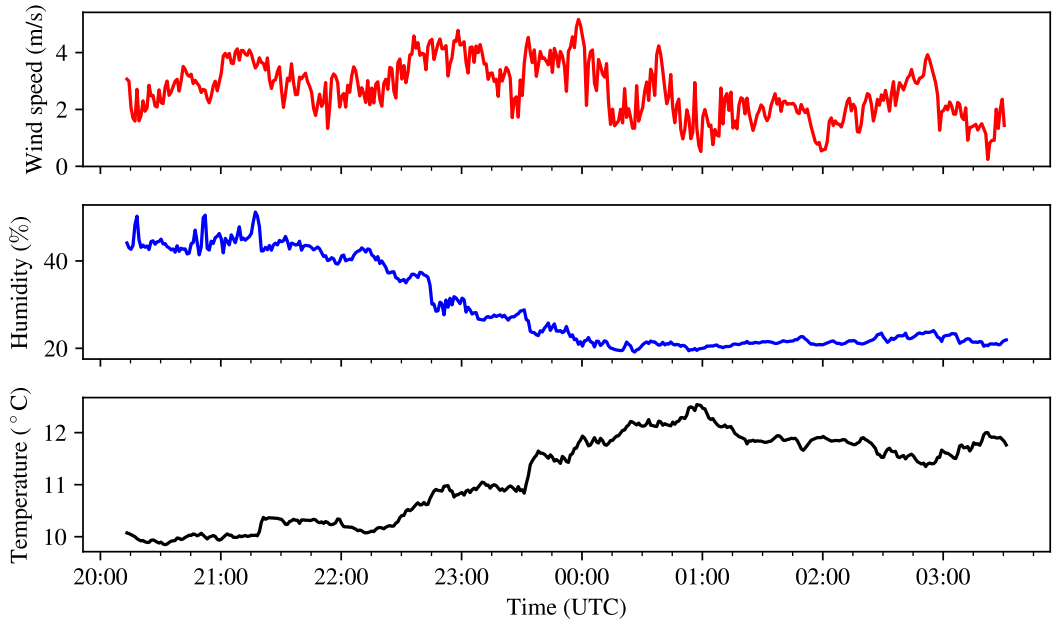

Figure 4.6: Local weather data from the night of the 21st of September 2022. The panels show wind speed, humidity, and temperature, from top to bottom. The weather station was situated around 5 m from the location of the experiments.

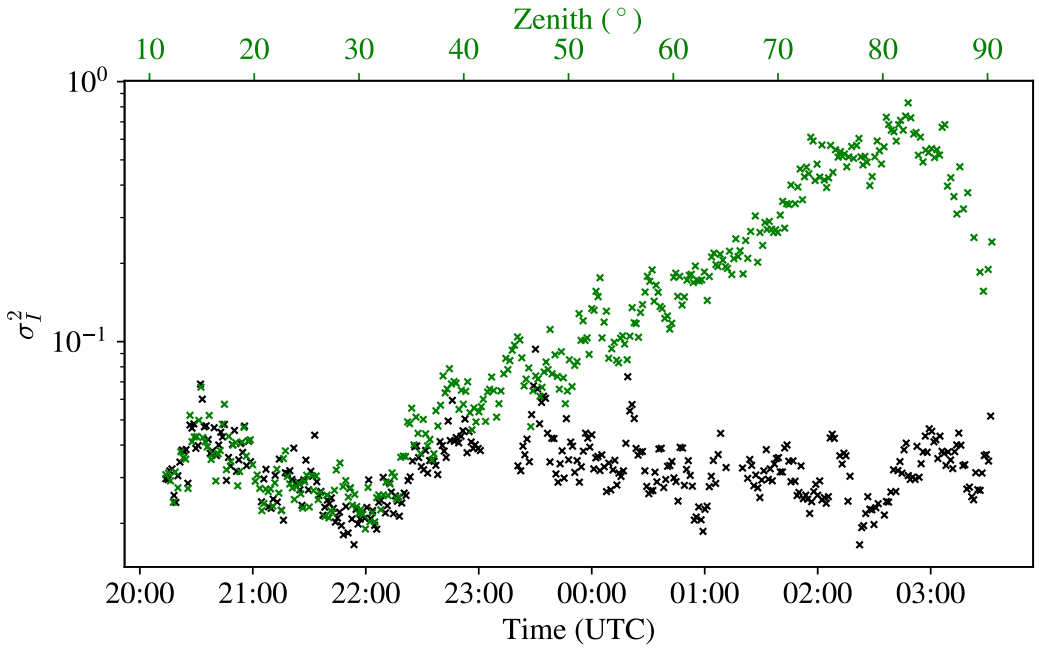

Figure 4.7: Measured σ_I^2 data from SHIMM1 (black) and SHIMM2 (green) as a function of time and zenith angle of SHIMM2. SHIMM1 stayed within 20° of zenith whereas SHIMM2 tracked Vega from 10° to the horizon at 90°. The secondary x-axis shows the zenith angle of SHIMM2. All data points represent the average of a minute of data. All data is scaled to 500 nm.

using equation 3.26. Here, it is seen that there is a very good agreement between both the weak and strong fluctuation model and the measured σ_I^2 up until ∼80°, before this the data has a correlation coefficient of 0.91. Beyond this zenith angle, the weak fluctuation asymptotically increases, and the strong fluctuation theory begins to saturate however this model estimates the measured σ_I^2 to be higher than the observed σ_I^2. A closer view of the point of deviation between all three datasets is shown in figure 4.9.

There are many reasons as to why there is a divergence between the model and measurements at very large zenith angles. One explanation for this difference is a decrease in signal due to high atmospheric attenuation when imaging through a large volume of turbulence, as seen in figure 4.2. The signal-to-noise is reduced so the intensity variance may not be detectable above the noise. Figure 4.10 shows the intensity of the centroid

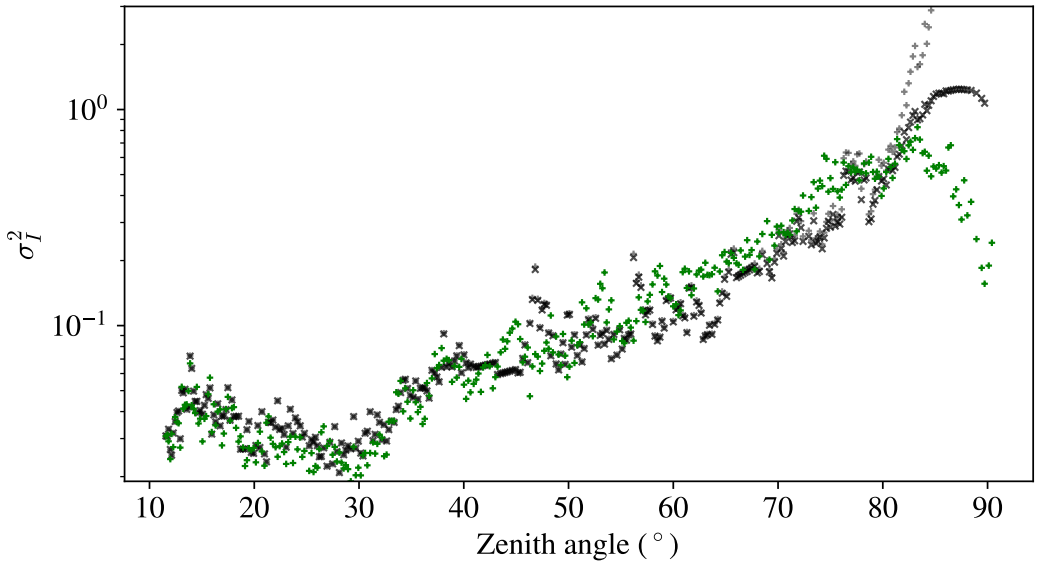

Figure 4.8: Comparisons between measured σ_I^2 and theoretically derived σ_I^2 across varying zenith angles. Green crosses represent direct measurements from SHIMM2, while grey and black crosses correspond to weak and strong fluctuations theories, respectively, using equations 3.15 and 3.26, both derived from SHIMM1 and subsequently scaled to the corresponding zenith angle of SHIMM2.

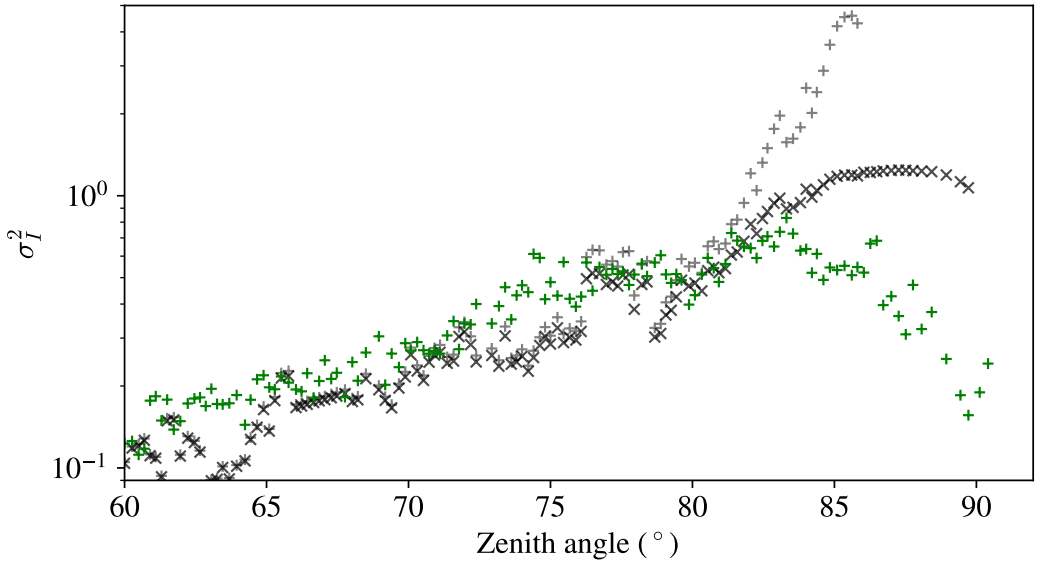

Figure 4.9: Zoom-in of Figure 4.8 at very large zenith angles.

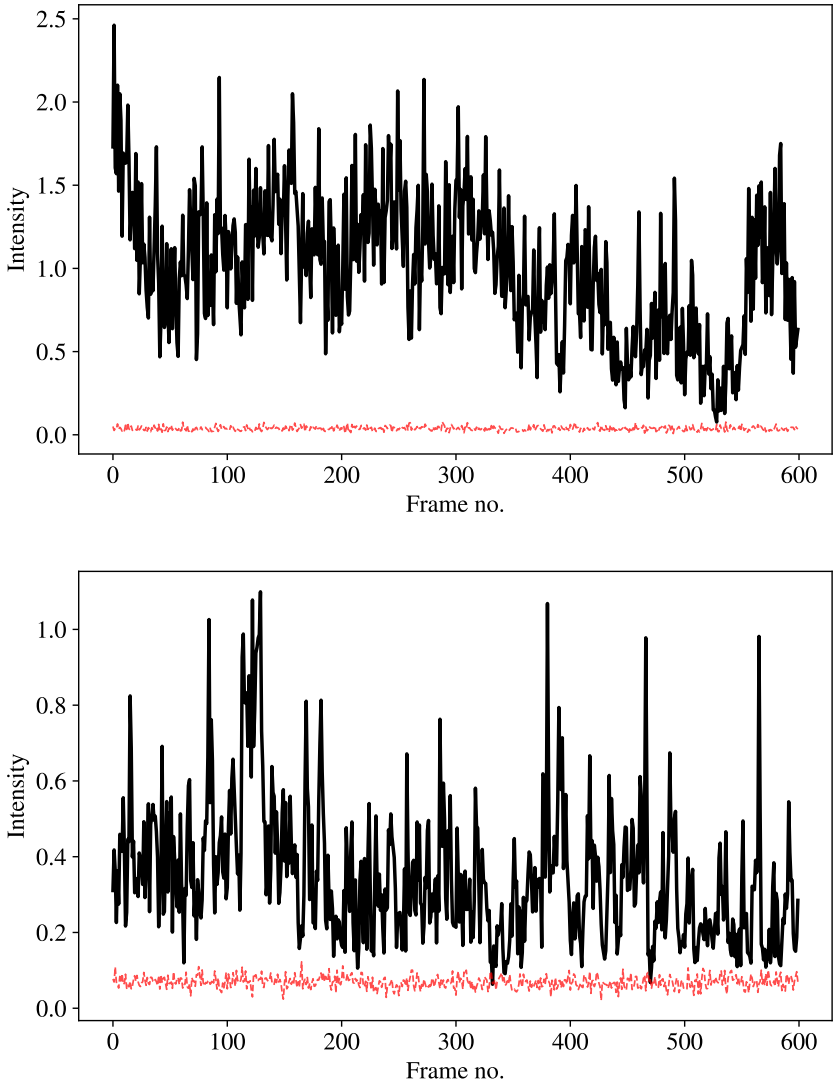

Figure 4.10: Comparisons between background noise intensity (red) and the measured intensity of a single spot (black). (top) Data taken at 5° and (bottom) data taken at 85°.

versus the background noise of the camera. The background noise is calculated by the averaged intensity in an annulus around the centroid. Here the intensity of the measurement is always greater than the background noise and should be detectable despite increased attenuation.

Additionally, the differences could also be due to the near-horizon optical path being through the oceanic atmosphere which is typically weaker. The evolving ground structure with increasing horizontal distance of the observer is a factor that equation 3.7 does not take into account. However, if the latter case were to be true, a divergence between theory and measurements would be anticipated much earlier, given that targets were already observed through oceanic turbulence as early as 45° zenith into the experiment.

There are several potential reasons for the divergence between the model and measurements at very large zenith angles. Since the model, as represented in equation 3.26, accounts for strong fluctuations, the reduction in scintillation is hypothesised to be attributed to alternative atmospheric effects, such as ray bending due to refraction or an increase in atmospheric attenuation, which are not incorporated into the models.

Unfortunately, it is difficult to disentangle instrumental effects from optical turbulence effects especially when observing at very large zenith angles. Despite this, this demonstration indicates that one can estimate σ_I^2 up to 80° from an instrument pointed near zenith in this particular environment.

4.3.1.2 Fried parameter

Figure 4.11 shows the r_0 measured by SHIMM1 and SHIMM2 over the 7-hour run. The SHIMM pointing toward zenith shows that throughout the night the Fried parameter reduces from 15 cm to 5 cm, indicating that the optical turbulence is getting stronger throughout the night. This reduction in r_0 may be attributed to an increase in local temperature and wind. Additionally, this trend is not observed in the measured scintil-

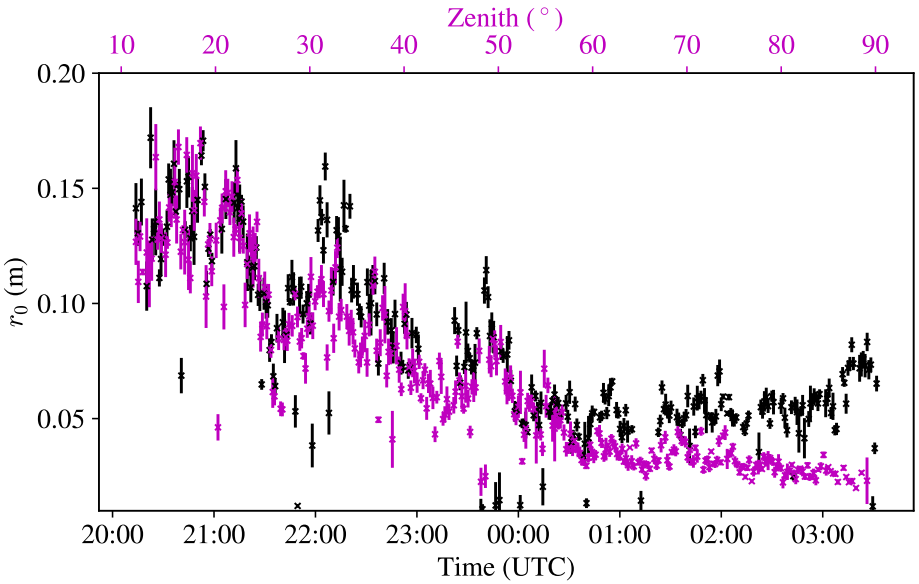

Figure 4.11: Measured r_0 data from SHIMM1 (black) and SHIMM2 (purple) as a function of time and zenith angle of SHIMM2. All data points represent the average of a minute of data taken over a 7-hour run. The secondary x-axis shows the zenith angle of SHIMM2. All data is scaled to 500 nm.

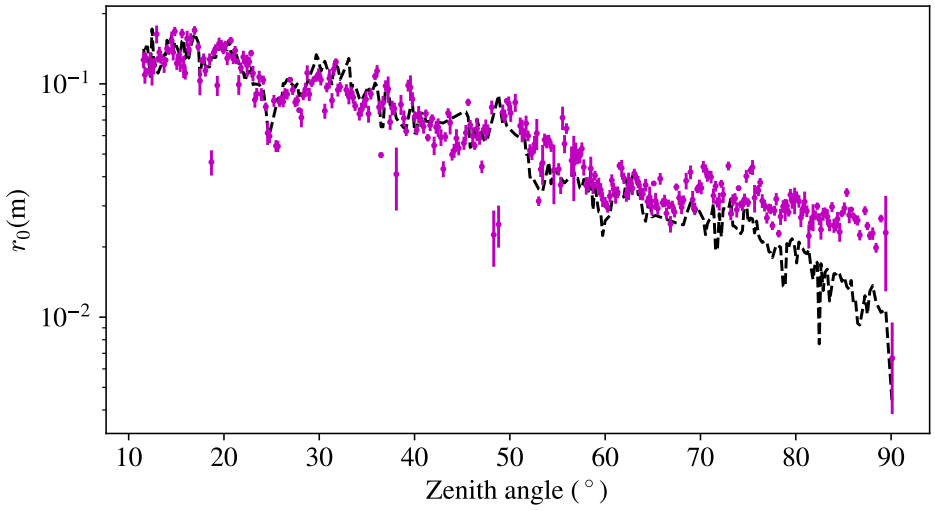

Figure 4.12: Comparison between the measured r_0 and r_0 derived from existing theory. (Purple) r_0 measured by SHIMM pointing at various angles. (Black) r_0 derived from measurements taken at zenith and then scaled using Kasten and Young theory Kasten (1965); Kasten and Young (1989). All data points are scaled to 500 nm and averaged over a minute of data.

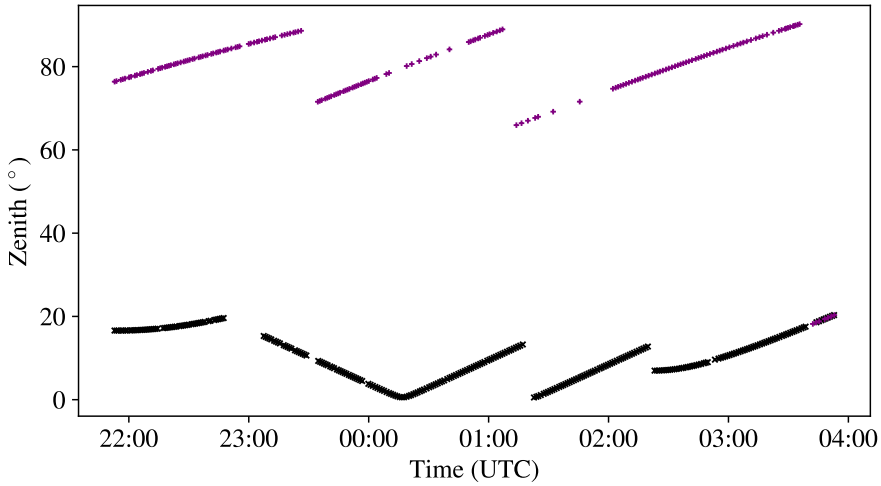

Figure 4.13: Zenith angles of the SHIMMs as a function of time for SHIMM1 (black) and SHIMM2 (purple).

lation, which decreases throughout the night; therefore, this change can be attributed to low-altitude turbulence.

Additional comparisons between the two measurements are presented in figure 4.12. Here data measured at varying zenith angles are compared with data collected at the zenith and then scaled to SHIMM2's corresponding zenith angle using the theory described in section 3.2.1.1. A strong agreement between measurement and theory is observed up until 70°, at which point the two datasets begin to diverge. For zenith angles beyond this threshold, both Kasten and Young theory and secant scaling underestimate r_0, suggesting the turbulence strength is weaker than the model predicts.

Our primary belief is that this mismatch arises from the omission of optical propagation effects in equation 3.11, as it is solely the integrated air mass along the propagation path. It has been observed in simulation that the optical propagation causes an increase in the measured r_0. It is believed that this is not an instrumental error due to a small r_0, as the SHIMM is capable of measuring r_0 values down to 1 cm, as seen in Griffiths et al. (2023).

4.3.2 Large zenith study

Another night of successful data collection occurred on September 19th, 2022. Despite encountering challenges like limited visibility and high humidity during this experiment, usable data were gathered. Tracking individual stars under these conditions proved to be particularly demanding, resulting in incomplete datasets. Due to unfavourable conditions, the study focused on tracking stars within zenith angles ranging from 60° to 90°, as potential deviations from the model were anticipated within this range. The sampled zenith angles are shown in figure 4.13. The same star was observed at 03:50 AM to verify that the instruments yielded the same optical measurements. Clouds lying near the horizon meant that high-zenith data could not be taken throughout the night with zero visibility between 01:00 AM and 02:00 AM.

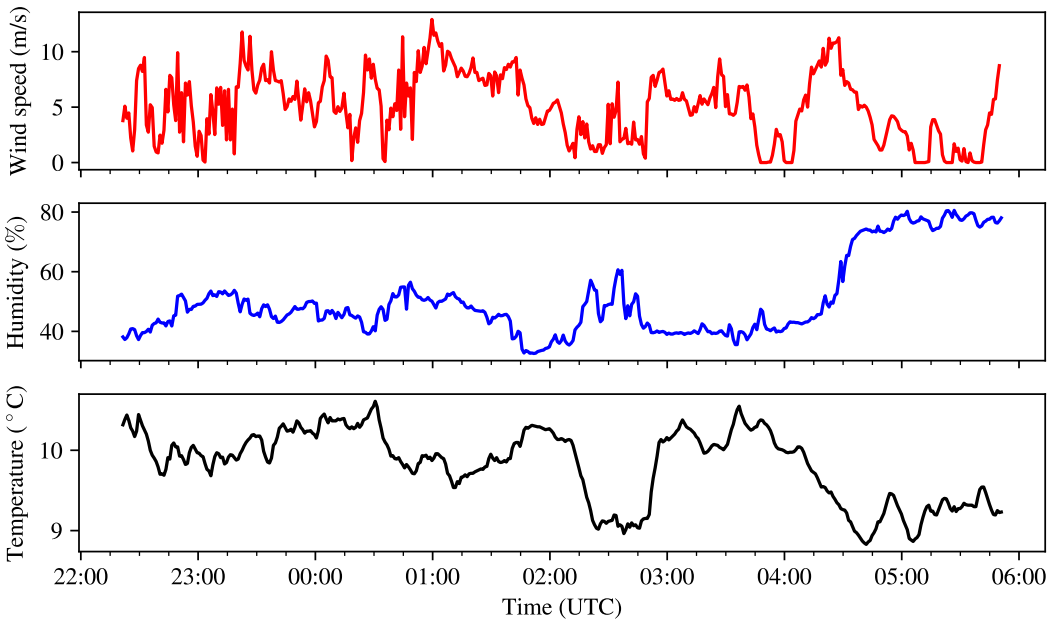

Figure 4.14: Local weather data from the night of the 19th of September 2022. Measurements were taken using the Isaac Newton Telescope weather station which sits approximately 5 m from where the experiment ran. The panels show wind speed, humidity, and temperature, from top to bottom

For comparison with data from other nights, the local weather data for this night

is presented in figure 4.14. The humidity levels towards the end of the night were sufficiently high and posed a risk of damage to the instruments. There were also stronger wind speeds.

4.3.2.1 Scintillation index

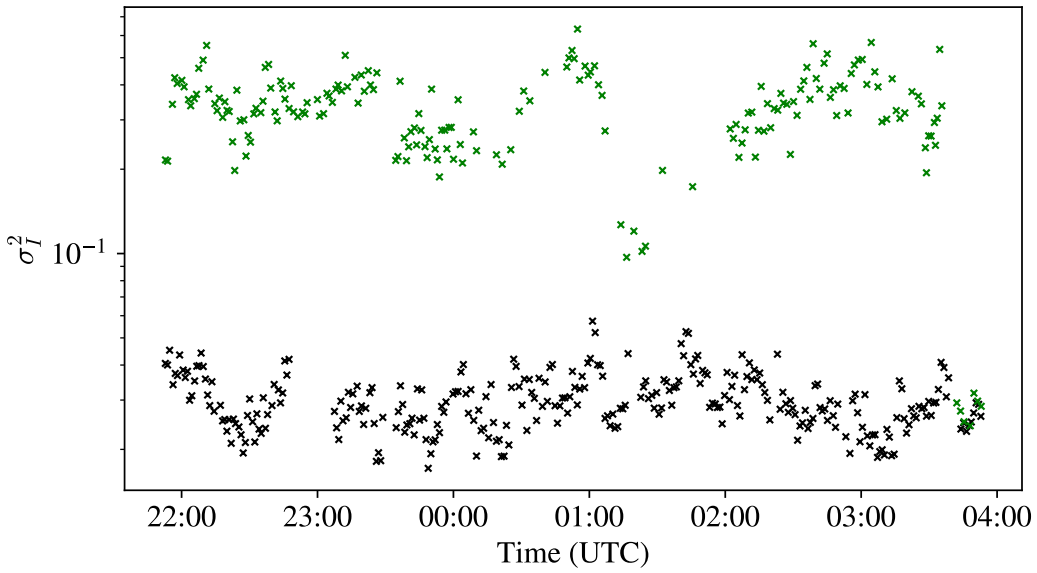

Figure 4.15: Measured σ_I^2 data from SHIMM1 and SHIMM2 as a function of time for the large zenith study on September 19th. Green crosses represent direct measurements from SHIMM2. Black crosses correspond to the measurements from SHIMM1 which was near zenith. All data points represent the average of a minute of data and are scaled to 500 nm.

The measured σ_I^2 values from SHIMM1 and SHIMM2 are shown in figure 4.15. There is a clear difference between the measured σ_I^2 with SHIMM1 compared to SHIMM2, with SHIMM2 measuring nearly ten times higher values than SHIMM1. Based on measurements taken between 22:00 and 23:00 and 02:00 and 03:00, the two data sets are unrelated. This is unsurprising, considering that the scintillation originates from turbulence occurring at considerable distances. At large zenith angles, the turbulent layers generating scintillation would be separated by several kilometres and uncorrelated.

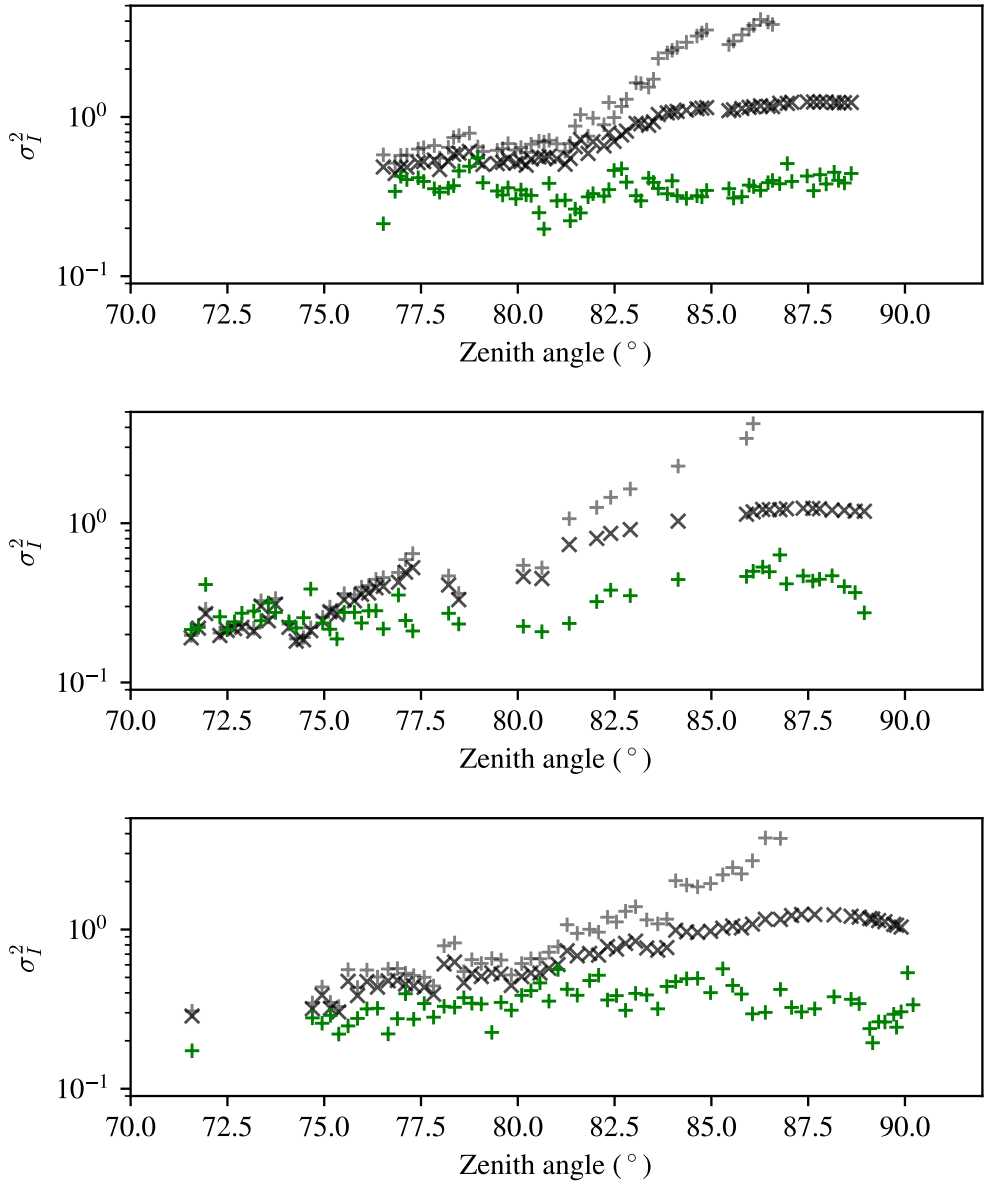

Figure 4.16: Comparisons between measured σ_I^2 and theoretically derived σ_I^2 across varying large zenith angles. Green crosses represent direct measurements from SHIMM2, while grey and black crosses correspond to weak and strong fluctuations theories, respectively. The data has been divided into three plots, each corresponding to individual large zenith runs. From top to bottom, these plots represent the first, second, and third runs, as depicted in Figure 4.13. All data points represent the average of a minute of data and are scaled to 500 nm.

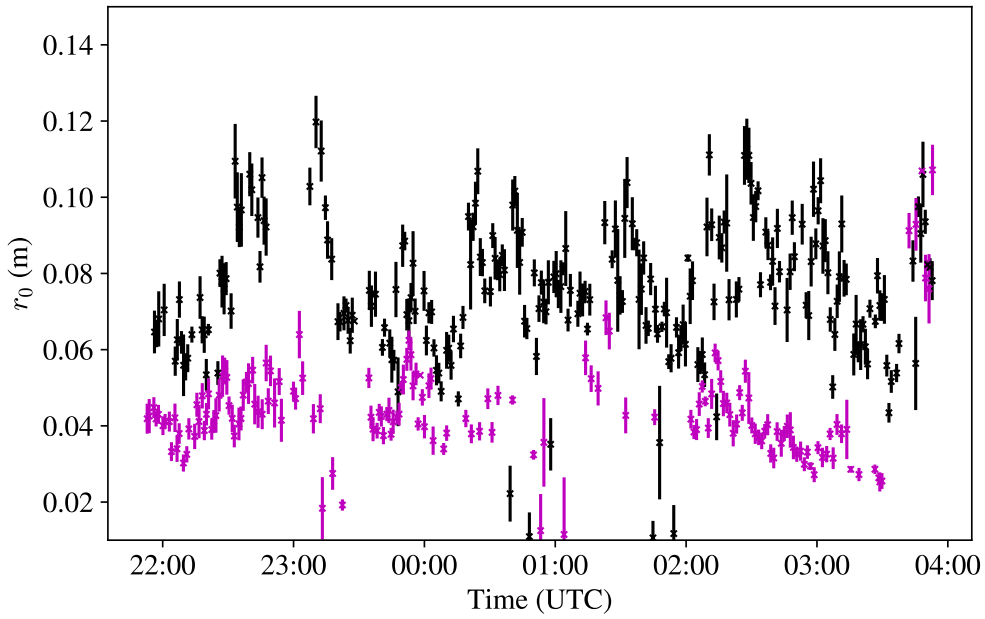

Figure 4.17: Measured r0 data from SHIMM1 (black) and SHIMM2 (purple) as a function of time and zenith angle of SHIMM2 for large zenith run. SHIMM1 stayed between 0° and 20° zenith whereas SHIMM2 stayed between 70° and 90° zenith. All data points represent the average of a minute of data taken over a 7-hour run. All data is scaled to 500 nm.

The scaled σ_I^2 data is presented in figure 4.16. The data has been subdivided to correspond to each large zenith run. This allows for the consideration of meteorological differences between each run. Each plot exhibits a trend similar to that observed in section 4.3.1.1, where both models deviate at a certain zenith angle. Specifically, the weak fluctuation model increases to very large values of σ_I^2 and the strong fluctuation model reaches a saturation point but still overestimates the strength of scintillation. This further validates the theory that equation 3.17 will not work well enough to estimate above a certain large zenith angle.

The point where the measured data deviates varies depending on the run, lying between 75° and 80°. It is believed that this is due to variance in weather conditions throughout the night. Strong wind conditions increase turbulent conditions, leading to stronger perturbations and reaching a saturation point sooner. This would also explain the dif-

ferences between the two nights. Despite this, it is still remarkable that both equations 3.15 and 3.17 work up to such large zenith angles. Further studies will be necessary to comprehend the nuances behind the observed disagreement at very large zenith angles.

4.3.2.2 Fried parameter

Figure 4.17 shows the measured r_0 values from SHIMM1 and SHIMM2 as a function of time. Again, these results show that looking at large zenith angles gives consistently smaller r_0 values. It can be seen that the development of r_0 occurs more rapidly than compared to σ_I^2, an effect which is also seen in section 4.3.1. The average r_0 measurement for this evening was 8 cm, 2 cm smaller than the previous run and when looking at large zenith angles got as small as 3 cm.

The scaled value of r_0 is shown in figure 4.18, again it has been split up into three sets of data, each corresponding to a particular large zenith run. Data points with very large error bars have been removed, this can occur when the wind causes the spot pattern to shift off the camera or when the turbulence is no longer following Kolmogorov statistics. In each run, the Kasten and Young theory overestimates the strength of r_0, a similar trend that is also observed in 4.3.1.2. As seen in the previous study the point of divergence between the theory and the measurements occurs at around 70°, smaller than that of scintillation. Because of this, this range of zenith values may not be appropriate for studying the Fried parameter dependence of large zenith. The instability of r_0 throughout the night makes it difficult to draw any further conclusions beyond this.

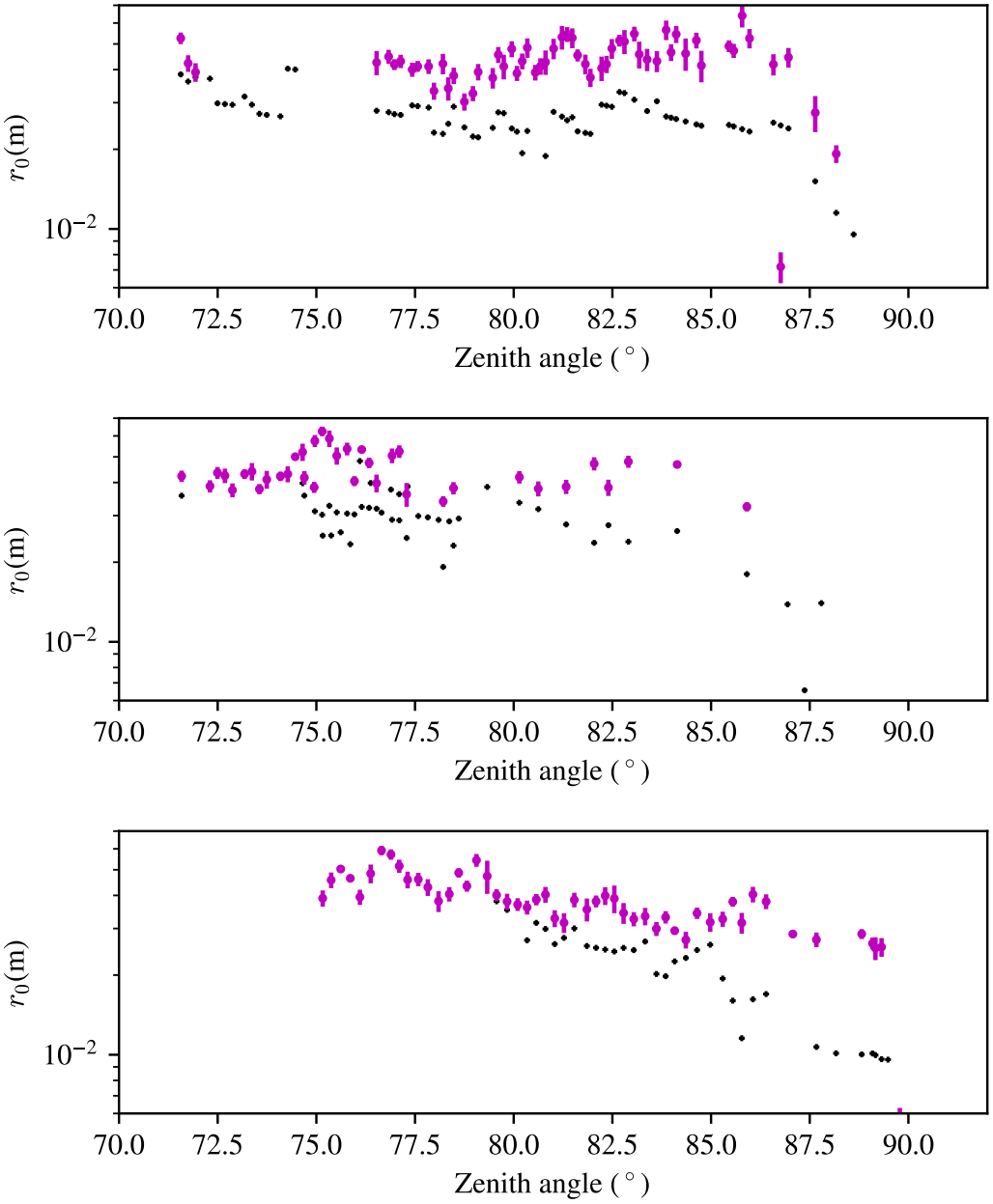

Figure 4.18: Comparison between the measured r_0 and r_0 derived from existing theory for large zenith run. (Black) SHIMM1 scaled r_0 from zenith and (purple) SHIMM2 represent the raw measurements. The data has been divided into three plots, each corresponding to individual high zenith runs. From top to bottom, these plots represent the first, second, and third runs, as depicted in Figure 4.13. All data points are scaled to 500 nm and averaged over a minute of data.

4.4 Conclusion

The main goal of this experiment was to compare turbulence measurements obtained at zenith with those measured at varying zenith angles to check the limitations of equations 3.26 and 3.19. The experiment ran on the 21st of September, 2022 on the roof of the Isaac Newton Telescope at the Roque de Los Muchachos Observatory in La Palma, Canary Islands, Spain. This study made comparisons between the turbulence parameters at zenith and at varying zenith angles by using two identical SHIMMs which ran concurrently in close proximity. This served to mitigate potential ambiguities in our measurements that could arise from local fluctuations in the turbulence conditions.

The results indicate that the measured scintillation index (σ_I^2) and Fried parameter (r_0) only began to diverge from their respective models at large zenith angles. For σ_I^2, a strong alignment is observed with both weak and strong fluctuation theories (equations 3.15 and 3.26) until zenith angles surpass $\sim$85°. Beyond this point, weak fluctuations increase asymptotically, and strong fluctuations saturate, both estimating a higher σ_I^2 compared to the observed values. The primary reason for the discrepancy is believed to be that equation 3.26 does not explicitly incorporate certain atmospheric effects. These effects include refraction-induced ray bending, increased atmospheric attenuation, and the influence of uncorrelated turbulence occurring at a distance. However, this study successfully demonstrates that one can estimate σ_I^2 to large zenith angles, for this particular environment, by using a measurement taken near zenith. Further studies are required to understand the nuances causing discrepancies at very large zenith angles.

Similarly, r_0 aligns well with the theory up to a zenith angle of $\sim$70°. At larger zenith angles, both Kasten and Young theory and secant scaling overestimates r_0 indicating weaker turbulence than these models predict. This discrepancy is attributed to the omission of optical propagation effects in equation 3.19.

An additional study was conducted on a separate night, specifically targeting measure-

ments for large zenith angles. SHIMM2's zenith angle remained fixed at 70° and 90° for this study. Similar trends were observed, validating the conclusions of the aforementioned study. However, adverse weather conditions, such as strong winds and high humidity levels, resulted in lower data quality. As a result, no further conclusions could be drawn from these observations.

Disentangling instrumental effects from optical turbulence remains challenging, especially during observations at very large zenith angles. Despite these challenges, it is believed that for this particular turbulent environment, equations 3.26 and 3.19 can be confidently used to calculate the atmospheric turbulence parameters within these limits. Consequently, a SHIMM can be employed in any astronomical site as a monitor and the measured turbulence parameters can be extrapolated to a zenith angle as low as $\sim$70°.

CHAPTER 5

Measuring optical turbulence above the City of London

5.1 Introduction

The full realisation of FSOC and QKD would involve connections between users on a global scale. This relies on stable bidirectional satellite-to-ground optical links in a variety of different locations including urban areas. Current atmospheric measurements are primarily focused on remote locations for astronomical applications or to study horizontal links in cities. Consequently, there has been a lack of research on the vertical atmospheric pathway of turbulence in built-up areas (Schöck et al., 2009; Jiang et al., 2008).

To the best of current knowledge, the only study of vertical optical turbulence in an urban environment was performed in Kallistratova and Pekour (1994). This work highlighted significant optical turbulence values when compared to a rural environment, particularly at night, attributable to the urban heat island effect. An effect that occurs in cities, which, being primarily composed of concrete and asphalt, absorb and retain more heat than rural areas. The author notes that data from a rural environment cannot be applied to urban conditions. However, the measurements were limited to the boundary layer, restricting the understanding of high-altitude turbulent effects.

Additionally, the author highlights that the method used to derive the C_n^2 values fundamentally relies on the assumption that temperature fluctuations are the sole driver of refractive index fluctuations. This notably overlooks the potential impact of pressure fluctuations, which could also play a critical role.

A portable SHIMM (Griffiths et al., 2023) is used to measure the full vertical distribution of atmospheric optical turbulence in the City of London. The measured Fried parameter, Rytov variance and scintillation index are presented, representing the first vertical atmospheric optical turbulence measurement in an urban environment. These findings offer insights that can aid in the design and development of optical ground stations in urban environments.

This work demonstrates a technique for configuring the modified Hufnagel-Valley model of turbulence to match the measured turbulence statistics. A 10-layer integrated C_n^2 profile is derived to match the Fried parameter and scintillation index measured over the night. Using these profiles, an optical link is simulated where optical propagation and adaptive optics (AO) modelling are executed using the Fourier domain Adaptive optics Simulation Tool (FAST) (Farley et al., 2022). The focus is on downlink communications from a low-Earth orbit (LEO) satellite, a link with numerous communication applications such as remote sensing and Earth observation where it is necessary to transmit a significant volume of data collected by satellites to a ground station. There is also an increasing prevalence of LEO satellite constellations such as Starlink and Telesat (Zhu et al., 2022; Liao et al., 2017). The predicted temporal changes in the performance of a particular simulated system between a LEO satellite and ground are presented, assuming the satellite is at zenith to represent the best-case conditions. Then the change in optical communication performance is investigated as the propagation path and integrated turbulence strength increase with increasing zenith angle during a LEO transit. For all systems, the improvement in optical coupling with the use of various AO configurations is demonstrated.

This chapter serves as a demonstration of optical turbulence measurements in an urban environment. With the advent of the SHIMM, the assimilation of data in these settings has started. While the dataset presented here is modest, it represents a start toward comprehensive knowledge in this field. This study also contributes to our understanding of the logistical operation of the SHIMM as a portable tool for measuring optical turbulence. Moving forward, additional data collection efforts will be necessary to further reach statistical conclusions on the environments.

5.2 City-based atmospheric optical turbulence measurements

5.2.1 Experiment description and set-up

The experiment ran over a 4-hour period on the night of the 20th of April, 2022, on the 5th floor (approx. 15 m above ground) of a building on Threadneedle Street as shown in figure 5.1. The building stands directly opposite the Bank of England and is less than a kilometre from the London Stock Exchange. The surrounding area is comprised mostly of high-rise buildings and roads. The instrument was placed on wooden slats and stood 1.5 m above the surface. The local air temperature fluctuated between 5°C and 7°C throughout the night, with an average wind speed of 4.4 ms^{-1}. These are standard conditions for this time of year. The night was relatively clear with some high cirrus.

The SHIMM measures the angle-of-arrival and intensity in a Shack-Hartmann wavefront sensor. The instrument has been extensively tested and validated and additional information on the SHIMM can be found in Griffiths et al. (2023). This set-up used a Cassegrain telescope with a 28 cm diameter aperture. Stars with magnitude 2 or brighter were observed at 650 nm wavelength, selecting bright targets to achieve a high signal-to-noise ratio despite the high cirrus and background light. The techniques used

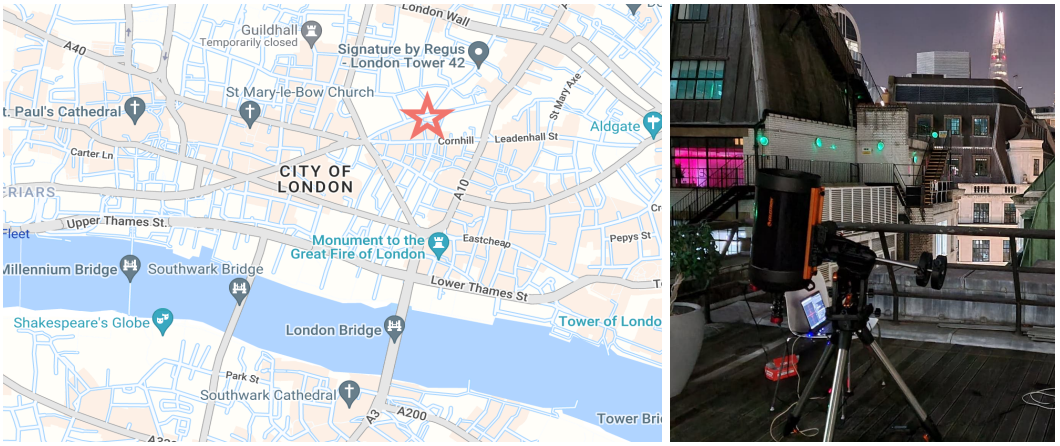

Figure 5.1: Experimental set-up. (Left) Experiment location is indicated with a star. Map data: Google, ©2022. (Right) SHIMM set-up on the roof of an office building on Threadneedle Street.

to measure the Fried parameter, r_0 and Rytov variance are also found in Griffiths et al. (2023).

The temporal scintillation index, σ_I^2, is measured over a 4.6 cm subaperture. σ_I^2 is a measurement of the intensity fluctuations in the receiver plane, given by equation 3.26.

5.2.2 Experimental results

Figure 5.2 presents the Fried parameter, Rytov variance and scintillation index that was recorded over the course of a 4-hour period, averaged over 30-second intervals. The Rytov variance was calculated using the 4 measured C_n^2 layers and calculated using equation 3.10. The gaps in the data at 03:30 AM and 04:00 AM were due to tracking issues when changing targets.

Figure 5.2 shows that r_0 remains relatively stable throughout the night, with a mean value of 4.5 cm and fluctuating by a standard deviation of 0.6 cm. This is relatively weak considering this is not an astronomical site where average r_0 values lie within the range 7 - 12 cm (Hardy, 1998). As measurements were taken 2.5 hours after astronomical twilight there were no solar heating effects (Wesely and Alcaraz, 1973). The fluctuation

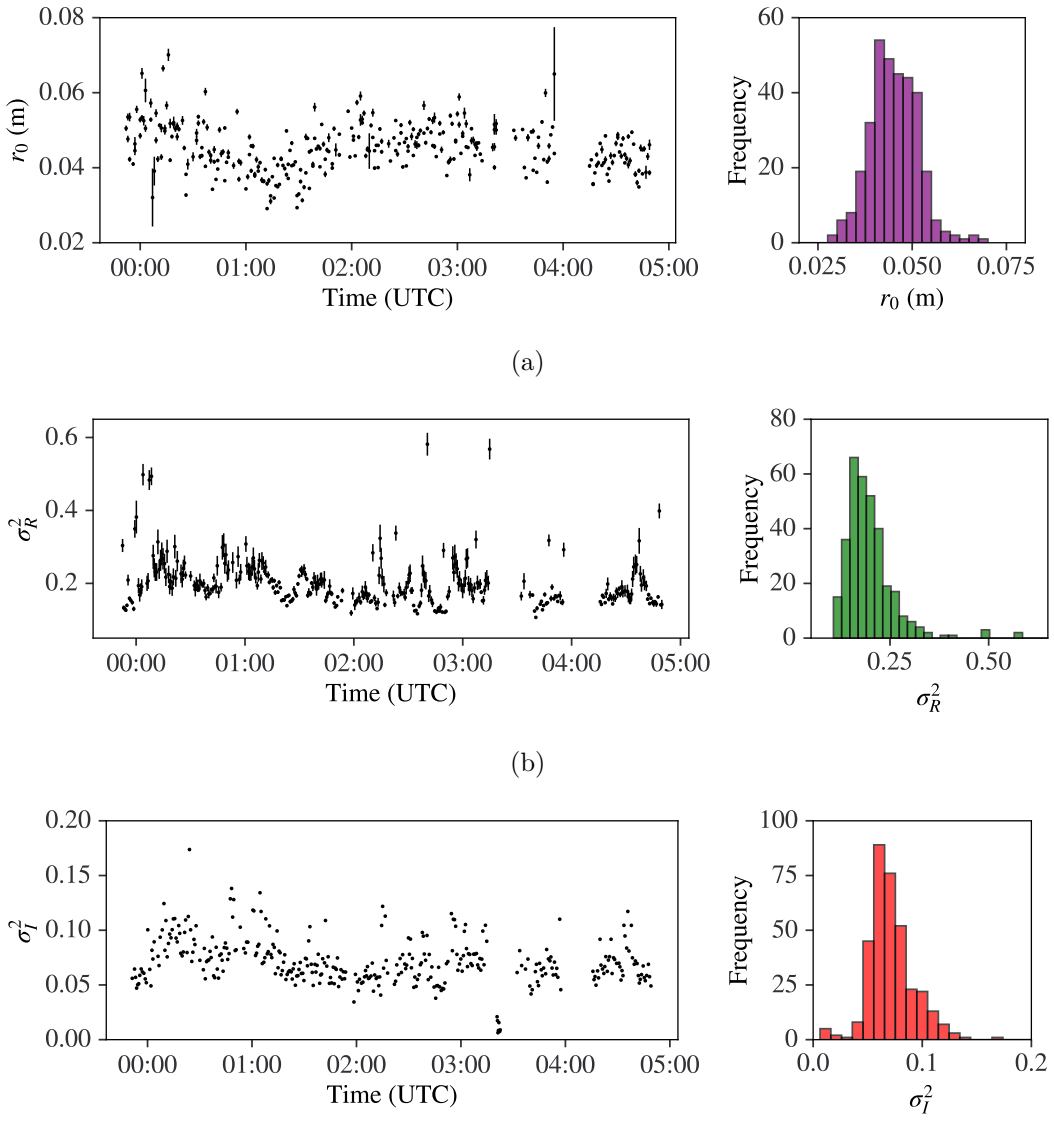

Figure 5.2: Measured atmospheric turbulence data from the city of London on the 20th of April from 0:00 AM to 5:00 AM (UTC). Presented as time-series (left) and histogram (right). (a) Measured r_0. r_0 has been scaled to 500 nm. (b) Measured Rytov variance, σ_R^2. (c) Measured scintillation index over a 4.6 cm subaperture. Measurements are averaged over 30-second periods. In all cases, turbulence parameters have been scaled to zenith.

in r_0 can be attributed to local variations in weather conditions such as wind speed and humidity (Trinquet and Vernin, 2006).

Figure 5.2 also shows the measured Rytov variance, σ_R^2, as a function of time, fluctuates over a smaller time scale compared to the r_0. The measured mean value of σ_R^2 is 0.20 with a standard deviation of 0.08. This is in the weak intensity fluctuation regime which is defined by σ_R^2<0.3 (Andrews and Phillips, 2005). Additionally, there is a weak correlation between r_0 and σ_I^2 (with a correlation coefficient of -0.11). This suggests a strong surface layer which dominates the variations in r_0 and is independent of high-altitude turbulence which predominately leads to scintillation.

Due to aperture averaging, σ_I^2 in a 4.6 cm subaperture of the SHIMM is not relevant information on its own. However, σ_I^2 is presented as it is a direct measurement of the intensity fluctuations and does not rely on SHIMM analysis. These values are used to replicate the observed turbulence conditions in simulation (see in section 5.3.1).

5.3 Turbulence measurements to simulation

A technique was developed to replicate the atmospheric turbulent conditions in simulation from the SHIMM data. The technique tunes the well-known Hufnagel-Valley (HV) model to match the observed conditions. This can be used in instances where only integrated turbulence parameters are available. These turbulent conditions are used as a downlink channel in the computational simulation of a propagating laser beam. This hybrid approach allows for the flexible design of link optics with realistic atmospheric conditions. This method can also be used to model ground-to-satellite links and links to GEO satellites.

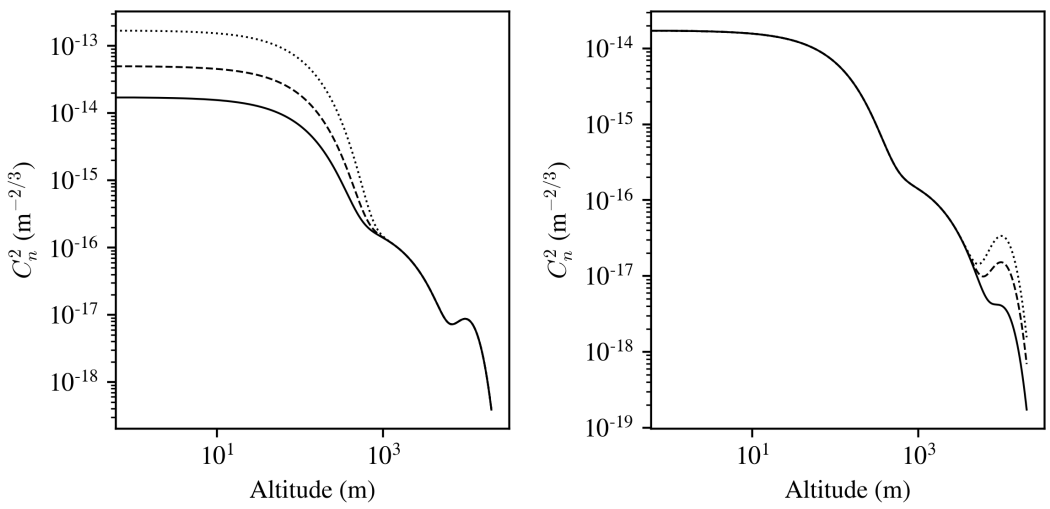

Figure 5.3: Modified HV distribution with variance in structure parameter (left), A, and w-parameter (right). (Left) Results for A values of 1.7×10^{-14} m$^{-2/3}$ (solid), 5×10^{-14} m$^{-2/3}$ (dashed) and 1.7×10^{-13} m$^{-2/3}$ (dots), corresponding to weak, moderate and strong ground turbulence, respectively (Andrews and Phillips, 2005). (Right) Results for w values of 10 ms^{-1} (dashed), 21 ms^{-1} (dashed) and 30 ms^{-1} (dots), corresponding to weak, moderate and strong pseudowind speeds, respectively.

5.3.1 Configuration of the modified Hufnagel-Valley model

Our approach here is to vary the HV-models two input parameters from equation 3.4, A and w, to replicate the observed turbulence conditions in simulation. Figure 5.3 shows that the input parameter A causes changes in the atmospheric distribution of C_n^2 up to 1 km in altitude and how varying the w-parameter contributes to the changes in the turbulence over 5 km in altitude. Both analytical models and simulations indicate that the w-parameter gives a specific scintillation value in a 4.6 cm subaperture regardless of the structure constant, A. These two parameters can be tuned to match the integrated r_0 and σ_I^2 from the SHIMM measurements.

An analytical aperture-averaged scintillation model is used to derive the value of w to match the σ_I^2 measured on the night (Andrews and Phillips, 2005). As the Shack-Hartmann subapertures are square lenses, this must be converted into a circular aperture of the same area to use this theory. A is chosen to match the observed r_0. By

deriving A and w this way a realistic turbulence distribution can be built to simulate each data set. A modified Equivalent Layers Method, as described in 3.2.2.1, is then used, integrating the C_n^2 between altitudes to obtain a single value that is equal to that section of turbulence with the same integrated parameters (Fusco et al., 1999). This allows for the generation of a profile with a small number of layers suitable for Monte Carlo simulations.

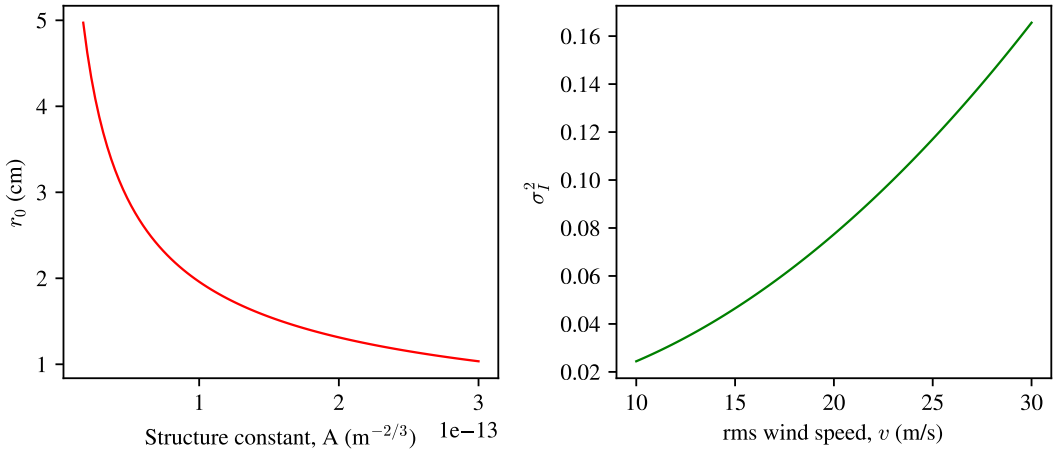

Figure 5.4: The output r_0 and σ_I^2 from the analytical models using the varying input parameters from the HV-model. (left) r_0 is derived by converting from C_n^2 at 500 nm. (right) σ_I^2 derived from the analytical aperture-averaged scintillation model over a 4.6 cm diameter aperture. Here the rms wind speed, v, is equivalent to the w-parameter.

Figure 5.4 shows the dependence of r_0 and σ_I^2 on input parameters A and w. The results presented here are derived from the aforementioned analytical models. It can be seen that to replicate the measured turbulence conditions, corresponding values of A and w can be chosen. As this theory does not account for strong turbulence, it is not applicable when σ_R^2 exceeds 1. However, the observed σ_R^2 remains below this threshold.

Figure 5.5 shows examples of deriving integrated turbulent layers using this method. The profiles used to model the best- and worst-case observed atmospheric conditions are presented. These profiles are used to model the atmospheric distribution of turbulence in simulation allowing for flexible analysis of FSOC system parameters.

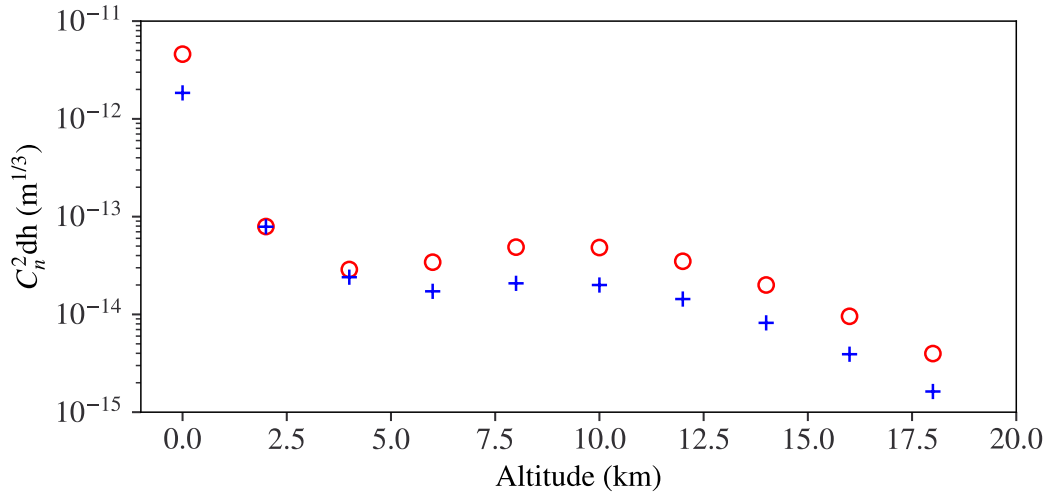

Figure 5.5: Derived vertical integrated turbulence profiles formed using a 10-layer model. For the best-case (blue cross) and worst-case (red circle) turbulence strengths observed on the night. These are derived using the concurrent weakest/strongest measured turbulence parameters taken at 02:50 AM and 01:32 AM, respectively.

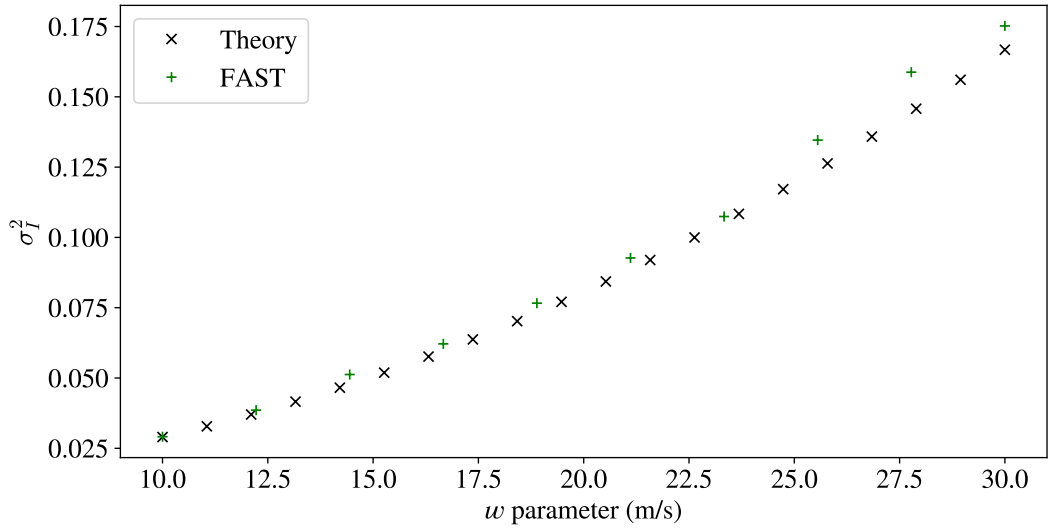

Figure 5.6: Comparison of scintillation over a 4.6 cm subaperture for varying w-parameter in the HV-model. Values are derived using the analytical model from equation 3.26 and FAST simulations.

Parameter	Value
Wavelength (nm)	1550
Receiver diameter (cm)	40
Receiver central obscuration (cm)	8
Transmitter diameter	Point-like
Zenith angle (°)	$0 \leq \zeta \leq 60$
Satellite altitude (km)	1000
Number of atmospheric layers	10

Table 5.1: Simulated atmospheric and receiver parameters.

5.3.2 Simulation of optical propagation and adaptive optics

The atmospheric optical propagation and adaptive optics system are simulated using FAST, a tool demonstrated in section 3.3.1. Each realisation is iterated 5000 times per simulation run to approach statistical convergence.

Figure 5.6 compares σ_I^2 between the analytical model and simulation results from FAST. This comparison validates FAST's results and demonstrates the effectiveness of tuning the w-parameter in the HV-model to simulate specific σ_I^2 values. Noticeably, for higher w-parameters, the datasets begin to diverge. This deviation may stem from stronger high-altitude turbulence, where the analytical theory starts to lose accuracy.

Parameter	Value
WFS type	Shack-Hartmann
WFS pitch (cm)	5
WFS noise	0
DM pitch (cm)	5
Loop rate (kHz)	1

Table 5.2: Simulated AO parameters.

The coupled flux, ρ, into a single-mode fibre in dB, scaled to the unaberrated case ρ_{dl}, is presented. For more information, see Farley et al. (2022).

The parameters used in our communication system configuration are shown in table 5.1. These parameters have been chosen to reflect existing communication systems (Perlot et al., 2007; Montmerle-Bonnefois et al., 2019; Osborn et al., 2021). First, it is assumed

that the communication downlink between a satellite and ground is at small zenith angles. This is done to investigate how link performance evolves as optical turbulence conditions change. Secondly, the effect on the coupled power of a downlink is examined as the air mass increases with changes in satellite elevation during LEO transit, using a specific set of atmospheric profiles considered representative of the entire night. It should be noted that the purpose of this chapter is to present modelling capabilities and exact system parameters are non-essential.

This work explores both tip/tilt-only and full wavefront correction. The specifications of the AO used in this work are shown in table 5.2; a justification for these parameters is provided in section 3.3.1. Note that due to the lack of wind profiles, an AO loop rate was assumed such that the temporal error remains small.

5.4 Free-space optical communications performance in an urban environment

The predicted performance of a downlink communication from a LEO satellite for each 30 seconds of turbulent data collected on the 20th of April is initially presented. Firstly, the satellite is placed at zenith in order to replicate the best-case for the coupling efficiency. Secondly, distributions have been built for predicted performance of a LEO pass by varying zenith angle between 60° through zenith and back down to 60°. The latter investigates the effect of increasing air mass on downlink performance. In both cases, the effects of applying various AO configurations to the receiver to correct phase are explored. All performance diagrams are presented as 2D-distributions built from histograms from the output of each simulated atmospheric state.

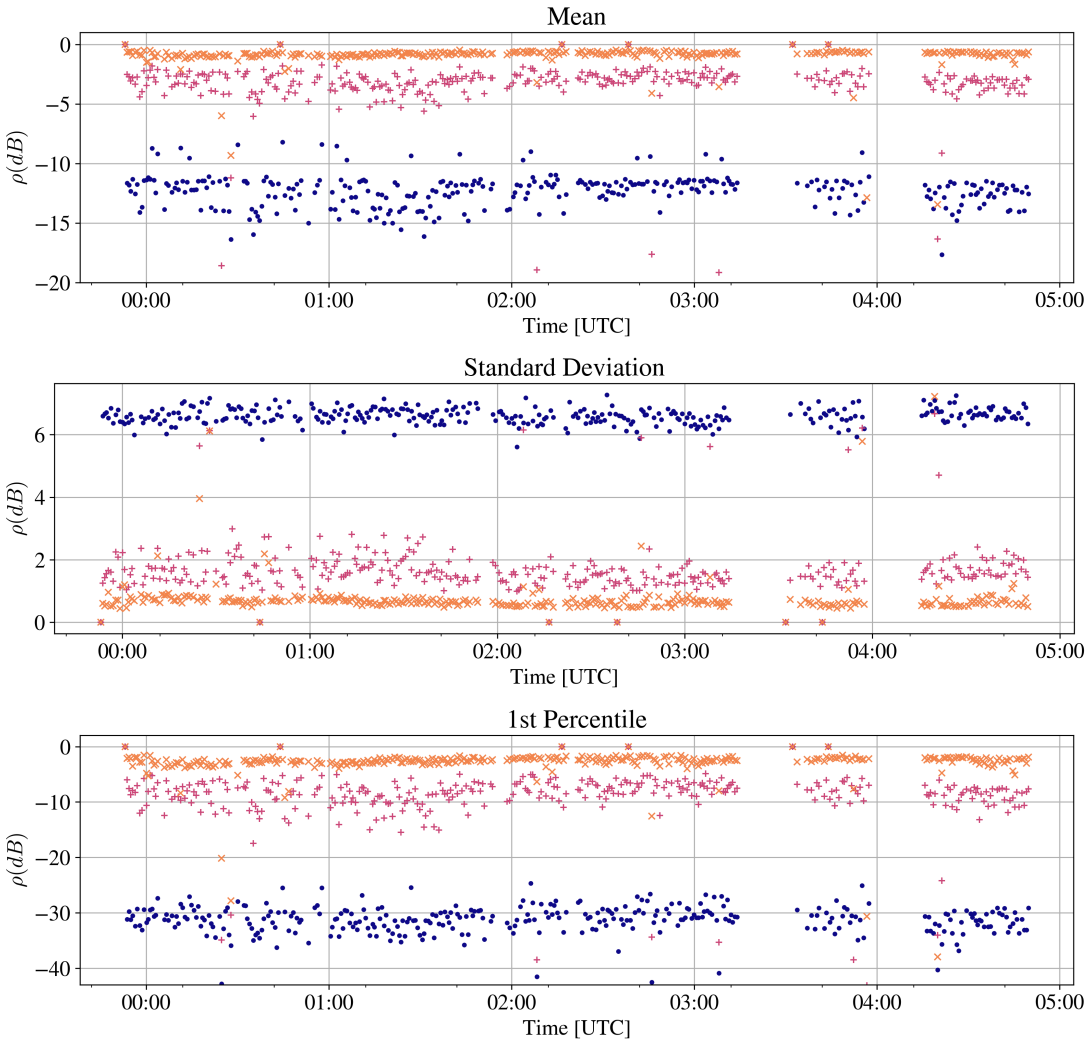

Figure 5.7: Statistical analysis of the coupled flux of a 1550 nm LEO downlink as a time-series. The satellite is assumed to be at zenith. From top to bottom, the mean performance, standard deviation, and 1st Percentile are shown. Each subfigure displays the time-series data under different AO conditions, where circles, pluses, and crosses represent no AO, tip/tilt-only AO, and full AO, respectively.

5.4.1 Predicted downlink performance (time-series)

Figure 5.7 shows the predicted performance of a particular FSOC system operating on the night of the 20th of April. The improvement in link performance is demonstrated by simulating the same system without AO correction, with tip/tilt only AO and with full AO, relative to the diffraction-limited case.

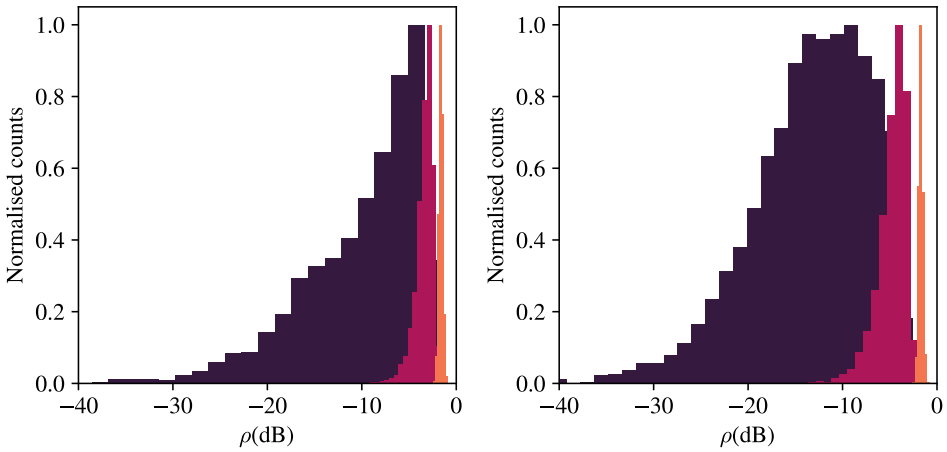

Figure 5.8: Histograms of the coupled power for all three AO configurations derived using the best and worst case turbulence measurements (left and right, respectively). (Purple) Without AO. (Pink) With tip/tilt correction only. (Orange) With full AO.

By comparing with figure 5.2, it can be seen that the mean coupled flux is correlated, with a correlation coefficient of 0.995, with the strength of the ground layer turbulence when there is no AO correction. This is a key determining factor for signal loss from the night the data was measured. Both tip/tilt and full phase correction significantly improve the coupling efficiency with a mean improvement of 9 dB and 11 dB, respectively.

Full AO offers a relatively modest improvement to coupling compared to tip/tilt only AO. Such improvements include a mean 2 dB increase in coupled power and an increase in temporal stability. The variation in the coupled power, defined by the width of the distribution, is now dependent on the atmospheric scintillation for both AO configurations whereas without AO was dependent on the phase of the wavefront at the receiver contributing to poor coupling efficiency. Table 5.3 shows the summary statistics from predicted downlink performance for the 3 AO configurations.

From table 5.3, the 1st percentile shows that for a communication link expected to operate with 99% uptime, using tip/tilt AO and full AO can result in FSOC performance improvements of up to 11 dB and 25 dB, respectively. This addition means there is

Table 5.3: Summary statistics from predicted downlink performance using different AO configurations.

AO configuration	Mean	Standard Deviation	1st Percentile
No AO	-12.6	6.99	-32.8
Tip/tilt AO	-3.57	3.40	-21.2
Full AO	-0.981	1.58	-7.54

less dependence on weak turbulence conditions for a stable communication link.

Figure 5.8 shows histograms of the coupled flux from simulations under the best and worst conditions observed during the campaign. The mean coupling efficiency fluctuates by at most 9 dB throughout the night when no AO is used. In contrast, the fluctuations are smaller with the use of tip/tilt AO and full AO, at 2 dB and 1 dB, respectively. This leads to the conclusion that the implementation of either AO system is essential to maintain a stable FSOC link under the varying turbulence conditions expected in urban environments.

5.4.2 Predicted downlink performance (LEO transit)

The atmospheric parameters used here were averaged over an 8-minute period at 00:33 AM to represent the duration of a LEO transit. Equation 3.6 is used to scale r_0 values to different zenith angles. This equation only remains true for weak fluctuations therefore ζ is restricted to be less than 60° (Andrews et al., 1995).

Lower elevation angles result in stronger distortions as the light propagates through the atmosphere. There are two main problems when considering propagation from satellite-to-ground. At low elevations, the atmospheric turbulence that the light propagates through is effectively thicker. This results in a smaller r_0 which can be mitigated with AO. There is also a larger propagation distance through stronger atmospheric layers meaning an increase in atmospheric scintillation, this cannot be corrected by AO alone.

Figure 5.9 shows that the uncorrected system exhibits a large variance in coupled power

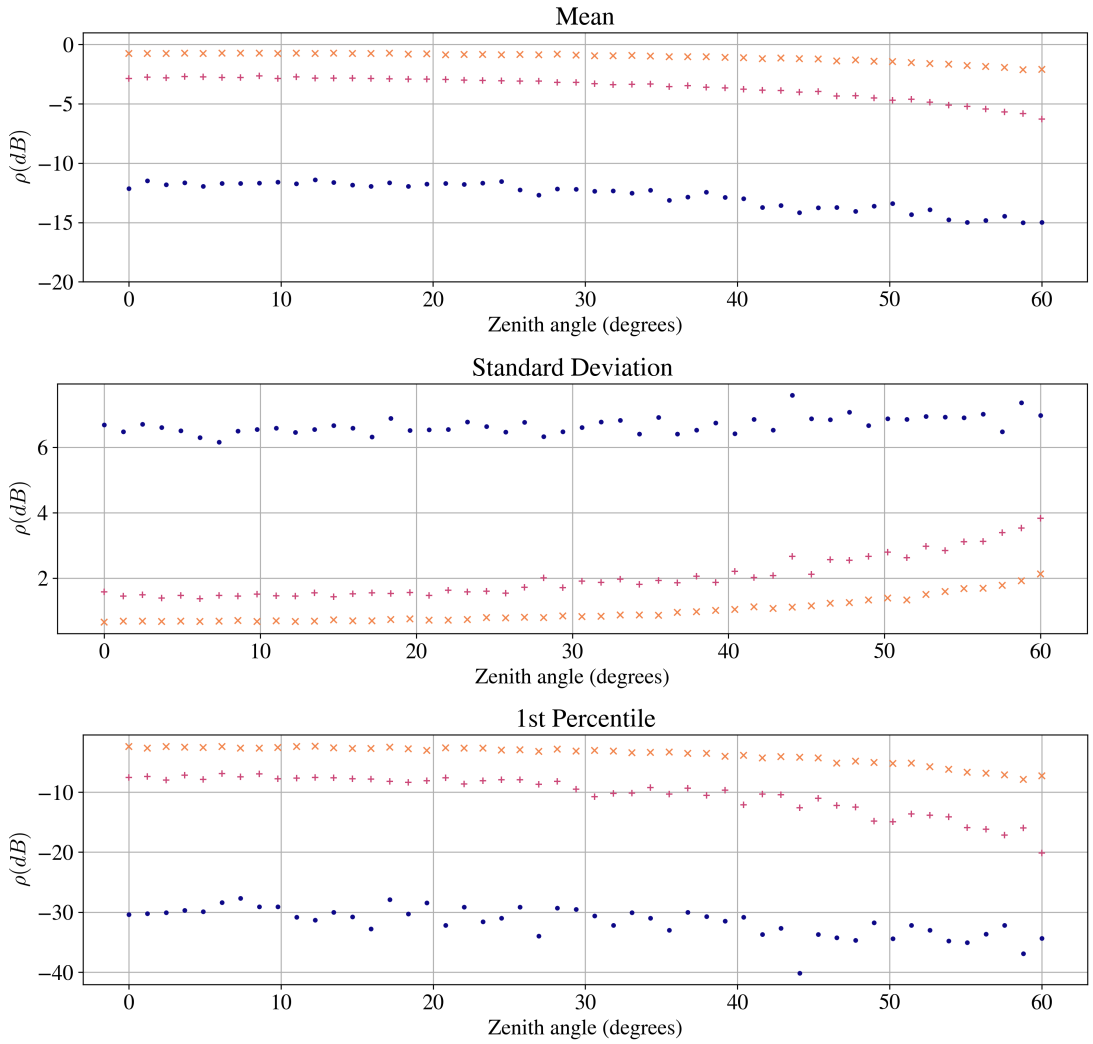

Figure 5.9: Intensity distributions for a downlink from a LEO satellite into a single mode fibre at varying zenith angles. From top to bottom: the mean, the standard deviation, and the 1st percentile. Each subfigure displays the data under different AO conditions, where circles, pluses, and crosses represent no AO, tip/tilt-only AO, and full AO, respectively. The HV distribution was generated to replicate the turbulence conditions observed at 00:33 AM (UTC). Negative zenith angle indicates a rising target. Note the change in y-scale between sub-figures.

across all zenith angles, with the mean coupled power decreasing from -12 ± 6.7 dB at zenith to -15 ± 7.0 dB at a zenith angle of 60°. Tip/tilt-only correction significantly improves the system's performance, increasing the mean by 9.2 dB at zenith and 8.7 dB at 60°. With tip/tilt-only correction, the coupling reduces from -2.9 ± 1.6 dB at zenith to -6.3 ± 3.8 at 60°. As the zenith angle increases, the decreasing r_0 creates

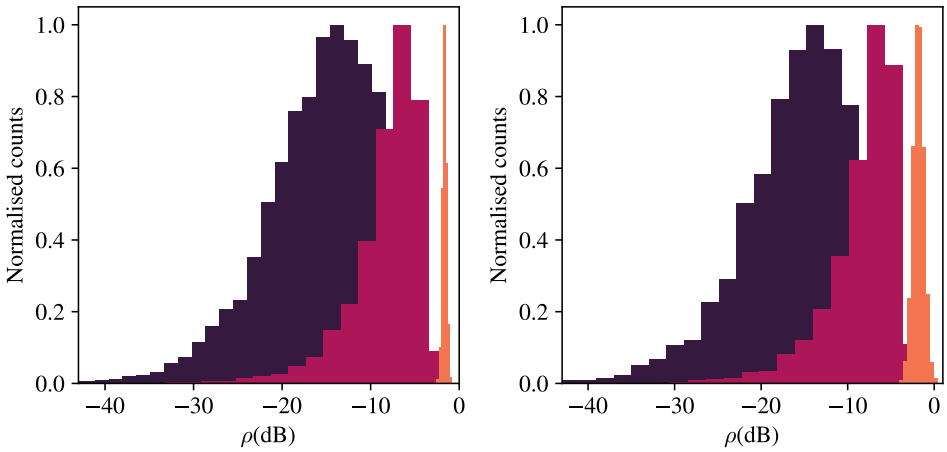

Figure 5.10: Histograms of the coupled power from orbiting satellite for all three AO configurations. The satellite is positioned at zenith and at 60° (left and right, respectively). (Purple) Without AO. (Pink) With tip/tilt correction only. (Orange) With full AO.

aberrations in the wavefront that cannot be corrected with tip/tilt correction alone.

In both AO configurations, the variance in the coupled power correlates with increasing scintillation as the elevation decreases. Full AO provides significant improvements to link stability at the largest zenith angles, increasing the mean by as much as 4.2 dB compared to the tip/tilt-only system. However, the variance in coupled power increases as the zenith angle increases, being 3.3 times larger at 60° compared to the zenith. At these larger zenith angles, the system becomes scintillation-limited.

It can be concluded that for a system with this optical design to operate effectively over a large range of elevations, the receiver should incorporate full AO to minimise the impact of decreased r_0 values at larger zenith angles. Histograms for targets at zenith and at 60° are shown in figure 5.10, comparing the performance across each AO configuration.

Table 5.4 compiles the statistics for each AO configuration for zenith angles of 0° and 60°. By looking at the 1st percentile data for 60°, it can be seen that tip/tilt AO provides a 13 dB improvement, while full AO offers a 27 dB improvement. Additionally,

at 60°, full AO results in a 13 dB improvement over tip/tilt AO, compared to only a 5 dB improvement at zenith. This shows that full AO offers the largest communication uptime, especially when regarding operations over increasing elevation angles.

Table 5.4: Statistics of the performance of a downlink during a LEO transit at 0° and 60° using different AO configurations.

AO Config.	0°			60°		
	Mean	Std Dev	1st Percentile	Mean	Std Dev	1st Percentile
No AO	-12.1	6.69	-30.4	-15.0	6.97	-34.4
Tip/tilt AO	-2.85	1.58	-7.58	-6.28	3.83	-20.1
Full AO	-0.755	0.656	-2.40	-2.09	2.13	-7.30

5.5 Conclusions

In this study, atmospheric optical turbulence above London's financial district was measured over a 4-hour period. The local temperature and windspeed on the night of the observations were typical for April. The Fried parameter, Rytov variance, and scintillation index were presented with mean values of 4.5 cm, 0.2, and 0.08, respectively. It is important to note that this experiment is intended as a demonstration, and additional data is required for comprehensive statistical analysis.

Vertical turbulence distributions were developed based on the well-known HV model, modified to match the measured scintillation and Fried parameter in the City of London on the 20th of April 2022. These distributions were used to replicate realistic urban turbulence conditions in simulation.

The modelling capability was demonstrated by predicting the performance of a LEO satellite-to-ground optical communication link as expected on the night of the measurements. This method of modelling the atmospheric channel has the potential to be expanded to simulate uplink and communication links to satellites at different altitudes. Assuming the best-case fibre-optic coupling where the satellite is at zenith, the predicted performance was presented as a time series. Results showed a significant im-

provement in both coupled flux and link stability with the addition of AO. Specifically, full AO phase correction improved the mean coupled power by as much as 11.6 dB compared to the uncorrected system, with a further reduction in standard deviation by 5.4 dB, indicating improved stability in the quality of the downlink. Full AO provided a slight advantage of 2.8 dB in mean coupled power and a 0.9 dB reduction in variance compared to tip/tilt AO in this configuration. Through the additional analysis of the 1st percentile, it can be determined that the uptime of a communication link is improved by 25 dB with the addition of full AO, reducing the systems dependence on weak turbulence conditions.

The predicted downlink performance from a LEO satellite as it transitions from 60° up through zenith and back down to 60° was also presented. Simulations show that in both the uncorrected and tip/tilt-only corrected, increased zenith angles reduced the mean coupled power by as much as 3.9 dB and 3.4 dB, respectively. Conversely, full AO provided a stable mean coupled power, showing a decrease of at most 1.3 dB between zenith and lower elevation angles. In both AO cases, increasing zenith angles exhibited an increased variance in the coupled power, an effect which can be attributed to scintillation at lower elevations. These results also demonstrate that implementing full AO provides a significant advantage in maintaining a downlink with a transiting satellite, improving mean coupled power by up to 12.9 dB and reducing variance by 4.8 dB compared to the uncorrected system when communicating with an orbiting satellite. Full AO also offers a notable advantage over tip/tilt-only AO at large elevation angles, with a 4.2 dB improvement at 60°, as tip/tilt-only correction begins to fail under the small r_0 values encountered at large zenith angles. It was also observed through the 1st percentile that there is an increased communication uptime, by 27 dB, by using full AO compared to without AO. Additionally, at 60°there is a 13 dB improvement between tip/tilt AO and full AO, reiterating the need for full AO especially when considering maximising downlink uptime over large zenith angles.

CHAPTER 6

Introducing TURBO: a 24-hour continuous turbulence monitor in Barcelona, Spain

6.1 Introduction

Atmospheric optical turbulence serves as a key limiting factor in the performance of FSOC systems. Therefore, it is important to understand the optical turbulence parameters at the location of an optical ground station (OGS). This information can be obtained through the analysis of archival meteorological data and an assessment of the local environment's structure. However, to ensure accuracy, such models, as presented in Osborn and Sarazin (2018); Masciadri et al. (2017, 2023); Shikhovtsev et al. (2023), require validation through real measurements. TURBO (TURBulence mOnitor) is a research initiative between the University of Durham, European Space Agency (ESA) and Universitat Politècnica de Catalunya (UPC) which aims to address these challenges.

TURBO's main function is to be the first turbulence monitor to take continuous optical turbulence data in an urban environment. The instrument being used for this purpose is referred to as TURBO1 and will be installed within a dome on a building at UPC. TURBO1 will complement the array of atmospheric instruments stationed at UPC, in-

cluding sun photometers and an aerosol LIDAR. These instruments will not only aid in understanding how aerosols affect atmospheric turbulence but will also provide insights into the optical transmission through the atmosphere, independent of turbulent effects. The secondary function of TURBO is the design of a portable, smaller instrument referred to as TURBO2 which can be transported to multiple locations to verify forecasts and provide valuable data for other potential OGS sites.

In this study, the outcomes of two commissioning campaigns are reported. During the initial campaign, the focus was on setting up the instrument and addressing operational challenges. Subsequently, the first day and night continuous measurement of vertical optical turbulence in an urban environment was conducted. The results of this run are discussed, along with some preliminary discussions on the performance of an optical ground station under these turbulence conditions. Additionally, the secondary campaign, where TURBO2 was commissioned, is discussed, along with the presentation of the results of the comparison between the two instruments.

6.2 Local weather analysis

The weather analysis presented here has all been derived using archival data from ECMWFs (European Centre for Medium-Range Weather Forecasts) ERA-5 dataset (Muñoz-Sabater et al., 2021). It provides global atmospheric reanalysis data covering various meteorological variables, including temperature, wind speed, and humidity. The ERA-5 dataset provides 1-hourly data with grid sizes of 31 km^2 and offers 30 vertical layers between 0 km to 20 km in altitude. This data can be used for site characterisation, measurement validation and optical performance prediction.

Cloud cover is a primary contributor to signal loss and requires careful consideration when considering the placement of an OGS. Barcelona lies in the northwest of Spain along the Mediterranean coasts and as such has typically good weather conditions.

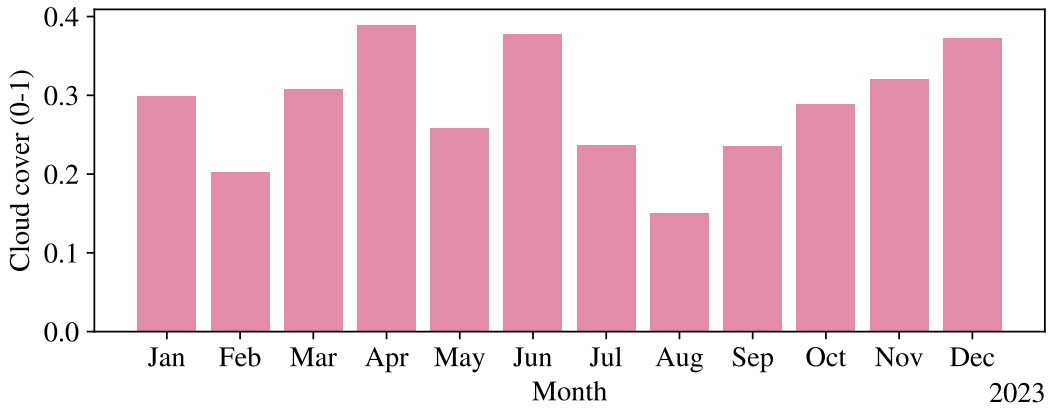

Figure 6.1: Fractional cloud coverage variation throughout the year 2023. Data is from the ERA-5 dataset.

Figure 6.1 shows the fractional cloud coverage in Barcelona throughout 2023, averaged over each month. The value 1 represents complete cloud coverage and 0 indicates clear skies. The calculations for each timestep are based on the maximum coverage across 29 layers. Over the year the cloud coverage varies between 0.15 and 0.40 fractional cloud coverage. The mean downtime of an optical system during this period will be 28% downtime due to cloud coverage alone.

It's important to note that this data represents only one year of observation. With the changing climate, future years may exhibit different patterns of cloud cover. Furthermore, future research could utilise UPC's vertical lidar to measure aerosol density, which contributes to signal loss through scattering and absorption.

6.3 First campaign

This campaign took place in early November 2023. The key objectives for the first campaign were to install TURBO1, identify potential operational issues and run the first continuous, day and night measurements in an urban environment.

6.3.1 TURBO1 installation

TURBO1 shares a similar design with SHIMMs used in previous sections but with some necessary changes. One key difference is its ability to operate continuously for 24 hours, which requires addressing low signal-to-noise issues during daytime star observations. To tackle this, the instrument now uses an infrared wavefront sensor the CRED3, which helps in detecting stars more effectively in the infrared spectrum.

Additionally, the SHIMM body has been redesigned for long-term durability, which uses an aluminium case which adds structure to the optics to prevent movement caused by gravity as the telescope slews. The unit also is sealed to prevent any dust from entering and to provide water resistance. Here the SHIMM is coupled to an 11-inch (28 cm) diameter Celestron C11 telescope which was on a CGX mount.

For alignment of the optics, adjustments can be made to the Shack-Hartmann wavefront sensors' XY-position, the wavefront sensor can also be rotated to ensure the spot pattern aligns square on the camera sensor, and the optical stage can be rotated to align parallel with the camera. This process allows us to verify the expected size, shape, and focus of the sub-apertures ensuring the accuracy of the pixel size.

It was observed that during night time, there was a reduction in signal in the camera. This occurred due to the formation of dew on the telescope corrector plate, which was also seen to form on the guide scope. Both are seen in figure 6.2. Dew forms on the surfaces of the telescope when the local temperature drops below the dew point. To address this issue in the future, a dew shield will be installed which works by keeping warm air in front of the corrector plate, preventing condensation. However, in instances of high humidity, condensation may pose a risk to TURBO's electrical components, which will require the closure of the dome before this becomes a problem.

Figure 6.3 illustrates the installation of the SHIMM on the pier within the dome. Mounting the telescope to a permanent pier, rather than using a tripod, offers several

Figure 6.2: Dew forming on the corrector plate of the telescope and on the guide scope.

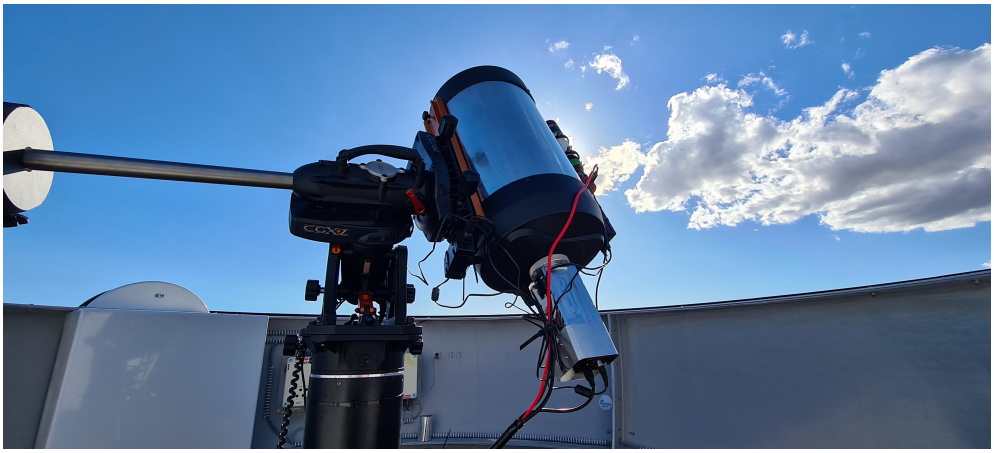

Figure 6.3: SHIMM installation onto the pier in the dome. Cable management of the SHIMM in the dome. To prevent the optical tube from overheating and generating additional turbulence, it was wrapped with silver tape over the original black paint.

advantages, providing increased stability, reducing vibrations, and ensuring a long-term alignment of the telescope.

In future, TURBO will develop so it can find targets either remotely or autonomously. The cables running to the SHIMM had to be arranged so that they would not snag and were long enough to reach all telescope positions. Cable ties were used to join cables running to the camera, guide scope camera and iris control. The telescope was then

Figure 6.4: Experimental set-up for 40-hour run.

manually moved to a maximum range of movement to verify a safe cable arrangement.

6.3.2 Experimental set up

The data presented here is taken on the rooftop of the same building, before installation on the pier. Unsafe wind speeds meant that the dome was not safe for a complete installation. Due to the lack of weather protection and reliance on early-stage software, the SHIMM required continuous supervision throughout the 40-hour run, which was unsustainable for longer periods.

This experiment took place at the tail end of Storm Ciarán, a windstorm which severely impacted central Europe, therefore the measured data may diverge from the typical weather patterns observed in Barcelona during this season.

6.3.3 Results of 40-hours of continuous measurements

The results of the continuous measurements taken over 40 hours are presented. To the best of current knowledge, this is the first continuous optical turbulence measurement taken in an urban environment that includes both daytime and nighttime measurements. The results and any anomalies found in the data are discussed. There are gaps in the data partway through the second night of measurements, attributed to high winds shaking the star out of the field of view. All measurements presented here are scaled to both zenith and 500 nm wavelengths.

The wind speeds of the available atmospheric layers are presented in figure 6.5 for a point of comparison to the observed turbulent conditions. Although the strong wind layer observed at approximately 15 km aligns with the typical altitude range of jet streams, confirmation of its classification as a jet stream is not possible due to insufficient data (Lutgens, 2013). Both high- and low-altitude wind speeds during the first 10 hours are significantly higher than at any other time during the experiment. Subsequently, both high- and low-altitude wind speeds decrease, potentially corresponding to the passing of Storm Ciarán.

Figure 6.6 plots the measured Fried parameter, r_0 throughout the run. The integrated r_0, as shown here, is a measure of how aberrated the wavefront is as it reaches the ground. The strength of this determines the extent of corrections required by an adaptive optics system. Through the first 15 hours of the experiment, r_0 remained relatively stable at around 5 cm, getting stronger in the daytime. This r_0 value is similar to that measured in London, presented in chapter 5. This corresponds to the high wind speeds at all altitudes shown in figure 6.5.

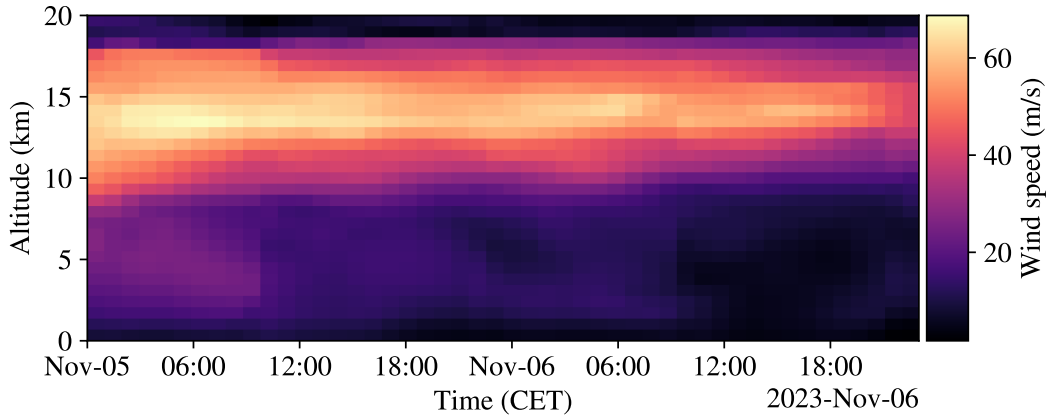

Figure 6.5: Wind speed as a function of altitude and time. Data sourced from the ERA-5 reanalysis dataset.

Between 12:00 and 18:00 each day, an increase in the r_0 value corresponding to a decrease in turbulence strength is exhibited. This is believed to be an effect of diurnal heating, as it occurs at the same time each day. This phenomenon is observed in each dataset and will be discussed further below.

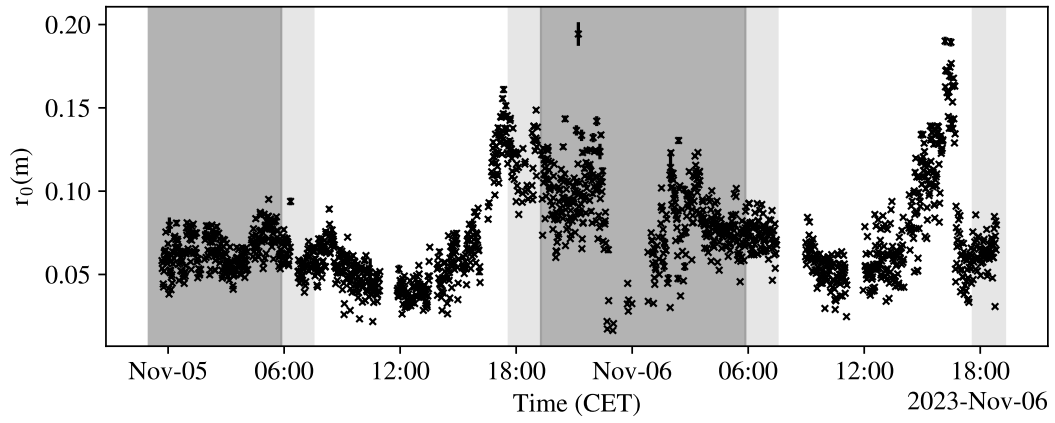

Figure 6.6: Measured r_0, scaled to zenith and to a wavelength of 500 nm.

The measured Rytov variance (σ_R^2) is presented in figure 6.7. Over the first 17 hours, the measured σ_R^2 lies around 0.8 and remains stable, this corresponds to the strong high-altitude winds observed in figure 6.5. This strength corresponds to moderate to high turbulence strengths. After 17:00, the σ_R^2 becomes weak, reaching a minimum at

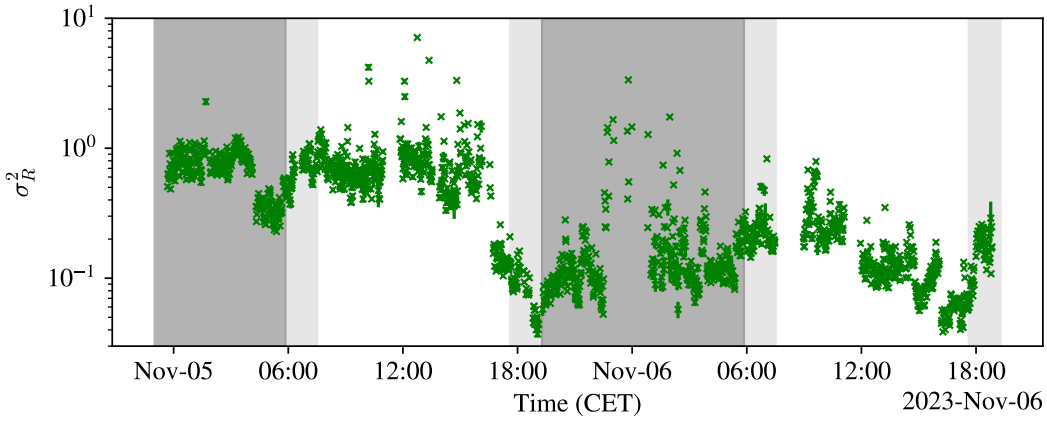

Figure 6.7: Measured σ_R, scaled to zenith and to a wavelength of 500 nm.

19:00, which is the point of sunset. There is an increase in σ_R^2 throughout the night, perhaps due to the convection caused by heat dissipation from the ground. Throughout the second day of measurements, there is a reduction in σ_R^2 until 18:00, when it begins to increase. The value of σ_R^2 seems to be independent of day or night time conditions. The most observed changes are seen in the transition between night and day.

Figure 6.8 illustrates the measured isoplanatic angle, θ_0. The trend of the isoplanatic angle closely mirrors that of σ_R^2, indicating stronger turbulence on the first day compared to the second, with both days showing a reduction in turbulent strength at 18:00.

The value of the isoplanatic angle uplink is important for pre-compensation. When communicating from the ground to a GEO-satellite, both the Earth and the satellite spin by 4 arcseconds between the transmission and reception of data. Precompensating the phase from the downlink onto the uplink can help mitigate turbulent effects. However, if the isoplanatic angle is significantly smaller than 4 arcseconds, the phase from the downlink becomes uncorrelated for the uplink. This is the case for all θ_0 measurements, indicating that precompensation may fail when using the downlink directly. Alternative methods for obtaining the phase necessary for successful precompensation could be explored, such as employing a laser guide star or numerically estimating the

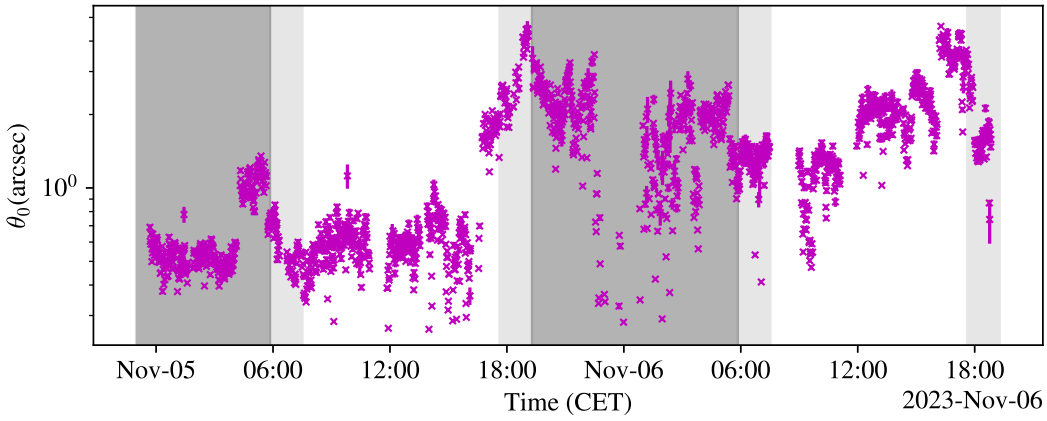

Figure 6.8: Measured θ_0, scaled to zenith and to a wavelength of 500 nm.

phase.

The turbulent data measured in the preceding figures exhibits fluctuations over comparable time scales. For instance, during weak turbulent conditions, larger values of r_0 are observed alongside smaller values of σ_R^2, while the opposite holds for strong turbulent conditions.

In each dataset, it is observed that the optical turbulence became much weaker towards 18:00 of each day, as the sun began to set. This is some of the weakest observed turbulence conditions throughout the run. This is a pattern that has been documented and observed (see Good et al. (1988)) and is attributed to the lack of temperature gradient between the boundary layer and the ground leading to reduced convection.

Table 6.1 summarises the statistics of these histograms, providing the mean, first quartile (Q1), and third quartile (Q3) for each turbulent parameter.

Table 6.1: Summary statistics for turbulent parameters

Parameter	Day			Night		
	Mean	Q1	Q3	Mean	Q1	Q3
r_0 (cm)	5.6	3.9	7.0	6.6	5.2	7.7
σ_R^2	0.36	0.18	0.42	0.36	0.18	0.40
θ_0 (arcsec)	1.1	0.79	1.5	1.1	0.81	1.5
τ_0 (ms)	3.2	1.8	4.0	3.9	1.8	5.9

In summary, the measured turbulence conditions observed at UPC, Barcelona, exhibit large temporal fluctuations. To a first degree, the strength of the turbulent effects appears to correlate with the atmospheric wind speeds. However, changes in turbulence strength over smaller time scales may require further observations, as there is limited indication of the underlying factors driving these fluctuations. Furthermore, despite this being the largest continuous dataset on urban atmospheric optical turbulence, additional data is required before the behaviour of this turbulence can be understood and the site satisfactorily characterised.

6.3.4 Estimating FSOC performance using turbulence measurements

The motivation behind the TURBO project is to understand the performance of an optical system in an urban environment. Presented here are the results of simulations aimed at estimating the performance of optical communication systems under the measured conditions seen in section 6.3.3.

The TURBO analysis software can measure an estimation of the vertical profile of optical turbulence strength using an autocorrelation between the intensities of the spots in the wavefront sensor (Griffiths et al., 2023). These can be used in simulation to estimate how a laser beam will propagate through specific turbulent conditions. A Monte-Carlo approach can be used to achieve statistical information about this.

6.3.4.1 Investigating diurnal variations

If these measurements were taken at an astronomical site, one would expect night time turbulence conditions to be noticeably weaker. However, the measurements indicate that in an urban environment such as Barcelona, stronger turbulence can occur at night, and weaker turbulence can occur during the day. Despite this, diurnal fluctuations are still evident, such as a repeating pattern of turbulence progressively weakening after

Layer altitude (km)	r_0 (m) at 500nm ($\zeta = 0$)	r_0 (m) at 1550nm ($\zeta = 49°$)
0	0.04	0.12
4	0.08	0.26
12	0.20	0.61
20	0.29	0.90

Table 6.2: Measured r_0 values of the turbulent layer under worst conditions observed at 13:30 and corresponding r_0 scaled for a GEO feeder link (wavelength: 1550 nm, zenith angle: 49°).

Layer altitude (km)	r_0 (m) (500 nm, $\zeta = 0$)	r_0 (m) at (1550 nm, $\zeta = 49°$)
0	0.17	0.52
4	0.30	0.93
12	0.38	1.2
20	*	*

Table 6.3: Measured r_0 values of the turbulent layer under best conditions observed at 18:20 and corresponding r_0 scaled for a GEO feeder link (wavelength: 1550 nm, zenith angle: 49°). Where r_0 is denoted by a *, the value is too large that it cannot be measured.

midday. In this section, the impact of these fluctuations on the performance of a communication system will be examined.

Four-layer profiles of turbulence strengths from the best and worst conditions observed in the first day of data, measured using the SHIMM, are presented in tables 6.2 and 6.3 as r_0 values. These correspond to the midday and the transition period at dusk. Here, the measured values are compared to the scaled parameters that correspond to the turbulence strengths of an optical channel that would be used to communicate with a GEO satellite. The zenith angle between a GEO satellite and an observer in Barcelona will vary depending on the satellite's position along the GEO belt. For a satellite that is due south of an observer in Barcelona, it will be positioned at a zenith angle of 49°, this value will be used throughout this section (Soler and Eisemann, 1994).

Figure 6.9 and 6.10 show single realisations of the intensity and phase profiles, respectively, of a laser beam that has propagated through the strongest and weakest turbulent profiles from day 1. These are to emulate a downlink in such conditions. In the weakest case, the intensity fluctuations exhibit a smaller variance compared to

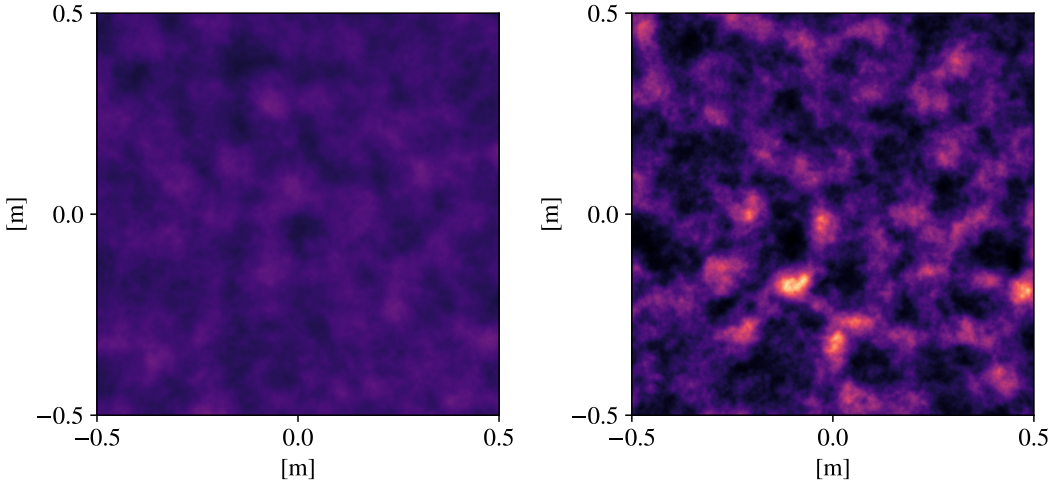

Figure 6.9: The simulated intensity of a plane wave propagating through phase screens with C_n^2dh strengths equivalent to the observed layers on the first day of measurements, plotted on the same z-scale. Weak atmospheric turbulence conditions, simulated using profiles observed at 18:20, are depicted on the left, while strong turbulence conditions, simulated using profiles measured at 13:30, are shown on the right. The input r_0 values are scaled to 1550 nm, and a zenith angle of 49°. Propagation is performed at the same wavelength, with the distances between profiles scaled to match this zenith angle.

the strongest cases, where there are very bright spots of intensity and very dim spots within the structure. Additionally, in the weakest case, the phase structure (seen in Figure 6.10) is relatively flat compared to the strongest case, where both high- and low-order phase fluctuations are evident. This suggests that the optical link performs worse under the strongest turbulence conditions. The measured profiles can also serve as inputs for Monte-Carlo simulations, which will be used to explore and discuss the differences between these two turbulent states in further detail below.

Figure 6.11 displays histograms generated from a Monte Carlo simulation representing a downlink through the strong and weak turbulence profiles. Each simulation is iterated over 1000 atmospheric realisations to reach statistical convergence. These simulations were conducted using FAST, as discussed in Chapter 5. The output, I_{dl}, represents the received intensity normalized to the unaberrated case, with 0 indicating the intensity received in the absence of turbulence. In the weaker case, significant improvements

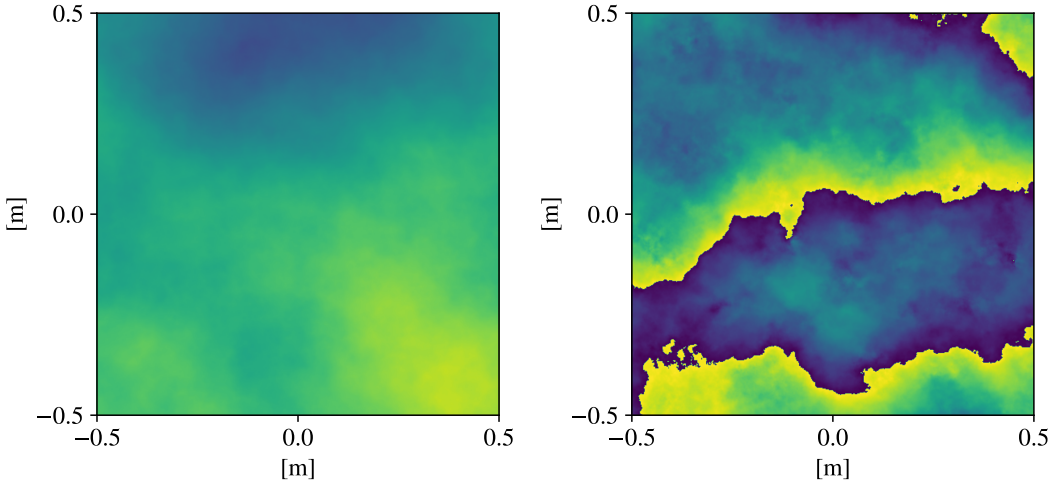

Figure 6.10: The simulated phase profile corresponding to the beam in figure 6.9, with the z-axis scaled to -π and +π. The discontinuities in the phase are due to phase wrapping.

are observed with the inclusion of either tip/tilt only or full adaptive optics correction, with 44% and 54% of the data achieving coupled intensity greater than -1 dB, respectively. There is also only a small improvement in the use of full AO over tip/tilt-only correction. The distributions for the strongest observed conditions are unsurprisingly worse where even with AO correction, there are still signal losses. With full AO, the system has a similar coupling distribution to the weakest conditions without AO. For a communication system to compensate for this it will need to resend a missing signal several times until it is detected. As explored in chapter 3, the effectiveness of an optical link depends not only on atmospheric conditions but also on factors such as receiver size, transmitting beam diameter, and AO system configurations (including wavefront sensor type, sub-aperture size, wavefront sensor noise, loop time, etc.). A few of these parameters will be explored in an attempt to optimise an FSOC system for these conditions. In each case, the median coupled intensity relative to the unaberrated coupling and its variance shall be presented. In doing so, the signal degradation from propagating effects alone can be studied and how they can be improved with AO correction. The received power of a 1 W transmission in 1550 nm through each

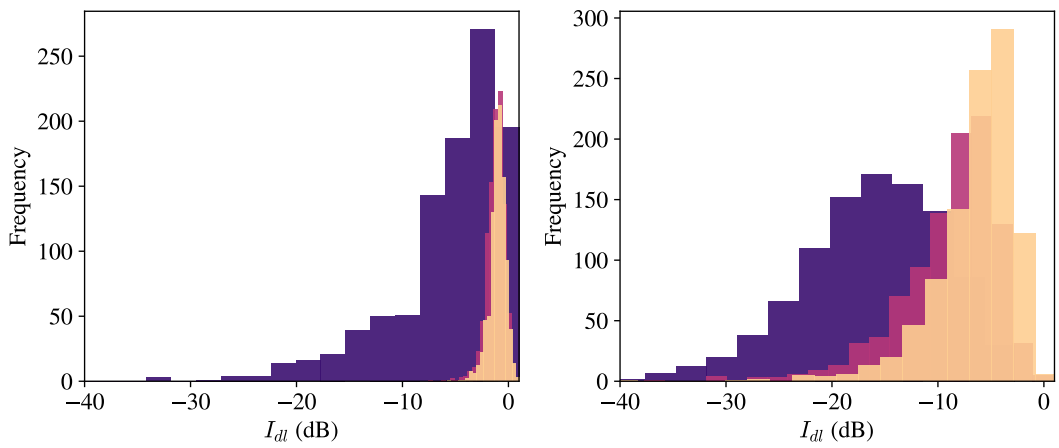

Figure 6.11: Histograms of the predicted received intensity relative to the unaberrated case, I_{dl} in downlink FSOC performance over a day. The system uses a 0.5 m diameter circular receiver. (left) Weakest measurements turbulence. (right) Strongest measured turbulence. The colours dark purple, purple and yellow correspond to no adaptive optics, tip/tilt only correction and full adaptive optics correction.

configuration is also presented.

Receiver diameter (downlink)

With increased aperture area, there increases the probability of photon detection. However, measuring over a larger wavefront increases the effective turbulence strength (D/r_0) requiring more complex AO systems. Here, the effect of increasing aperture size on the coupled intensity is explored.

In this simulation, noise is not included in the wavefront sensor camera, allowing the assumption that the centroid of each sub-aperture on the wavefront sensor is measurable regardless of scintillation. However, in reality, scintillation can cause variances across the wavefront sensor, leading to instances where scintillation-induced nulls occur in spot measurements. This reduces the system's ability to accurately reconstruct the wavefront.

Figure 6.12 shows the distributions of median I_{dl} for downlink with different receiver sizes. In the weakest observed conditions, the receiver diameters less than 0.2 m exhibit the highest coupling efficiency in all configurations, with all median values nearing the

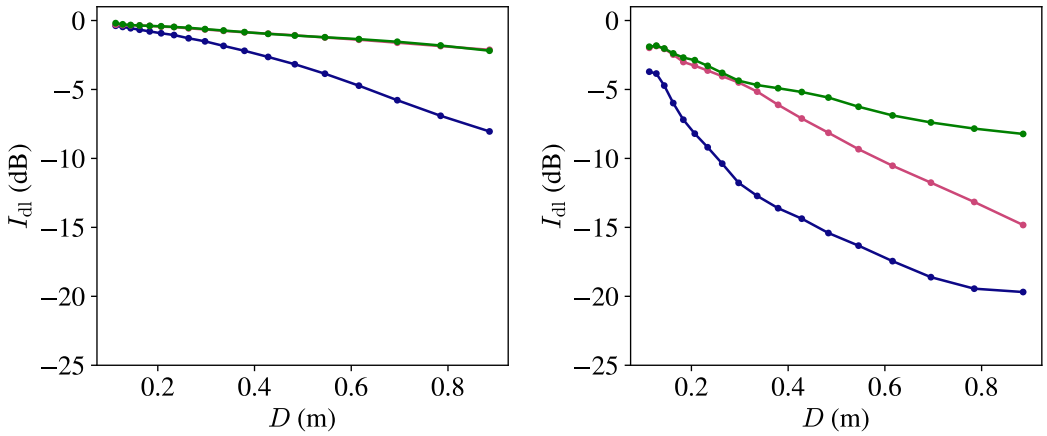

Figure 6.12: Median I_{dl} for downlink using different receiver diameters, D. Using the weakest measured turbulence condition and the strongest measured turbulence conditions, left and right, respectively. The colours represent different correction methods: blue for no AO, pink for tip/tilt-only correction, and green for full AO correction.

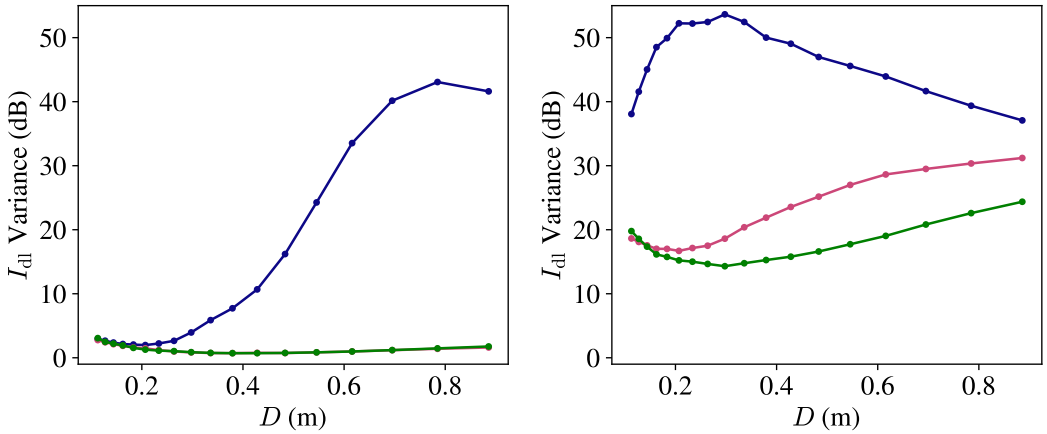

Figure 6.13: Variance in I_{dl} for figure 6.12 for downlink using different receiver diameters, D.

unaberrated case. The inclusion of AO only marginally improves the coupling of the light, as the receiver aperture is smaller than the measured r_0. By definition, in these conditions where the receiver aperture is smaller than the measured r_0, the spatial phase variance is sufficiently small that corrective measures such as adaptive optics are not necessary.

With increasing diameters, there is a reduction in the median I_{dl} for all configurations. The variance in I_{dl} remains almost unchanged for receivers with AO mitigation, while without AO, the variance in coupled intensity unsurprisingly worsens with increasing diameter size.

Additionally, there is no observed increase in coupled intensity when full AO correction is added compared to tip/tilt-only correction, indicating that the phase is primarily comprised of low-order phase perturbations. The decrease in coupled intensity with increasing diameter may be attributed to wavefront reconstruction errors due to a reduction in wavefront sensor pixel size.

Similar trends are observed in stronger conditions, where increased diameter sizes reduce coupled intensity. The overall reduction in median I_{dl} and increased variance compared to the weakest case can be attributed to increased scintillation causing photon losses. Full AO now offers improved coupled intensity over diameters of 0.3 m. The variance in the uncorrected scheme decreases past $\sim$0.3 m, possibly due to the averaging of intensity variances across the aperture. However, variance increases with larger diameters in both cases of AO correction, perhaps due to increased D/r_0 causing speckling in the sub-apertures and thus reducing the effectiveness of finding the centre spot of the focal plane. The most stable regime here is full AO correction, which offers the highest I_{dl} and the smallest variance.

Figure 6.14 shows the median signal losses due to propagating through the optical configurations and turbulence conditions from figure 6.12. These are shown for clarity as the parameter I_{dl} reflects purely the atmospheric effect and not the true performance of an optical system. It demonstrates that in the weakest turbulence regime, there is a reduction in signal losses with increasing receiver size, with a $\sim$15 dB increase between a 10 cm and a 0.8 m receiver in all. Here the addition of full AO only offers an improvement above 0.3 m receiver diameters.

Under stronger turbulence conditions, receivers larger than 0.3 meters benefit signific-

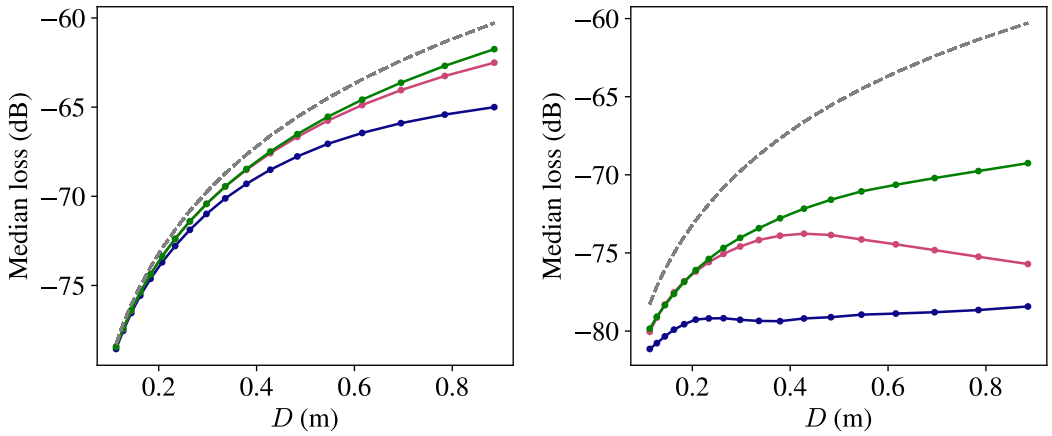

Figure 6.14: Median signal losses for varying receiver sizes at 1550 nm with fibre coupling. The colours represent different correction methods: blue for no AO, pink for tip/tilt-only correction, and green for full AO correction. The grey dashed line is the free space path loss in the absence of turbulence.

antly from the implementation of full AO to mitigate signal losses. In these scenarios, the difference between the unaberrated case and turbulent cases is pronounced, primarily due to signal losses caused by scintillation, which cannot be alleviated by AO at the receiver.

Figure 6.14 illustrates that in the strongest turbulence conditions, incorporating full AO reduces losses for receivers with diameters greater than 0.3 meters. Additionally, full AO enhances signal coupling by up to 5 dB compared to tip/tilt-only correction. Comparing scenarios without AO to those with full AO reveals improvements across all receiver diameters, with the largest receivers experiencing the most significant performance boost, achieving a 10 dB increase.

Furthermore, it is evident that across all diameter sizes, the performance without AO correction in the weakest case outperforms the performance with full AO in the strongest cases, highlighting the diverse range of conditions experienced at this particular location.

Beam waist (uplink)

The choice of the beam waist of the uplink laser involves consideration of beam diffraction and interaction with turbulent layers, as well as power requirements and eye safety. This study investigates how increasing the beam waist can alter the uplink's performance. Additionally, the inclusion of an LGS for uplink precompensation is considered. An LGS can be used to address the decorrelation between the downlink and uplink wavefronts induced by the point ahead angle, which is discussed in section 3.3.

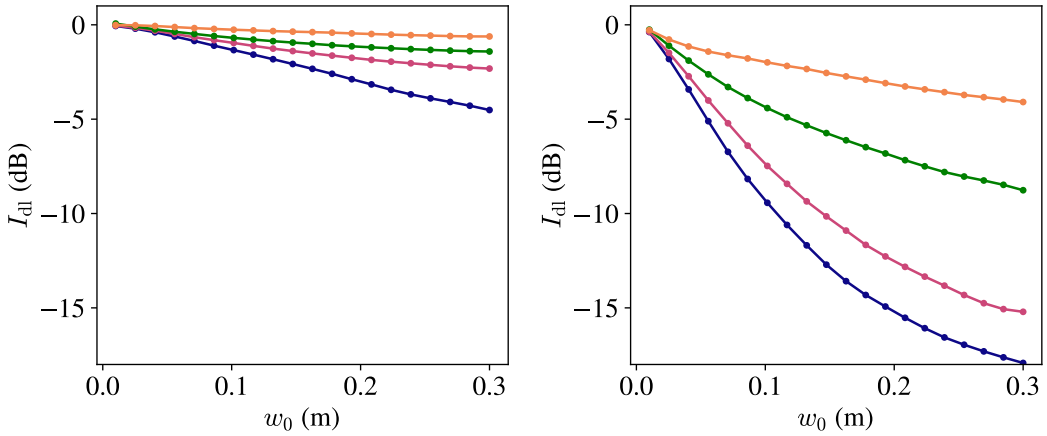

Figure 6.15: Median I_{dl} of uplink as a function of initial beam waist, w_0. The colours blue, pink, green and yellow correspond to no AO, tip/tilt only correction, full AO correction and LGS AO correction.

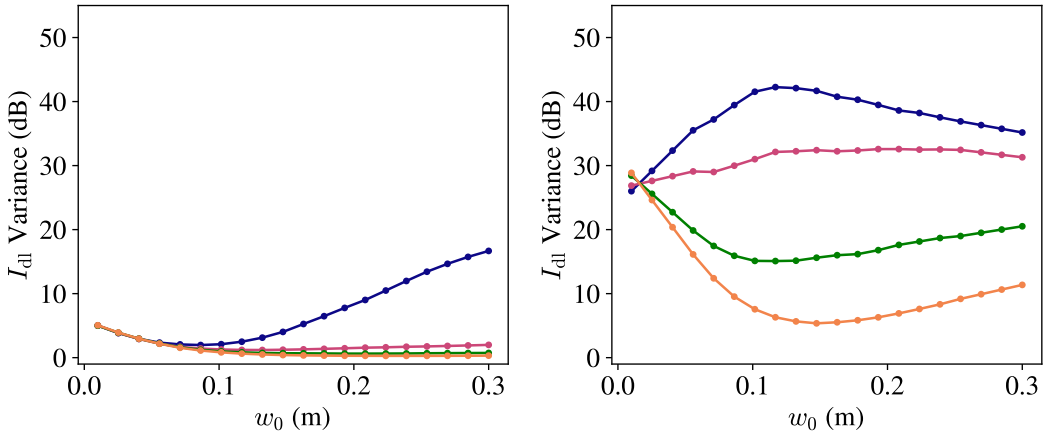

Figure 6.16: Variance in I_{dl} for figure 6.15 for downlink using different beam waists, w_0.

Figure 6.15 and 6.16 show the median I_{dl} and variance in I_{dl}, respectively, for varying launch sizes. As seen in the previous section, in the weakest observed turbulence conditions the performance of all 4 AO configurations works well. The uncorrected beam coupling worsens with increased beam size as it interacts with more atmospheric turbulence as it propagates, inducing increased beam wander.

For beam sizes less than 0.1 m, AO offers no improvement on the variance of the coupled intensity. Beams of this size undergo significant diffraction, leading to a deviation in the relationship between the phase of the beam and the phase of atmospheric turbulence encountered during propagation. This diminishes the reciprocity between the two phases, reducing the effectiveness of correction.

Here there are increasingly better system performances at larger w_0 with each AO scheme. However, this fractional improvement does not seem enough to warrant the use of an LGS AO system over tip/tilt-only correction. This agrees with prior simulations in this regime.

For the strongest cases, there is a clear reduction in the median I_{dl} with increasing beam waists in all cases, with the best performance being the LGS precompensation at a beam waist of 0.1 m. However, even with LGS AO, the system is still unable to reach the unaberrated case. One reason could be that without perfect wavefront precompensation, wavefront residuals will generate increased beam wander and scintillation after the interaction with turbulence. This explains the reduction in median I_{dl} and the increase in I_{dl} variance with an increase in beam size for AO and LGS AO precompensation.

Figure 6.17 illustrates the median signal losses corresponding to the optical links shown in figure 6.15 calculated using equation 2.1. In each configuration, optimal power transmission is achieved with the largest w_0 and the implementation of LGS AO. In the weakest turbulence conditions, the addition of the LGS AO precompensation system results in an improvement of up to 4 dB. Conversely, in the strongest turbulence con-

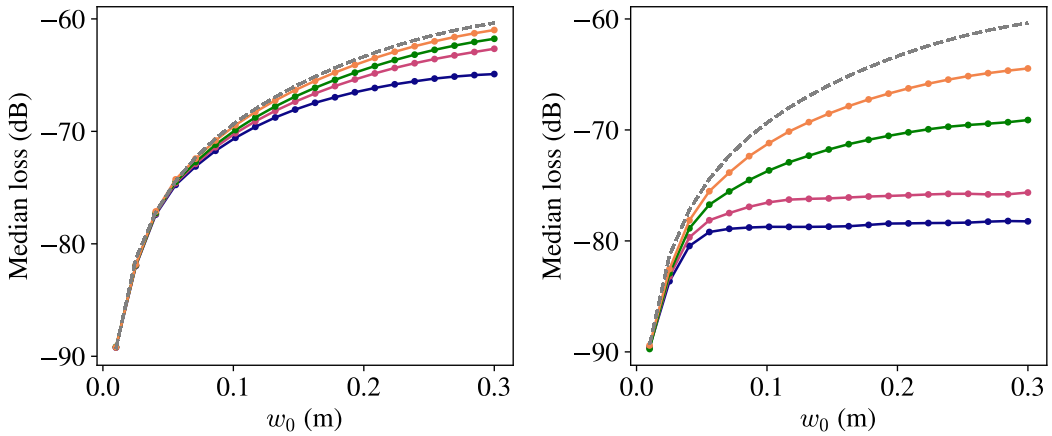

Figure 6.17: Median signal losses for optical link with varying beam waists at 1550 nm. The transmitted power is 1 W. The colours blue, pink, green and yellow correspond to no AO, tip/tilt only correction, full AO correction and LGS AO correction. The grey dashed line is the unaberrated case.

ditions, LGS AO precompensation provides a significant reduction in signal losses, up to 14 dB, for a 0.3 m beam waist.

In summary, the significant variations in turbulence conditions throughout the day must be carefully considered in the design of an adaptive optics system. For continuous operation of this communication system, it is important that the adaptive optics system can effectively operate in all encountered turbulent conditions. Constructing a single adaptive optics system capable of addressing two distinct turbulent states requires further studies into the optical design of the system and the form of AO. With the use of TURBO1, continuous atmospheric optical turbulence data can be gathered to aid in the optimisation of future optical ground stations.

In the case of non-continuous forms of FSOC, such as quantum key distribution, it is possible to schedule the downlink of information to coincide with these transitional periods when atmospheric turbulence is at its weakest. In such cases, as demonstrated by the above simulations, there may not be a need to include full AO or, potentially, any phase correction.

Figure 6.18: Assembly of TURBO2.

6.4 Second campaign

The second campaign ran in mid-February 2024 and the main objectives were to fix the key issues that were identified in the first campaign, assess the feasibility of an autonomous system that could be operated remotely, and to assemble and perform data assimilation using TURBO2.

The optical set-up for TURBO2 is identical to TURBO1 with the exception of the telescope tube, which is 8 inches (20 cm) instead of 11 inches (27 cm). This is joined to a CGXL mount, which is the same as TURBO1, but sits on a tripod instead of a metal pier. Figure 6.18 shows the set-up used throughout the run, which lies just outside of the dome of TURBO1. The dew shield is also used here, partly to allow for improved balancing of the telescope as it is heavier towards the back. In poor conditions, TURBO2 had to be powered down and a tarp was used to protect the telescope from rain, wind, and humidity.

For typical SHIMM operation, there has to be autoguiding to maintain the spot pattern

within the field of the wavefront sensor. This is due to the wavefront sensor camera having a small field of view so that any improper tracking in the scope can cause the spot pattern to drift. A guidescope is used to view the star over a larger field of view which can allow the tracking back to centre. One cause of the drift that can be encountered is inaccurate alignment, backlash in the gear system of the mount, unbalanced mount and flex in the optical system of the telescope. Here the SHIMM control software will operate in a closed-loop feedback system between the wavefront sensor and the telescope, adjusting the right ascension and declination of the telescope mount to maintain a well-centred spot pattern within the centroid.

If the target is lost for an extended period, for instance, due to cloud cover, reacquiring it during the daytime without visual feedback can be challenging. This is especially relevant for TURBO2, as it utilises a tripod, which is less stable than the pier used for TURBO1, and needs to be repositioned across different locations. To mitigate this challenge, performing a complete alignment of TURBO2, including a two-star alignment and full polar alignment, is essential. The need for precise alignment in combination with high cloud coverage meant that no daytime measurements were taken with TURBO2.

TURBO2 also experienced failures in relatively strong winds. Due to its lack of protection from a dome and its lighter weight compared to TURBO1, the wind caused the centroids to shake off the wavefront sensor camera. If TURBO2 is expected to operate in these conditions, a windshield can be used to prevent this.

6.4.1 Experimental results: Comparisons between TURBO1 and TURBO2

Intermittently poor weather throughout the second run meant that continuous data could not be gathered using both instruments. Presented here are four hours of concurrent data collected from TURBO1 and TURBO2, during which both observed the

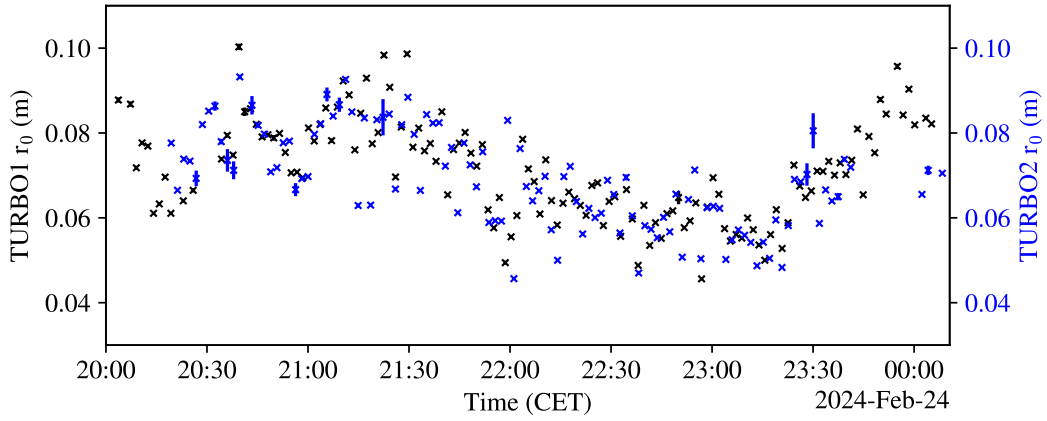

Figure 6.19: Comparisons between TURBO1 and TURBO2 measured r_0. All measurements are scaled to 500 nm and to zenith.

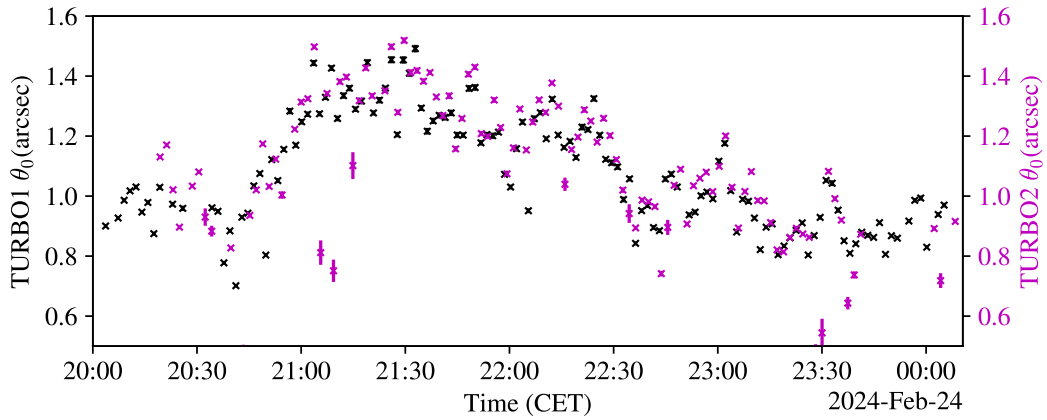

Figure 6.20: Comparisons between TURBO1 and TURBO2 measured θ_0. All measurements are scaled to 500 nm and to zenith.

same star. The aim of this experiment is to understand how a decreased aperture size may affect a SHIMM's ability to perform turbulence measurements.

Figures 6.19, 6.20, 6.21, and 6.22 present the measured turbulence parameters from both TURBO1 and TURBO2 throughout the night. σ_I^2 is now also presented as it is a direct measurement of the intensity variance in the centroids. All data was collected after sunset. At first glance, the measurements from both instruments exhibit good agreement, showing similar temporal variations in the measured parameters. It is noticeable that TURBO2 has a higher number of data points with large errors, attributed

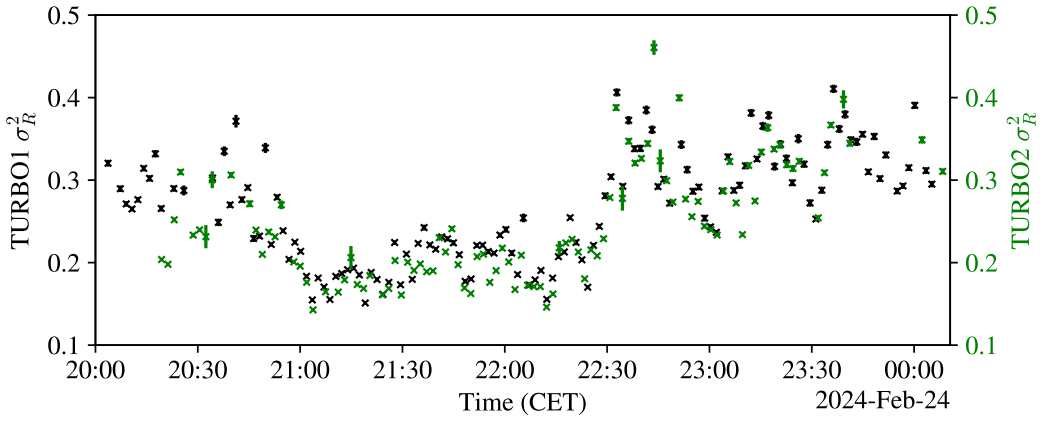

Figure 6.21: Comparisons between TURBO1 and TURBO2 measured σ_R^2. All measurements are scaled to 500 nm and to zenith.

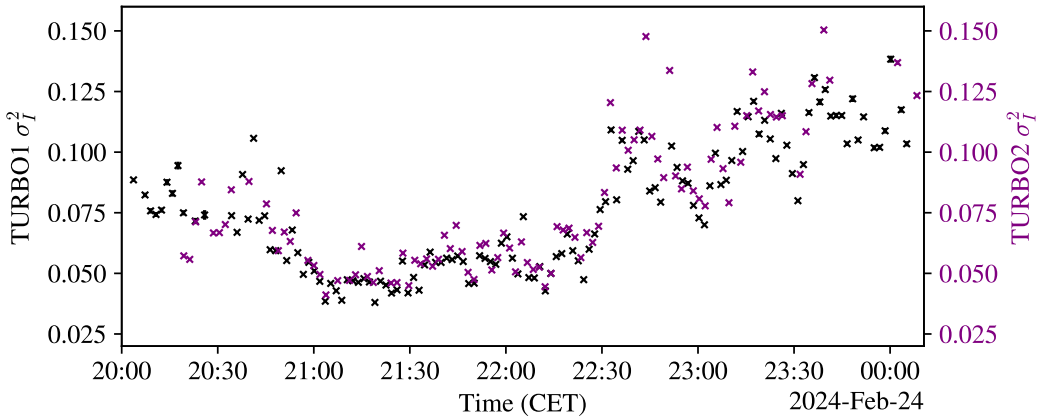

Figure 6.22: Comparisons between TURBO1 and TURBO2 measured σ_I^2. All measurements are scaled to 500 nm and to zenith.

to its susceptibility to wind shake.

Further comparisons between the datasets are shown in figure 6.23, whereby the measured data from each instrument is plotted against each other. There is, in general, a good agreement between the measurements of TURBO1 and TURBO2. There are some outliers in the data which may be due to reduced signal-to-noise or wind shake.

Visual analysis indicates that for all σ_I^2 measurements, TURBO1 measurements are slightly smaller than that of TURBO2. This is expected as TURBO2 has smaller

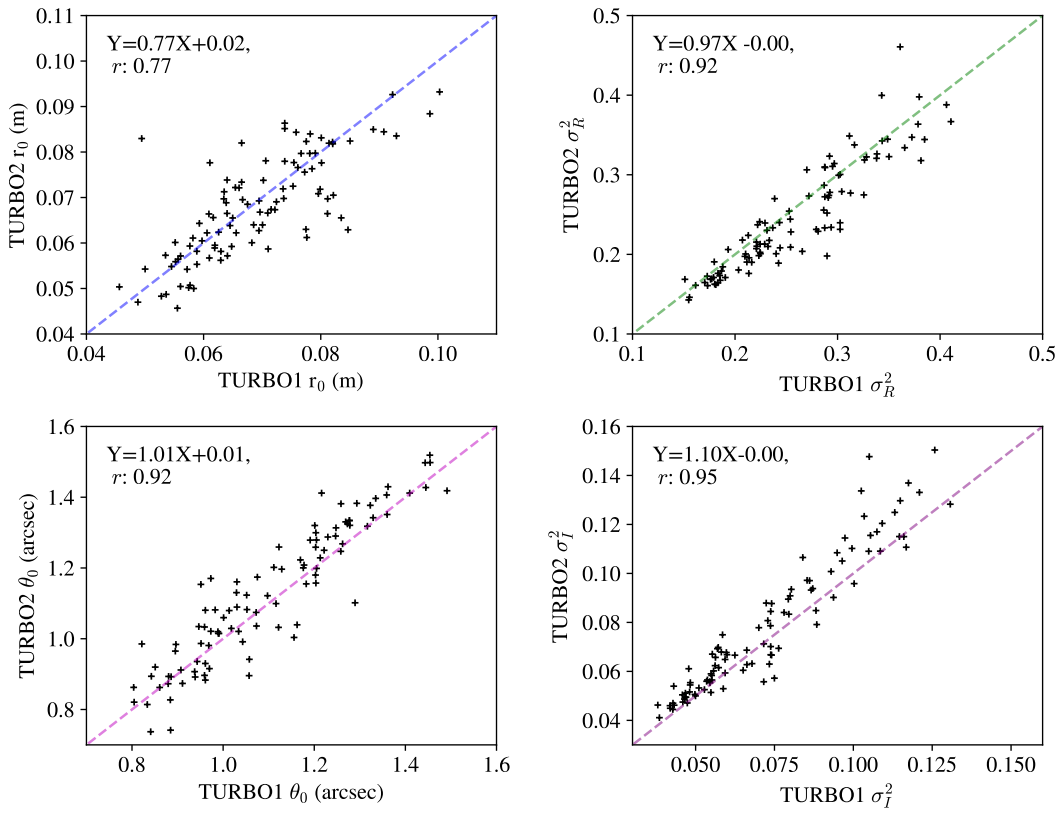

Figure 6.23: TURBO1 and TURBO2 measurements are plotted against each other for comparisons. The dashed line represents the relationship of Y=X. The linear fit to the data and the Pearson correlation coefficient, r, are shown in the top left of each plot.

sub-apertures, leading to a reduction in aperture averaging and thus an increase in intensity variances. Despite this, the two sets of data agree very well for two different instruments.

There are multiple factors that can contribute to the slight differences between the two datasets. Further data collection and analysis can help validate and improve the performance of both systems. Measurements should be conducted in both day and night turbulence regimes as TURBO2 is theorized to perform better in strong turbulence. This is due to its smaller pixel scale and sub-apertures, leading to increased resolution of the Shack-Hartmann spot positions and reduced speckling in stronger turbulent regimes, respectively. Additionally, a smaller collecting area leads to a reduced signal-

to-noise ratio. This reduction can potentially make it more challenging to locate targets below a certain magnitude, thereby limiting the number of usable targets.

6.5 Conclusions

This chapter covers the commissioning of the optical turbulence monitors, TURBO1 and TURBO2. These state-of-the-art instruments are designed to provide continuous, 24-hour turbulence data to aid in characterizing atmospheric turbulence in Barcelona. TURBO1 operates within a dome, with plans for automation to facilitate data collection during clear sky conditions. TURBO2 is designed to be more portable, allowing it to be transported to different locations for the characterization of various environments and to serve as a tool for validating optical turbulence forecasts. Future campaigns will focus on aiding TURBO1's full automation and testing TURBO2's functionality in both day and night conditions.

Furthermore, the first continuous day and night optical turbulence measurements taken in an urban environment are presented. The data demonstrates that turbulence levels can fluctuate over a wide range, such as r_0 evolving from 3 cm to 15 cm within a span of 3 hours. Additionally, it was observed that turbulence strengths decrease during the transition through sunset. Comparisons between the local weather data and the observed turbulence parameters reveal that high wind speeds can generate strong turbulence conditions.

Through the analysis of the continuous data, an evaluation of how an adaptive optics system may perform throughout a day in the observed conditions is conducted. The focus is on the degree of correction necessary for these conditions. It is observed that at the weakest measurements, only tip/tilt-only phase correction is necessary on the downlink for all receiver sizes up to 0.9 m. In the strongest conditions, full AO needs to be implemented for optimal performance. Similarly, for uplink precompensation, there is only a marginal improvement by implementing higher orders of AO correction.

However, in the strongest conditions, the best performance is achieved with LGS AO precompensation.

The second campaign where TURBO2 was first commissioned is also discussed. Data was collected simultaneously from both instruments over the course of 4 hours, allowing verification of the measurements of both instruments and the effect of an increased aperture size. Both instruments agree well, with certain potential measurement biases due to the smaller pixel size of TURBO2 and its smaller telescope diameter reducing the aperture averaging. However, further work is needed to understand these biases.

Future work will use the continuous data from the measurements of TURBO1 and TURBO2 to help perform site characterization. UPC's vertical LIDAR can be used in combination with the atmospheric optical measurements for a more comprehensive understanding of the environment. This will enable the assessment of the feasibility of establishing an optical ground station within Barcelona.

CHAPTER 7

Conclusion

This thesis explores the significance of optical turbulence in free-space optical communications, investigating some of the novel turbulent environments in which optical communication links must operate, specifically urban landscapes and across all zenith angles.

The results presented in this thesis can be used directly by researchers and engineers in the field of free-space optical communications who aim to simulate satellite-to-ground optical systems under relevant atmospheric conditions. Atmospheric turbulence is a significant obstacle to the successful propagation of light from transmitter to receiver; therefore, a comprehensive understanding of the optical channel is essential for accurately estimating system performance and for the effective design of optical communication systems. The methodologies employed in this thesis to model and analyse turbulence parameters can be further expanded to explore the full parameter space, allowing for the optimisation of key system components such as the receiver, transmitter, light source, modulation techniques, and turbulence mitigation strategies.

The initial study examines the impact of varying zenith angles on the integrated turbulence parameters σ_I^2 and r_0, addressing an important aspect of ground-to-satellite optical communications. This is particularly relevant for communication links operat-

ing across all zenith angles, such as those for LEO and GEO communication links at high latitudes. This relationship has not yet been studied using concurrent instruments. By employing two turbulence monitors, the study distinguishes between temporal variations and those caused by changing zenith angles. The experiment uses two identical turbulence monitors to sample zenith angles from 10° to 90°, while concurrently collecting data using a reference monitor positioned near zenith.

The findings indicate that the measured σ_I^2 and r_0 deviate from their respective models only at large zenith angles. There is strong agreement with both weak and strong fluctuation theories for σ_I^2 until zenith angles exceed approximately 80°. Beyond this point, weak fluctuations increase asymptotically, and strong fluctuations saturate to 1 in all instances, both estimating a higher σ_I^2 compared to observed values which reduce to near 0.3. The study also finds that r_0 aligns well with theory up to a zenith angle of approximately 70°. At larger zenith angles, both Kasten and Young's theories and secant scaling overestimate r_0, tending to 0.9 cm, whereas true measurements tend to near 2.5 cm, indicating weaker turbulence than these models predict. The discrepancy is likely due to the omission of optical propagation effects from the theory.

The limitations of conducting this experiment in an astronomical environment are discussed, and it is suggested that if this experiment were replicated in an urban environment, the divergence between theory and measurements would occur much earlier, as the strong turbulence regime will be entered at smaller zenith angles. Despite these challenges, the presented theory can effectively calculate atmospheric turbulence parameters within this turbulent environment. Thus, a SHIMM can serve as a reliable monitor at any astronomical site, allowing the extrapolation of measured turbulence parameters to a zenith angle as low as approximately 70°.

The secondary study focuses on the behaviour of atmospheric optical turbulence in an urban environment. Currently, optical turbulence measurements primarily target astronomical sites with ideal turbulence conditions or study horizontal links in urban

areas. As a result, there has been limited research on the vertical atmospheric pathway of turbulence in built-up areas.

Atmospheric optical turbulence was measured over London's financial district for a 4-hour period, marking the first measurements of optical turbulence in an urban environment. The Fried parameter, Rytov variance, and scintillation index were presented with mean values of 4.5 cm, 0.2, and 0.08, respectively. Vertical turbulence distributions were developed based on the well-known HV model, modified to match the measured σ_I^2 and r_0. These distributions were used to simulate realistic urban turbulence conditions. The results of Monte Carlo simulations were presented to investigate the performance of optical communication links throughout the measurement night, including best-case scenarios of fibre coupling with the satellite at zenith and the predicted performance as a time series. It was found that the addition of tip/tilt-only correction and full AO offered an improved coupling of 8.86 dB and 11.6 dB, respectively, compared to the uncorrected case. Additionally, it was observed that when communication links are established at zenith angles of 60° or higher, full AO is recommended, as the turbulence depths at these angles create aberrations that cannot be effectively mitigated using tip/tilt-only corrections, with an improvement of 4.2 dB at 60° between the two systems.

This study demonstrates optical turbulence measurements in an urban environment. Using the SHIMM in the City of London provides a beginning to data assimilation in urban environments, aiding the understanding of how these turbulent environments behave. Although the dataset presented here is modest, it represents an initial step towards comprehensive knowledge in this field.

Finally, the work covers the installation of a permanent instrument at Universitat Politècnica de Catalunya, Barcelona, Spain. These two instruments will be used for long-term data assimilation of the optical turbulence above Barcelona, data that is invaluable to the full realisation of optical communication systems.

This work presents 40 hours of continuous optical turbulence data, significantly expanding upon a previous study conducted in London, marking the first collection of day and night data in an urban setting. The study finds that turbulence data fluctuates significantly throughout the day and can change from strong to weak turbulence within a few hours. In summary, the mean values for r_0, σ_R^2, θ_0, and τ_0 were 6.2 cm, 0.36, 1.1 arcsec, and 3.6 ms, respectively. A decrease in turbulence intensity was observed during the transition through sunset. By comparing local weather data with observed turbulence parameters, it was concluded that strong turbulence conditions may be induced by high wind speeds.

The potential performance of a satellite-to-ground optical link in Barcelona was also studied, focusing on determining the level of correction required for optimal performance in these conditions. At the weakest measurements, only a marginal improvement was observed by implementing higher orders of AO correction. However, in the strongest observed conditions, full AO should be implemented, with the best possible performance being LGS-AO for precompensation on the uplink, offering at most a 15 dB improvement over the uncorrected case.

Further research will use ongoing data collection from TURBO to facilitate site characterisation. Additionally, the integration of UPC's vertical LIDAR data will complement atmospheric optical measurements and improve the understanding of the environment. This will provide a thorough assessment of the feasibility of establishing an optical ground station in Barcelona.

This thesis culminates many atmospheric optical measurements in novel environments. Through these experiments, the understanding of atmospheric optical turbulence has advanced, from its effects on light propagation at different zenith angles to present the first measurements in urban environments, laying the groundwork for future research and data assimilation efforts.

Bibliography

A. Abahamid, A. Jabiri, J. Vernin, Z. Benkhaldoun, M. Azouit, and A. Agabi. Optical turbulence modeling in the boundary layer and free atmosphere using instrumented meteorological balloons. *Astronomy & Astrophysics*, 416(3):1193–1200, 3 2004. ISSN 0004-6361. doi: 10.1051/0004-6361:20031390. URL http://www.aanda.org/10.1051/0004-6361:20031390.

A. G. Alkholidi and K. S. Altowij. Free Space Optical Communications — Theory and Practices. In M. Khatib, editor, *Contemporary Issues in Wireless Communications*, chapter 5. IntechOpen, Rijeka, 2014. doi: 10.5772/58884. URL https://doi.org/10.5772/58884.

L. C. Andrews. *Field Guide to Atmospheric Optics, Second Edition*. SPIE, 1 2019. ISBN 9781510619388. doi: 10.1117/3.2318080. URL https://www.spiedigitallibrary.org/ebooks/FG/Field-Guide-to-Atmospheric-Optics-Second-Edition/eISBN-9781510619388/10.1117/3.2318080.

L. C. Andrews and R. L. Phillips. *Laser Beam Propagation through Random Media*. SPIE, 1000 20th Street, Bellingham, WA 98227-0010 USA, 9 2005. ISBN 9780819459480. doi: 10.1117/3.626196. URL http://ebooks.spiedigitallibrary.org/book.aspx?doi=10.1117/3.626196.

L. C. Andrews, R. L. Phillips, and P. T. Yu. Optical scintillations and fade statistics for a satellite-communication system. *Applied Optics*, 34(33):7742, 1995. ISSN 0003-6935. doi: 10.1364/ao.34.007742.

L. C. Andrews, R. L. Phillips, C. Y. Hopen, and M. A. Al-Habash. Theory of optical scintillation. *Journal of the Optical Society of America A*, 16(6):1417, 6 1999a. ISSN 1084-7529. doi: 10.1364/josaa.16.001417. URL https://opg.optica.org/abstract.cfm?URI=josaa-16-6-1417.

L. C. Andrews, C. Y. Young, A. Al-Habash, R. L. Phillips, and D. E. Tjin-Tham-Sjin. Fade statistics associated with a space/ground laser communication link at large zenith angles. In M. C. Roggemann and L. R. Bissonnette, editors, *Propagation and Imaging through the Atmosphere III*, volume 3763, pages 268–277. International Society for Optics and Photonics, SPIE, 10 1999b. doi: 10.1117/12.363622. URL https://doi.org/10.1117/12.363622http://proceedings.spiedigitallibrary.org/proceeding.aspx?articleid=995809.

L. C. Andrews, R. L. Phillips, and C. Y. Young. *Laser Beam Scintillation with Applications*. SPIE, 7 2001. ISBN 9780819441034. doi: 10.1117/3.412858. URL https://spiedigitallibrary.org/ebooks/PM/Laser-Beam-Scintillation-with-Applications/eISBN-9780819478511/10.1117/3.412858.

L. C. Andrews, R. L. Phillips, D. Wayne, T. Leclerc, P. Sauer, R. Crabbs, and J. Kiriazes. Near-ground vertical profile of refractive-index fluctuations. *Atmospheric Propagation VI*, 7324(April 2009):732402, 2009. ISSN 0277786X. doi: 10.1117/12.820369.

R. Avila, J. Vernin, and E. Masciadri. Whole atmospheric-turbulence profiling with generalized scidar. *Applied Optics*, 36(30):7898, 10 1997. ISSN 0003-6935. doi: 10.1364/AO.36.007898. URL https://opg.optica.org/ao/abstract.cfm?URI=ao-36-30-7898https://opg.optica.org/abstract.cfm?URI=ao-36-30-7898.

M. Azouit and J. Vernin. Optical Turbulence Profiling with Balloons Relevant to

Astronomy and Atmospheric Physics. *Publications of the Astronomical Society of the Pacific*, 117(831):536–543, 2005. ISSN 0004-6280. doi: 10.1086/429785.

R. Barrios, S. Dimitrov, R. Mata-Calvo, and D. Giggenbach. Link budget assessment for GEO feeder links based on optical technology. *International Journal of Satellite Communications and Networking*, 39(2):160–177, 3 2021. ISSN 1542-0973. doi: 10.1002/sat.1371. URL https://onlinelibrary.wiley.com/doi/10.1002/sat.1371.

E. L. Bass. Aperture averaging of optical scintillations based on a spectrum with high wave number bump. *Optical Engineering*, 34(1):26, 1995. ISSN 0091-3286. doi: 10.1117/12.184051.

L. F. Beesley, J. Osborn, R. Wilson, O. J. D. Farley, R. Griffiths, and G. D. Love. Exploring atmospheric optical turbulence: observations across zenith angles. *Applied Optics*, 63(16):E48, 2024. ISSN 1559-128X. doi: 10.1364/ao.519063.

A. Belmonte. Feasibility study for the simulation of beam propagation: consideration of coherent lidar performance. *Applied Optics*, 39(30):5426, 2000. ISSN 0003-6935. doi: 10.1364/ao.39.005426.

A. Belmonte, A. Rodríguez, F. Dios, and A. Comerón. Phase compensation considerations on coherent free-space laser communications system. volume 6736, page 67361A, 10 2007. doi: 10.1117/12.740276. URL http://proceedings.spiedigitallibrary.org/proceeding.aspx?doi=10.1117/12.740276.

C. Bi, X. Qian, Q. Liu, W. Zhu, X. Li, T. Luo, X. Wu, and C. Qing. Estimating and measurement of atmospheric optical turbulence according to balloon-borne radiosonde for three sites in China. *Journal of the Optical Society of America A*, 37(11):1785, 11 2020. ISSN 1084-7529. doi: 10.1364/JOSAA.397894. URL https://opg.optica.org/abstract.cfm?URI=josaa-37-11-1785.

R. Biasi, D. Bonaccini Calia, M. Centrone, M. Enderlein, M. Faccini, O. Farley, D. Gallieni, D. Gooding, P. Haguenauer, P. Janout, D. Jenkins, F. Lison, J. Luis,

N. Martinez Rey, J. Osborn, C. Patauner, D. Pescoller, M. Reyes, L. Sabatini, L. Salvi, Z. Sodnik, D. Alaluf, M. Tintori, M. Tordi, M. Townson, H. Virdee, D. P. Wei, and W. L. Clements. ALASCA: the ESA Laser Guide Star Adaptive Optics Optical Feeder Link demonstrator facility. In K. Minoglou, N. Karafolas, and B. Cugny, editors, *International Conference on Space Optics — ICSO 2022*, volume 12777, page 186. SPIE, 7 2023. ISBN 9781510668034. doi: 10.1117/12.2690989. URL https://www.spiedigitallibrary.org/conference-proceedings-of-spie/12777/2690989/ALASCA--the-ESA-Laser-Guide-Star-Adaptive-Optics-Optical/10.1117/12.2690989.full.

S. Bloom, E. Korevaar, J. Schuster, and H. Willebrand. Understanding the performance of free-space optics. *Journal of Optical Networking*, 2(6):178, 6 2003. ISSN 1536-5379. doi: 10.1364/JON.2.000178. URL https://opg.optica.org/abstract.cfm?URI=jon-2-6-178.

M. J. Booth. Adaptive optics in microscopy. *Philos. Trans. A Math. Phys. Eng. Sci.*, 365(1861):2829–2843, 12 2007.

M. Born and E. Wolf. *Principles of Optics: 60th Anniversary Edition*. Cambridge University Press, 7 edition, 2019.

D. M. Britz, J. P. Dodley, and D. J. Barnickel. Broadband local service offerings using free-space optical links: a network business perspective. *Optical Wireless Communications III*, 4214(February 2001):63–71, 2001. doi: 10.1117/12.417515.

T. Butterley, R. W. Wilson, M. Sarazin, C. M. Dubbeldam, J. Osborn, and P. Clark. Characterization of the ground layer of turbulence at Paranal using a robotic SLODAR system. *Monthly Notices of the Royal Astronomical Society*, 492(1):934–949, 2020. ISSN 13652966. doi: 10.1093/mnras/stz3498.

T. H. Carbonneau and D. D. R. Wisely. Opportunities and challenges for optical wireless: the competitive advantage of free space telecommunications links in today's

crowded marketplace. In P. Christopher, L. Langston, and G. S. Mecherle, editors, *Other Conferences*, volume 3232, page 119. SPIE, 1 1998. doi: 10.1117/12.301022. URL http://proceedings.spiedigitallibrary.org/proceeding.aspx?doi=10.1117/12.301022https://api.semanticscholar.org/CorpusID:108636661.

S. Cheinet and A. P. Siebesma. The impact of boundary layer turbulence on optical propagation. In K. Stein, A. Kohnle, and J. D. Gonglewski, editors, *Optics in Atmospheric Propagation and Adaptive Systems X*, volume 6747, page 67470A, 10 2007. ISBN 9780819469052. doi: 10.1117/12.741433. URL http://proceedings.spiedigitallibrary.org/proceeding.aspx?doi=10.1117/12.741433.

M. Chen, C. Liu, D. Rui, and H. Xian. Performance verification of adaptive optics for satellite-to-ground coherent optical communications at large zenith angle. *Optics Express*, 26(4):4230, 2 2018a. ISSN 1094-4087. doi: 10.1364/oe.26.004230. URL https://doi.org/10.1364/OE.26.004230.

W. Chen, J. Sun, X. Hou, R. Zhu, P. Hou, Y. Yang, M. Gao, L. Lei, K. Xie, M. Huang, R. Li, H. Zang, Y. Wan, E. Dai, Y. Xi, W. Lu, S. Wei, L. Liu, and J. Li. 5.12Gbps optical communication link between LEO satellite and ground station. In *2017 IEEE International Conference on Space Optical Systems and Applications, ICSOS 2017*, pages 260–263, 2018b. ISBN 9781509065110. doi: 10.1109/ICSOS.2017.8357402.

H. J. Chivers and R. D. Davies. A comparison of radio star scintillations at 1390 and 79 Mc/s at low angles of elevation. *Journal of Atmospheric and Terrestrial Physics*, 24(7):573–584, 1962. ISSN 00219169. doi: 10.1016/0021-9169(62)90080-6.

R. Cochetti. *Mobile Satellite Communications Handbook*. John Wiley \& Sons, Nashville, TN, 2 edition, 9 2014.

C. E. Coulman, J. Vernin, and A. Fuchs. Optical seeing—mechanism of formation of thin turbulent laminae in the atmosphere. *Applied Optics*, 34(24):5461, 1995. ISSN 0003-6935. doi: 10.1364/ao.34.005461.

H. Y. D. L. Fried. Telescope-Performance Reciprocity for Propagation in a Turbulent Medium. 1(4):33–42, 1971.

J. M. Dilhac. The Telegraph of Claude Chappe - An Optical Telecommunication Network for the XVIIIth Century. *Institut National des Sciences Appliquées de Toulouse*, pages 1–8, 2001.

O. J. D. Farley, M. J. Townson, and J. Osborn. FAST: Fourier domain adaptive optics simulation tool for bidirectional ground-space optical links through atmospheric turbulence. *Optics Express*, 30(13):23050, 2022. doi: 10.1364/oe.458659.

T. Farrell. The effect of atmospheric optical turbulence on laser communications systems: Part 1, theory. (May 2019):11, 2019. ISSN 1996756X. doi: 10.1117/12.2520055.

R. Fields, D. Kozlowski, H. Yura, R. Wong, J. Wicker, C. Lunde, M. Gregory, B. Wandernoth, and F. Heine. 5.625 Gbps bidirectional laser communications measurements between the NFIRE satellite and an Optical Ground Station. In *2011 International Conference on Space Optical Systems and Applications (ICSOS)*, pages 44–53. IEEE, 5 2011. ISBN 978-1-4244-9686-0. doi: 10.1109/ICSOS.2011.5783708. URL http://ieeexplore.ieee.org/document/5783708/.

E. Fischer, M. Feriencik, K. Kudielka, T. Dreischer, P. Adolph, T. Berkefeld, D. Soltau, J. Kunde, R. Czichy, J. Perdigues-Armengol, and Z. Sodnik. (Invited) Upgrade of ESA optical ground station with adaptive optics for high data rate satellite-to-ground links. *2017 IEEE International Conference on Space Optical Systems and Applications, ICSOS 2017*, 2017:63–70, 2018. doi: 10.1109/ICSOS.2017.8357213.

D. L. Fried. Aperture Averaging of Scintillation. *Journal of the Optical Society of America*, 57(2):169, 1967. ISSN 0030-3941. doi: 10.1364/josa.57.000169.

C. Fuchs and C. Schmidt. Update on DLR's OSIRIS program. In N. Karafolas, Z. Sodnik, and B. Cugny, editors, *International Conference on Space Optics — ICSO*

2018, page 17. SPIE, 7 2019. ISBN 9781510630772. doi: 10.1117/12.2535937. URL https://www.spiedigitallibrary.org/conference-proceedings-of-spie/11180/2535937/Update-on-DLRs-OSIRIS-program/10.1117/12.2535937.full.

C. Fuchs, C. Schmidt, J. Keim, F. Moll, B. Rödiger, M. Lengowski, S. Gaißer, and D. Giggenbach. Update on DLR's OSIRIS program and first results of OSIRISv1 on Flying Laptop. In H. Hemmati and D. M. Boroson, editors, *Free-Space Laser Communications XXXI*, volume 10910, page 109100S. SPIE, 2019. doi: 10.1117/12.2514349. URL https://doi.org/10.1117/12.2514349.

T. Fusco, J.-M. Conan, V. Michau, L. M. Mugnier, and G. Rousset. Efficient phase estimation for large-field-of-view adaptive optics. *Optics Letters*, 24:1472, 1999. ISSN 0146-9592. doi: 10.1364/ol.24.001472.

D. Giggenbach, E. Lutz, J. Poliak, R. Mata-Calvo, and C. Fuchs. A high-throughput satellite system for serving whole europe with fast internet service, employing optical feeder links. *Breitbandversorgung in Deutschland - 9. ITG-Fachkonferenz*, pages 49–55, 2015.

R. E. Good, R. R. Beland, E. A. Murphy, J. H. Brown, and E. M. Dewan. Atmospheric Models Of Optical Turbulence. Number 1988, page 165, 8 1988. doi: 10.1117/12.975626. URL http://proceedings.spiedigitallibrary.org/proceeding.aspx?doi=10.1117/12.975626.

J. W. Goodman. Introduction to Fourier Optics. *Physics Today*, 22(4):97–101, 4 1969. ISSN 0031-9228. doi: 10.1063/1.3035549. URL https://pubs.aip.org/physicstoday/article/22/4/97/426760/Introduction-to-Fourier-Opticshttps://api.semanticscholar.org/CorpusID:118908270.

R. Griffiths, J. Osborn, O. Farley, T. Butterley, M. Townson, and R. Wilson. Demonstrating the first 24-hour continuous vertical monitoring of the atmospheric op-

tical turbulence. *Optics Express*, 31(4):6730–6740, 2023. ISSN 10944087. doi: 10.1364/oe.479544.

J. W. Hardy. *Adaptive Optics for Astronomical Telescopes*. Oxford University PressNew York, NY, 7 1998. ISBN 9780195090192. doi: 10.1093/oso/9780195090192.001.0001. URL https://academic.oup.com/book/52804.

W. Hart, G. M. Brown, S. M. Collins, M. De Soria-Santacruz Pich, P. Fieseler, D. Goebel, D. Marsh, D. Y. Oh, S. Snyder, N. Warner, G. Whiffen, L. T. Elkins-Tanton, J. F. Bell, D. J. Lawrence, P. Lord, and Z. Pirkl. Overview of the spacecraft design for the Psyche mission concept. *IEEE Aerospace Conference Proceedings*, 2018-March:1–20, 2018. ISSN 1095323X. doi: 10.1109/AERO.2018.8396444.

J. R. Holton and G. J. Hakim. *An introduction to dynamic meteorology: Fifth edition*, volume 9780123848. 2012. ISBN 9780123848666. doi: 10.1016/C2009-0-63394-8.

L. Jiang, T. Dai, X. Yu, Z. Dai, C. Wang, and S. Tong. Analysis of scintillation effects along a 7 km urban space laser communication path. *Applied Optics*, 59(27):8418, 9 2020. ISSN 1559-128X. doi: 10.1364/AO.397309. URL https://opg.optica.org/abstract.cfm?URI=ao-59-27-8418.

Y. Jiang, J. Ma, L. Tan, S. Yu, and W. Du. Measurement of optical intensity fluctuation over an 11.8 km turbulent path. *Optics Express*, 16(10):6963, 5 2008. ISSN 1094-4087. doi: 10.1364/oe.16.006963. URL https://opg.optica.org/oe/abstract.cfm?URI=oe-16-10-6963.

A. Johns, B. Seaton, J. Gal-Edd, R. Jones, C. Fatig, and F. Wasiak. James Webb Space Telescope: L2 communications for science data processing. In R. J. Brissenden and D. R. Silva, editors, *Observatory Operations: Strategies, Processes, and Systems II*, number July 2008, page 70161D, 7 2008. ISBN 9780819472267. doi: 10.1117/12.777377. URL http://proceedings.spiedigitallibrary.org/proceeding.aspx?doi=10.1117/12.777377.

M. A. Kallistratova and M. S. Pekour. Structure of optical turbulence over large city. In W. A. Flood and W. B. Miller, editors, *Atmospheric Propagation and Remote Sensing III*, volume 2222, page 894, 6 1994. doi: 10.1117/12.177967. URL http://proceedings.spiedigitallibrary.org/proceeding.aspx?doi=10.1117/12.177967.

F. Kasten. A new table and approximate formula for relative optical air mass. *Archiv für Meteorologie, Geophysik und Bioklimatologie*, 14(Series B):206–223, 1965.

F. Kasten and A. T. Young. Revised Optical Air Mass Tables and approximation formula. *Applied Optics*, 28(22):4735–4738, 1989.

H. Kaushal and G. Kaddoum. Optical Communication in Space: Challenges and Mitigation Techniques. *IEEE Communications Surveys & Tutorials*, 19(1):57–96, 2017. ISSN 1553-877X. doi: 10.1109/COMST.2016.2603518. URL http://ieeexplore.ieee.org/document/7553489/.

D. Lechner, A. Zepp, M. Eichhorn, and S. Gładysz. Adaptable Shack-Hartmann wavefront sensor with diffractive lenslet arrays to mitigate the effects of scintillation. *Optics Express*, 28(24):36188, 11 2020. ISSN 1094-4087. doi: 10.1364/OE.410217. URL https://opg.optica.org/abstract.cfm?URI=oe-28-24-36188.

S. Li and J. Wang. Adaptive free-space optical communications through turbulence using self-healing Bessel beams. *Scientific Reports*, 7(August 2016):1–8, 2017. ISSN 20452322. doi: 10.1038/srep43233.

S. K. Liao, H. L. Yong, C. Liu, G. L. Shentu, D. D. Li, J. Lin, H. Dai, S. Q. Zhao, B. Li, J. Y. Guan, W. Chen, Y. H. Gong, Y. Li, Z. H. Lin, G. S. Pan, J. S. Pelc, M. M. Fejer, W. Z. Zhang, W. Y. Liu, J. Yin, J. G. Ren, X. B. Wang, Q. Zhang, C. Z. Peng, and J. W. Pan. Long-distance free-space quantum key distribution in daylight towards inter-satellite communication. *Nature Photonics*, 11(8):509–513, 2017. ISSN 17494893. doi: 10.1038/nphoton.2017.116.

F. K. Lutgens. *The atmosphere : an introduction to meteorology*. 12th editi edition, 2013. ISBN 9781292054216.

A. Malik and P. Singh. Free Space Optics: Current Applications and Future Challenges. *International Journal of Optics*, 2015(c), 2015. ISSN 16879392. doi: 10.1155/2015/945483.

G. Marchi and C. Scheifling. Turbulence compensation for laser communication, imaging on horizontal path and non-natural turbulence using direct and iterative procedures. *Unconventional Imaging and Wavefront Sensing 2012*, 8520:85200C, 2012. ISSN 0277786X. doi: 10.1117/12.929606.

J. Marino. Expected performance of solar adaptive optics in large-aperture solar telescopes. *Optical Engineering*, 51(10):101709, 2012. ISSN 00913286. doi: 10.1117/1.OE.51.10.101709. URL http://opticalengineering.spiedigitallibrary.org/article.aspx?doi=10.1117/1.OE.51.10.101709.

E. Masciadri, F. Lascaux, A. Turchi, and L. Fini. Optical turbulence forecast: Ready for an operational application. *Monthly Notices of the Royal Astronomical Society*, 466(1):520–539, 2017. ISSN 13652966. doi: 10.1093/mnras/stw3111.

E. Masciadri, A. Turchi, and L. Fini. Towards operational optical turbulence forecast systems at different scales. *Adaptive Optics Systems VIII*, (3):61, 8 2023. doi: 10.1117/12.2629287. URL https://www.spiedigitallibrary.org/conference-proceedings-of-spie/12185/2629287/Towards-operational-turbulence-forecast-systems-at-different-time-scales/10.1117/12.2629287.fullhttp://arxiv.org/abs/2308.03373.

J. L. Miller. Photonics Rules of Thumb. *Optical Engineering*, 36(4):1268, 4 1997. ISSN 0091-3286. doi: 10.1117/1.601287. URL http://opticalengineering.spiedigitallibrary.org/article.aspx?doi=10.1117/1.601287.

A. Montmerle-Bonnefois, C. Petit, C. B. Lim, J. F. Sauvage, S. Meimon, P. Perrault, F. Mendez, B. Fleury, J. Montri, J. M. Conan, V. Michau, N. Védrenne, Z. Sodnik, and C. Voland. Adaptive optics precompensation of a GEO feeder link: The FEEDELIO experiment. *Optics InfoBase Conference Papers*, Part F149-(October 2018):1–8, 2019. ISSN 1996756X. doi: 10.1117/12.2536003.

J. Muñoz-Sabater, E. Dutra, A. Agustí-Panareda, C. Albergel, G. Arduini, G. Balsamo, S. Boussetta, M. Choulga, S. Harrigan, H. Hersbach, B. Martens, D. G. Miralles, M. Piles, N. J. Rodríguez-Fernández, E. Zsoter, C. Buontempo, and J. N. Thépaut. ERA5-Land: A state-of-the-art global reanalysis dataset for land applications. *Earth System Science Data*, 13(9):4349–4383, 2021. ISSN 18663516. doi: 10.5194/essd-13-4349-2021.

J. G. Olmedo and V. P. G. Jiménez. Visibility Framework and Performance Analysis for Free Space Optical Communications in Satellite Links. *IEEE Access*, 11(July): 68897–68911, 2023. ISSN 2169-3536. doi: 10.1109/ACCESS.2023.3292795. URL https://ieeexplore.ieee.org/document/10173531/.

J. Osborn and M. Sarazin. Atmospheric turbulence forecasting with a general circulation model for Cerro Paranal. *Monthly Notices of the Royal Astronomical Society*, 480(1):1278–1299, 2018. ISSN 13652966. doi: 10.1093/MNRAS/STY1898.

J. Osborn, M. J. Townson, O. J. D. Farley, A. Reeves, and R. M. Calvo. Adaptive Optics pre-compensated laser uplink to LEO and GEO. *Optics Express*, 29(4):6113, 2021. ISSN 1094-4087. doi: 10.1364/oe.413013.

J. Pan, M. Evans, T. Euler, H. Johnson, and F. DeNap. Free-space optical communications: opportunities and challenges from a carrier's perspective. In H. Wu, C.-L. I, and J. Vaario, editors, *Wireless and Mobile Communications II*, volume 4911, pages 58–72, 8 2002. doi: 10.1117/12.480489. URL http://proceedings.spiedigitallibrary.org/proceeding.aspx?articleid=884201.

G. Parry, J. G. Walker, and R. J. Scaddan. On the statistics of stellar speckle patterns and pupil plane scintillation. *Optica Acta*, 26(5):563–574, 1979. ISSN 00303909. doi: 10.1080/713820037.

S. Perera, R. W. Wilson, T. Butterley, J. Osborn, O. J. Farley, and D. J. Laidlaw. SHIMM: a versatile seeing monitor for astronomy. *Monthly Notices of the Royal Astronomical Society*, 520(4):5475–5486, 2023. ISSN 13652966. doi: 10.1093/mnras/stad339.

N. Perlot, M. Knapek, D. Giggenbach, J. Horwath, M. Brechtelsbauer, Y. Takayama, and T. Jono. Results of the optical downlink experiment KIODO from OICETS satellite to optical ground station Oberpfaffenhofen (OGS-OP). *Free-Space Laser Communication Technologies XIX and Atmospheric Propagation of Electromagnetic Waves*, 6457(February):645704, 2007. ISSN 0277786X. doi: 10.1117/12.708413.

R. L. Phillips, L. C. Andrews, R. L. Phillips, and C. Young Hopen. Scintillation model for a satellite communication link at large zenith angles. *Optical Engineering*, 39(12): 3272, 2000. ISSN 0091-3286. doi: 10.1117/1.1327839.

S. Piazzolla, W. T. Roberts, J. Kovalik, M. Y. Peng, V. Garkanian, C. P. Chen, W. Buehlman, M. Brewer, G. G. Ortiz, K. T. Matthews, and A. Biswas. Ground station for terabyte infrared delivery (TBIRD). In H. Hemmati and B. S. Robinson, editors, *Free-Space Laser Communications XXXV*, volume 1241311, page 38. SPIE, 3 2023. ISBN 9781510659315. doi: 10.1117/12.2655123. URL https://www.spiedigitallibrary.org/conference-proceedings-of-spie/12413/2655123/Ground-station-for-terabyte-infrared-delivery-TBIRD/10.1117/12.2655123.full.

S. B. Pope. *Turbulent Flows*. Cambridge University Press, 8 2000. ISBN 9780521591256. doi: 10.1017/CBO9780511840531. URL https://www.sae.org/content/210044/

https://www.cambridge.org/core/product/identifier/9780511840531/type/book.

C. A. Primmerman, T. R. Price, R. A. Humphreys, B. G. Zollars, H. T. Barclay, and J. Herrmann. Atmospheric-compensation experiments in strong-scintillation conditions. *Applied Optics*, 34(12):2081, 4 1995. ISSN 0003-6935. doi: 10.1364/AO.34.002081. URL https://opg.optica.org/abstract.cfm?URI=ao-34-12-2081.

J. G. Proakis. *Digital communications*. McGraw-Hill, 4th edition, 2001. ISBN 978-0072321111.

Z. Qu and I. B. Djordjevic. 500 Gb/s free-space optical transmission over strong atmospheric turbulence channels. *Optics Letters*, 41(14):3285, 2016. ISSN 0146-9592. doi: 10.1364/ol.41.003285.

R. Ragazzoni. Pupil plane wavefront sensing with an oscillating prism. *Journal of Modern Optics*, 43(2):289–293, 1996. ISSN 13623044. doi: 10.1080/09500349608232742.

W. C. Reynolds, D. E. Parekh, P. J. Juvet, and M. J. Lee. Bifurcating and blooming jets. *Annual Review of Fluid Mechanics*, 35(1984):295–315, 2003. ISSN 00664189. doi: 10.1146/annurev.fluid.35.101101.161128.

J. R. Roadcap and P. Tracy. A preliminary comparison of daylit and night C n 2 profiles measured by thermosonde. *Radio Science*, 44(2):1–8, 4 2009. ISSN 0048-6604. doi: 10.1029/2008RS003921. URL https://agupubs.onlinelibrary.wiley.com/doi/10.1029/2008RS003921.

F. Roddier. The Effects of Atmospheric Turbulence in Optical Astronomy. *Progress in Optics*, 19:281–376, 1981. ISSN 00796638. doi: 10.1016/S0079-6638(08)70204-X. URL https://linkinghub.elsevier.com/retrieve/pii/S007966380870204X.

F. Roddier. *Adaptive optics in astronomy*, volume 56. Taylor and Francis Ltd., 10 1999. doi: 10.1080/00107514.2015.1041765. URL http://www.tandfonline.com/doi/full/10.1080/00107514.2015.1041765.

T. S. Rose, D. W. Rowen, S. D. LaLumondiere, N. I. Werner, R. Linares, A. C. Faler, J. M. Wicker, C. M. Coffman, G. A. Maul, D. H. Chien, A. C. Utter, R. P. Welle, and S. W. Janson. Optical communications downlink from a low-earth orbiting 15U CubeSat. *Optics Express*, 27(17):24382, 8 2019. ISSN 10944087. doi: 10.1364/oe.27.024382.

E. Ryznar and J. A. Bartlo. Dependence of C_n^2 (C_n^2) in the atmospheric boundary layer on conventional meteorological variables. 33, 1986.

G. Sanders, L. Thorens, M. Reisky, O. Rulik, and S. Deylitz. *GPRS Networks*. Wiley, 8 2003. ISBN 9780470853177. doi: 10.1002/0470869550. URL https://onlinelibrary.wiley.com/doi/book/10.1002/0470869550.

C. M. Schieler, K. Riesing, A. Horvath, B. Bilyeu, J. Chang, A. Garg, J. P. Wang, and B. Robinson. 200 Gbps TBIRD CubeSat downlink: pre-flight test results. In H. Hemmati and B. S. Robinson, editors, *Free-Space Laser Communications XXXIV*, number March 2022, page 34. SPIE, 3 2022. ISBN 9781510648579. doi: 10.1117/12.2615321. URL https://www.spiedigitallibrary.org/conference-proceedings-of-spie/11993/2615321/200-Gbps-TBIRD-CubeSat-downlink-pre-flight-test-results/10.1117/12.2615321.full.

C. Schmidt, B. Rodiger, J. Rosano, C. Papadopoulos, M. T. Hahn, F. Moll, and C. Fuchs. DLR's Optical Communication Terminals for CubeSats. *2022 IEEE International Conference on Space Optical Systems and Applications, ICSOS 2022*, pages 175–180, 2022. doi: 10.1109/ICSOS53063.2022.9749735.

J. Schmidt. *Numerical Simulation of Optical Wave Propagation with examples in MATLAB*. SPIE, 2010. ISBN 9780819483263.

M. Schöck, S. Els, R. Riddle, W. Skidmore, T. Travouillon, R. Blum, E. Bustos, G. Chanan, S. G. Djorgovski, P. Gillett, B. Gregory, J. Nelson, A. Otárola, J. Seguel, J. Vasquez, A. Walker, D. Walker, and L. Wang. Thirty Meter Telescope Site Testing I: Overview. *Publications of the Astronomical Society of the Pacific*, 121(878): 384–395, 2009. ISSN 0004-6280. doi: 10.1086/599287.

M. Sechaud, F. Mahe, T. Fusco, V. Michau, and J.-M. Conan. High-resolution imaging through atmospheric turbulence: link between anisoplanatism and intensity fluctuations. In *Optics in Atmospheric Propagation and Adaptive Systems III*, number September, page 100, 1999. doi: 10.1117/12.371314.

A. Y. Shikhovtsev, P. G. Kovadlo, A. A. Lezhenin, O. A. Korobov, A. V. Kiselev, I. V. Russkikh, D. Y. Kolobov, and M. Y. Shikhovtsev. Influence of Atmospheric Flow Structure on Optical Turbulence Characteristics. *Applied Sciences (Switzerland)*, 13 (3), 2023. ISSN 20763417. doi: 10.3390/app13031282.

T. Soler and D. W. Eisemann. Determination of Look Angles to Geostationary Communication Satellites. *Journal of Surveying Engineering*, 120(3):115–127, 1994. ISSN 0733-9453. doi: 10.1061/(asce)0733-9453(1994)120:3(115).

W. H. Southwell. Validity of the Fresnel approximation in the near field. *Journal of the Optical Society of America*, 71(1):7, 1 1981. ISSN 0030-3941. doi: 10.1364/JOSA.71.000007. URL https://opg.optica.org/abstract.cfm?URI=josa-71-1-7.

M. F. Spencer. Wave-optics investigation of turbulence thermal blooming interaction: II. Using time-dependent simulations. *Optical Engineering*, 59(08):1, 2020. doi: 10.1117/1.oe.59.8.081805.

L. B. Stotts and L. C. Andrews. Bit Error Rate Performance of a Laser Ground-to-Satellite Uplink Communications Systems in the Presence of Atmospheric Turbulence

and Loss. In *2022 IEEE International Conference on Space Optical Systems and Applications, ICSOS 2022*, pages 66–73. IEEE, 2022. ISBN 9781665434393. doi: 10.1109/ICSOS53063.2022.9749698.

O. Svelto. *Principles of lasers*. Springer, fourth edi edition, 1998. ISBN 9781475762662.

V. Tatarski. Wave propagation in a turbulent medium. *Nuclear Physics A*, 139(3):699, 1961. ISSN 03759474. doi: 10.1016/0375-9474(69)90300-5.

V. Tatarskii. The effects of the turbulent atmosphere on wave propagation. page 472, 1971. ISSN 1098-6596.

D. H. Titterton. *Military Laser Technology and Systems*. Artech House, 2015. ISBN 978-1-60807-778-6. URL https://app.knovel.com/hotlink/toc/id:kpMLTS000C/military-laser-technology/military-laser-technology.

A. Tokovinin. Where is the surface-layer turbulence? *Ground-based and Airborne Telescopes III*, 7733(August 2010):77331N, 2010. ISSN 0277786X. doi: 10.1117/12.856409.

A. A. Tokovinin. Ground layer sensing and compensation. *Second Backaskog Workshop on Extremely Large Telescopes*, 5382(1):490, 2004. ISSN 0277786X. doi: 10.1117/12.566207.

O. Topcu, H. Henniger, L. Grobe, M. Haardt, A. Mitschele-Thiel, and T. Simon. Lightweight, mobile free-space optical communications in disaster scenarios for transmission of Earth observation data: feasibility study. In A. K. Majumdar and C. C. Davis, editors, *Free-Space and Atmospheric Laser Communications XI*, volume 8162, page 816203, 9 2011. ISBN 9780819487728. doi: 10.1117/12.898800. URL http://proceedings.spiedigitallibrary.org/proceeding.aspx?doi=10.1117/12.898800.

M. J. Townson, O. J. Farley, G. O. de Xivry, J. Osborn, and A. P. Reeves. AOtools - A python package for adaptive optics modelling and analysis. *arXiv*, 27(22):31316–31329, 2019. ISSN 1094-4087. doi: 10.1364/oe.27.031316.

H. Trinquet and J. Vernin. A Model to Forecast Seeing and Estimate Cn2 Profiles from Meteorological Data. *Publications of the Astronomical Society of the Pacific*, 118(843):756–764, 5 2006. ISSN 0004-6280. doi: 10.1086/503165. URL http://aplicacionesbiblioteca.udea.edu.co:2057/stable/10.1086/503165http://iopscience.iop.org/article/10.1086/503165.

R. Tyson. *Principles of Adaptive Optics*. Elsevier, 1991. ISBN 9780127059006. doi: 10.1016/B978-0-12-705900-6.X5001-0. URL https://linkinghub.elsevier.com/retrieve/pii/B9780127059006X50010.

M. Uysal. *Optical Wireless Communications*. Signals and Communication Technology. Springer International Publishing, Cham, 2016. ISBN 978-3-319-30200-3. doi: 10.1007/978-3-319-30201-0. URL http://link.springer.com/10.1007/978-3-319-30201-0.

D. Vasylyev, W. Vogel, and F. Moll. Satellite-mediated quantum atmospheric links. *Physical Review A*, 99(5), 2019. ISSN 24699934. doi: 10.1103/PhysRevA.99.053830.

ViaSat. Status update for ViaSat-2 - our newest satellite, 8 2017. URL https://news.viasat.com/blog/scn/status-update-for-viasat-2-our-newest-satellite.

J. M. Wallace and P. V. Hobbs. *Atmospheric Science*. Elsevier, 2006. ISBN 9780127329512. doi: 10.1016/C2009-0-00034-8. URL https://linkinghub.elsevier.com/retrieve/pii/C20090000348.

S. M. Walsh, S. F. Karpathakis, A. S. McCann, B. P. Dix-Matthews, A. M. Frost, D. R. Gozzard, C. T. Gravestock, and S. W. Schediwy. Demonstration of 100 Gbps coherent free-space optical communications at LEO tracking rates. *Scientific Reports*,

12(1):1–12, 2022. ISSN 20452322. doi: 10.1038/s41598-022-22027-0. URL https://doi.org/10.1038/s41598-022-22027-0.

T.-L. Wang, I. B. Djordjevic, and J. Nagel. Laser beam propagation effects on secure key rates for satellite-to-ground discrete modulation CV-QKD. *Applied Optics*, 58 (29):8061, 10 2019. ISSN 1559-128X. doi: 10.1364/ao.58.008061.

Z. Wang, Q. Wang, W. Huang, and Z. Xu. *Visible Light communications: Modulation and Signal Processing*. 2017. ISBN 9781119331384. URL https://www.amazon.com/Visible-Light-Communications-Modulation-Communication-ebook/dp/B07822B8MY.

M. L. Wesely and E. C. Alcaraz. Diurnal cycles of the refractive index structure function coefficient. *Journal of Geophysical Research*, 78(27):6224–6232, 9 1973. ISSN 01480227. doi: 10.1029/JC078i027p06224. URL http://doi.wiley.com/10.1029/JC078i027p06224.

L. Westerby-Griffin, J. Osborn, O. J. D. Farley, R. Griffiths, and G. D. Love. Atmospheric optical turbulence analysis in London's financial district. In H. Hemmati and B. S. Robinson, editors, *Free-Space Laser Communications XXXV*, volume 12413, page 55. SPIE, 3 2023a. ISBN 9781510659315. doi: 10.1117/12.2648907. URL https://doi.org/10.1117/12.2648907.

L. Westerby-Griffin, J. Osborn, O. J. D. Farley, R. Griffiths, and G. D. Love. Atmospheric optical turbulence measurements at varying elevation angles. In H. Hemmati and B. S. Robinson, editors, *Free-Space Laser Communications XXXV*, volume 12413, page 56. International Society for Optics and Photonics, SPIE, 3 2023b. ISBN 9781510659315. doi: 10.1117/12.2649231. URL https://doi.org/10.1117/12.2649231.

R. W. Wilson. SLODAR: Measuring optical turbulence altitude with a Shack-Hartmann

wavefront sensor. *Monthly Notices of the Royal Astronomical Society*, 337(1):103–108, 2002. ISSN 00358711. doi: 10.1046/j.1365-8711.2002.05847.x.

R. W. Wilson, T. Butterley, and M. Sarazin. The Durham/ESO SLODAR optical turbulence profiler. *Monthly Notices of the Royal Astronomical Society*, 399(4):2129–2138, 2009. ISSN 13652966. doi: 10.1111/j.1365-2966.2009.15409.x.

J. C. Wyngaard. *Turbulence in the Atmosphere*. Cambridge University Press, 1 2010. ISBN 9780521887694. doi: 10.1017/CBO9780511840524. URL https://www.cambridge.org/core/product/identifier/9780511840524/type/book.

H. Yamazoe, H. Henniger, and K. Iwamoto. The communication experiment result of Small Optical Link for ISS (SOLISS) to the first commercial optical ground station in Greece. *2022 IEEE International Conference on Space Optical Systems and Applications, ICSOS 2022*, pages 40–46, 2022. doi: 10.1109/ICSOS53063.2022.9749739.

A. T. Young. Saturation of Scintillation*. *Journal of the Optical Society of America*, 60(11):1495, 11 1970a. ISSN 0030-3941. doi: 10.1364/JOSA.60.001495. URL https://opg.optica.org/abstract.cfm?URI=josa-60-11-1495.

A. T. Young. APERTURE FILTERING AND SATURATION OF SCINTILLATION. *J Opt Soc Amer*, 60(2):248–250, 1970b. ISSN 0030-3941. doi: 10.1364/josa.60.000248.

A. T. Young. Air mass and refraction. *Applied Optics*, 33(6):1108, 1994. ISSN 0003-6935. doi: 10.1364/ao.33.001108.

S. Zafar and H. Khalid. Free Space Optical Networks: Applications, Challenges and Research Directions. *Wireless Personal Communications*, 121 (1):429–457, 11 2021. ISSN 0929-6212. doi: 10.1007/s11277-021-08644-4. URL https://doi.org/10.1007/s11277-021-08644-4https://link.springer.com/10.1007/s11277-021-08644-4.

V. Zapatero, T. van Leent, R. Arnon-Friedman, W.-Z. Liu, Q. Zhang, H. Weinfurter, and M. Curty. Advances in device-independent quantum key distribution. *npj Quantum Information*, 9(1):10, 2 2023. ISSN 2056-6387. doi: 10.1038/s41534-023-00684-x. URL https://www.nature.com/articles/s41534-023-00684-x.

Q. Zhu, H. Tao, Y. Cao, and X. Li. Laser Inter-Satellite Link Visibility and Topology Optimization for Mega Constellation. *Electronics (Switzerland)*, 11(14), 2022. ISSN 20799292. doi: 10.3390/electronics11142232. URL https://www.mdpi.com/2079-9292/11/14/2232.

G. Ziegelberger. ICNIRP Guidelines on Limits of Exposure to Laser Radiation of Wavelengths between 180 nm and 1,000 μm. *Health Physics*, 105(3):271–295, 9 2013. ISSN 0017-9078. doi: 10.1097/HP.0b013e3182983fd4. URL https://journals.lww.com/00004032-201309000-00006.

R. E. Ziemer and W. H. Tranter. Principles of communications: Systems, modulation, and noise. *Wiley*, 14(5):32–32, 9 2001. ISSN 0094-5579. doi: 10.1109/MCOMD.1976.1089252. URL https://ieeexplore.ieee.org/document/1089252/.

Colophon

This thesis is based on a template developed by Matthew Townson and Andrew Reeves. It was typeset with LaTeX 2_ε. It was created using the *memoir* package, maintained by Lars Madsen, with the *madsen* chapter style. The font used is Latin Modern, derived from fonts designed by Donald E. Kunith.